UNIVERSITY OF CALIFORNIA,
IRVINE

Structural Characterization and Manipulation of Chiral Nanosamples Using Structured Light and Optical Force

DISSERTATION

submitted in partial satisfaction of the requirements
for the degree of

DOCTOR OF PHILOSOPHY

in Electrical and Computer Engineering

by

Mohammad Kamandi

Dissertation Committee:
Professor Filippo Capolino, Chair
Professor Ozdal Boyraz
Professor Kumar Wickramasinghe

2019

To my lovely wife
and
To my parents
for their endless love and support

Raise your words, not voice. It is rain that grows flowers, not thunder.

Rumi

TABLE OF CONTENTS

LIST OF FIGURES

ACKNOWLEDGMENTS

I would like to express the deepest appreciation to my committee chair, Professor Filippo Capolino, for his guidance, constructive criticism and encouragement throughout my graduate career here at UCI. His drive, enthusiasm and passion for excellence in engineering research have been a constant source of inspiration to me.

I would like to thank my committee members, Professor Ozdal Boyraz and Professor Kumar Wickramasinghe who provided guidance and support in our collaborations continuously. I am indebted to their very valuable comments on this thesis.

Every result provided in this thesis was accomplished with the valuable help and support of my fellow labmates and collaborators. Dr. Mohammad Albooyeh and I worked together on different parts of this thesis and without his innovativeness and creativity, my job would have been very difficult. I also acknowledge the contribution of my collaborators, Prof. Maria Vincenti and Prof. Domenico De Ceglia who I had the opportunity to work with and learn from. I thank The former and current members of our research group, in particular Dr. Caner Guclu, Dr. Mehdi Veysi, Dr. Mohamed Othman, Hamidreza Kazemi, Mohsen Rajaei, Dmitry Oshmarin, Dr. Jinwei Zeng, Ahmad Tariq Almutawa and Mohamed Yehia Nada. The former and current staff at the Electrical Engineering department always helped us in most urgent conditions. Therefore, I am very grateful to them, especially to Amy Pham, Susan Staebell, Loretta Waltemeyer, Luba Konkova and Elvia Salas.

More importantly, I am deeply grateful to my wife and my labmate, Mahsa Darvishzadeh Varcheie for her love and patience and for being my source of inspiration and constant support every day, in success as well as in failure.

I owe a great deal to my mother, father, sister and my brothers whose their constant love and endless support give me the strength to pursue my goals in life.

I like to thank Prof. G.P. Li and UCI INRF staff, Jake Hess, Richard Chang and Steven Martinez for helping me out to learn microfabrication process.

Last but not the least, I am grateful for the funding sources that allowed me to pursue my graduate school studies: The National Science Foundation and the USA Keck Foundation.

The text of this dissertation is a reprint of the materials as they appear in American Physical Society and American Chemical Society Journals. The co-authors listed in these publications directed and supervised research which forms the basis for the dissertation.

CURRICULUM VITAE

Mohammad Kamandi

2019 Ph.D. in Electrical and Computer Engineering, University of California, Irvine

2014 M.Sc. in Electrical Engineering, University of Tehran

2011 B.Sc. in Electrical Engineering, Ferdowsi University of Mashhad

EXPERIENCE

2019 Sr. Engineer, Finisar, Fremont, CA, USA

2014-2019 Graduate Student Researcher, Electrical Engineering and Computer Science, University of California Irvine, Advisor: Prof. Filippo Capolino

2018 R&D Intern, Alcon, Lake Forest, CA, USA

FIELD OF STUDY

Nano-Optics, Optical force, Chirality, Nano engineered materials, Electromagnetic modeling, Numerical methods

PUBLICATIONS

J1. **M. Kamandi**, M. Albooyeh, M. Veysi, M. Rajaei, J. Zeng, H. K. Wickramasinghe, F. Capolino, "Unscrambling Structured Chirality with Structured Light at the Nanoscale Using Photoinduced Force," ACS Photonics, vol. 5, no. 11, pp. 4360–4370, Nov. 2018.

J2. **M. Kamandi**, M. Albooyeh, C. Guclu, M. Veysi, J. Zeng, K. Wickramasinghe, F. Capolino, "Enantiospecific Detection of Chiral Nanosamples Using Photoinduced Force," Phys. Rev. Applied, vol. 8, no. 6, p. 064010, Dec. 2017.

J3. **M. Kamandi**, C. Guclu, T. S. Luk, G. T. Wang, and F. Capolino, "Giant field enhancement in longitudinal epsilon-near-zero films," Phys. Rev. B, vol. 95, no. 16, p. 161105, Apr. 2017.

J4. **M. Kamandi**, M. Albooyeh, M. Darvishzadeh-Varcheie, F. Capolino, **"**Discriminating chirality from anisotropy using force photoinduced by the azimuthally-radially polarized beam", to be submitted to Optics Letters.

J5. J. Zeng, **M. Kamandi**, M. Darvishzadeh-Varcheie, M. Albooyeh, M. Veysi, C. Guclu, M. Hanifeh, M. Rajaei, E. O Potma, H. K. Wickramasinghe, F. Capolino, "In pursuit of photo-induced magnetic and chiral microscopy," EPJ Appl. Metamat., vol. 5, p. 7, 2018.

J6. M. A. Vincenti, **M. Kamandi**, D. de Ceglia, C. Guclu, M. Scalora, and F. Capolino, "Surface Second-Harmonic Generation in Longitudinal Epsilon-Near-Zero Materials," Submitted, 2017.

J7. M. Darvishzadeh-Varcheie, W. J. Thrift, **M. Kamandi**, R. Ragan, and F. Capolino, "Two-scale structure for giant field enhancement: combination of Rayleigh anomaly and colloidal plasmonic resonance," Arxiv 1804.01084, Apr. 2018.

J8. M. Rajaei, J. Zeng, M. Albooyeh, **M. Kamandi**, M. Hanifeh, F. Capolino, and H. K. Wickramasinghe, "Giant Circular Dichroism at Visible Frequencies Enabled by Plasmonic Ramp-Shaped Nanostructures," ACS Photonics, Feb. 2019.

J9. J. Zeng, M. Darvishzadeh-Varcheie, M. Albooyeh, M. Rajaei, **M. Kamandi**, M. Veysi, E. O Potma, F. Capolino, H. K. Wickramasinghe, "Exclusive Magnetic Excitation Enabled by Structured Light Illumination in a Nanoscale Mie Resonator," ACS Nano, vol. 12, no. 12, pp. 12159–12168, Dec. 2018.

ABSTRACT

Structural Characterization and Manipulation of Chiral Nanosamples Using Structured Light and Optical Force

By

Mohammad Kamandi

Doctor of Philosophy in Electrical and Computer Engineering

University of California, Irvine, 2019

Professor Filippo Capolino, Chair

Detection, characterization and separation of chiral structures as one of the fundamental constituents of biomolecules are crucial in chemical and biological applications. Conventionally, chiroptical techniques such as circular dichroism (CD) are exploited to identify the material chirality. These methods require substantial amount of sample material with a high concentration. since chirality effect (as an indirect electric to magnetic coupling between incident light and sample material) is typically very weak. Therefore, the observation of chirality might be masked under the electric properties in chiroptical techniques if a substantial amount of material is not provided. Consequently, these techniques are not suitable for detection of chirality for nanoscale samples and can't provide information about their primary or secondary structure. On the other hand, separation of enantiomers is of great interest in pharmaceutical applications. Classical separation techniques which are used to separate molecular compounds and complexes in achiral environment, such as liquid-liquid extraction, chromatography and distillation are not universal for separation of all types of chiral molecules/compounds since not all compounds and host media are chemically compatible. This dissertation focuses on introducing new techniques for detection,

characterization and manipulation of chiral nanoparticles and nanostructures using structured light. Specifically, a new technique involving the measurement of photo-induced optical force (near-field characteristics) rather than the measurement of conventional scattered power (far-field characteristics) is introduced which substantially enhances the resolution in the detection of enantiomer type of chiral samples down to sub-100 nm. Furthermore, by utilizing structured illumination (circularly polarized wave for detection of transverse chirality and combination of azimuthally and radially polarized waves in the so-called azimuthally-radially polarized beam for detection of longitudinal chirality) the prediction of spatial features of the structure of a chiral sample is facilitated. It's been demonstrated that circularly polarized illumination can't differentiate between chirality and anisotropy. To overcome this deficiency and differentiate between anisotropy and chirality, an engineered combination of vortex beams (ARPB) is utilized. Lastly, a novel scheme to manipulate and control chiral nanoparticles and to sort enantiomers is proposed.

CHAPTER 1 : INTRODUCTION

Sec. 1.1 Background and motivation

Activity in biological systems, in terms of the specific interaction with a biological molecule, such as a receptor or enzyme depends strongly on a property of asymmetry called chirality. Molecules or compounds with non-superimposable mirror images are said to be chiral, and the mirror images of chiral molecule are called enantiomers.

Chirality is of supreme importance in life sciences. This significance originates from the fact that the fundamental building blocks of life, i.e., proteins and nucleic acids are built of chiral amino acids and chiral sugar, respectively [1]. More importantly, in pharmaceutical applications, the enzymes and receptors of human body can constructively react to drugs with only proper enantiomers as known as the Fischer's "lock and key" principle[2]. Therefore, if a drug is racemic, i.e., contains both mirror image enantiomers, namely R and S enantiomers, then it might result in detrimental effects beside the desired ones. As a result, based on the importance of chirality in chemical and pharmaceutical sciences, detection and characterization of chiral particles (materials) are fundamentally critical issues. In order to resolve these issues, spectroscopy techniques based on optical rotation (OR), circular dichroism (CD), and Raman optical activity (ROA) have been proposed [3]–[6]. In these chiroptical techniques, the scattered (refracted or absorbed) light from the sample is measured to detect the chirality. In particular, by measuring the difference in absorbance of the right and left hand circularly polarized (CP) light in CD, not only the chirality but also the primary and secondary structure of sample (i.e. proteins) can be determined [7]–[9].

However, down to molecular scales, due to the very weak interaction of light with chiral nanoparticles, the spectroscopic techniques for chirality detection encounter major challenges. For instance, the background scattering noise would play a notable prohibiting role in the chirality detection by using these techniques. Although many studies have been performed to resolve the background noise problem [10], [11], still a considerable amount of the material is required for the detection process. These challenges call for suitable techniques for the development of chirality detection at nanoscales. It should be noted that the optical activity of chiral structures, is a key parameter in molecular identification techniques to recognize the type of a molecule or to determine its structure thanks to the discriminatory behavior of chiral molecules in interaction with the incident light possessing distinct sense of polarization [12], [13].

On the other hand, separating enantiomers is a challenging task which would benefit the advancement of pharmaceutical science and technology. As an example, the common painkiller ibuprofen is a racemic mixture. In manufacturing this drug, equal quantities of both enantiomers are produced, however, only one of them is desired for painkilling. This means companies produce and sell twice the necessary amount of ibuprofen, and many other drugs. Therefore, there is a great deal of work looking at ways to efficiently separate molecules based on handedness. Classical separation techniques which are used to separate molecular compounds and complexes in achiral environment , such as liquid-liquid extraction, chromatography and distillation are not universal for separation of all types of chiral molecules/compounds since not all compounds and host media are chemically compatible [14]. These challenges call for suitable techniques for the development of chirality detection, characterization and separation at nanoscales.

Sec. 1.2 Aim

The aim of this thesis is to elaborate on the fundamentals of using optical force and structured illumination to detect, characterize and sort chiral nanosamples. The considered material samples could be made for example by a concentration of chiral molecules or of an engineered chiral material. We introduce a new microscopy technique involving measurement of photo-induced force rather than scattered power which substantially enhances the resolution in the characterization of chiral samples down to subwavelength scale without confusing chirality with anisotropy. Unlike conventional chiroptical techniques which are vulnerable to background noise and require a considerable amount of sample, thanks to the capabilities of photo-induced force microscopy (PiFM) in exploiting near-field information, we offer a fundamentally new measurement paradigm to resolve the existing limitations. Moreover, we demonstrate that PiFM can be used as a tool to unravel the structure of chiral samples by exploiting circularly polarized (CP) beam and Azimuthally Radially polarized beam (ARPB). We show how ARPB can be used to sort and manipulate opposite enantiomers, which benefits research in branches of science like stereochemistry, biomedicine, physical and material science, and pharmaceutics.

Sec. 1.3 Contents of Each Chapter

The dissertation is organized into Chapters that involve enhancing local electric fields for SERS applications and boosting magnetic fields to enhance the magnetic response of samples in microscopy systems as follows:

Chapter 2: Down to molecular scales, due to the very weak interaction of light with chiral nanoparticles, the spectroscopic techniques for chirality detection encounter major challenges. In this chapter, we use the PIFM for enantiomeric detection of nanoscale chiral samples. We propose to probe the difference between the force exerted on the AFM tip in the vicinity of a sample for

CP wave illuminations with opposite handedness, i.e., right and left hand. We provide analytical arguments which prove that for chiral samples, the proposed differential photoinduced force is nonzero, whereas for achiral ones, it vanishes. More importantly, we demonstrate that for a specific enantiomer, the differential force is equal with opposite sign to its mirror image, which paves the way toward revealing the enantiomer type for a chiral sample at the nanoscale.

Chapter 3: I introduce a technique that facilitates the prediction of spatial features of chirality of nanoscale samples by exploiting photo-induced optical force exerted on an achiral tip in the vicinity of the test specimen and utilize structured light as illuminating beam. The tip-sample interactive system is illuminated by structured light to probe both the transverse and longitudinal (with respect to the beam propagation direction) components of the sample's magnetoelectric polarizability as the manifestation of its sense of handedness, i.e., chirality. I specifically prove that although circularly polarized waves are adequate to detect the transverse polarizability components of the sample, they are unable to probe the longitudinal component. To overcome this inadequacy, I propose a judiciously engineered combination of radially and azimuthally polarized beams, as optical vortices possessing pure longitudinal electric and magnetic field components along their vortex axis, respectively, hence probing longitudinal chirality.

Chapter 4: Spectroscopy and microscopy techniques utilize circularly polarized beams to investigate the structural aspects of chiral samples. However, samples with anisotropic properties may respond similar to circularly polarized beams. Thus we might confuse an anisotropic sample with a chiral one. By taking advantage of the combination of vortex beams, azimuthally polarized beam (APB) and radially polarized beam (RPB), we demonstrate how to differentiate chiral sample from anisotropic achiral sample.

Chapter 5: In this chapter, we propose a scheme to manipulate and control chiral nanoparticles and to sort enantiomers. We exploit structured light at nanoscale based on the so called azimuthally radially polarized beam (ARPB) that is the superposition of a radially and an azimuthally polarized beam with proper phase difference illuminating a plasmonic nanoantenna that is used to interact and exert force on a chiral nanoparticle. Moreover, we demonstrate that two counter-propagating ARPBs separate enantiomers. We provide a rigorous analysis and provide numerical examples to demonstrate the physical principle of the proposed method and emphasize the abilities of this technique.

Chapter 6: In our journey to find a material for enhancing light-matter interaction and optical force, we report that a longitudinal epsilon-near-zero (LENZ) film leads to giant field enhancement and strong radiation emission of sources in it and these features are superior to what was found in previous studies related to isotropic ENZ. LENZ films are uniaxially anisotropic films where relative permittivity along the normal direction to the film is much smaller than unity, whereas the permittivity in the transverse plane of the film is not vanishing. We also prove that, in comparison to the (isotropic) ENZ case, the LENZ film's field enhancement not only is remarkably larger, but also occurs for a wider range of angles of incidence. Importantly, the field enhancement near the interface of the LENZ film is almost independent of the thickness unlike what happens in the isotropic ENZ case where extremely small thickness is required. We show that, for a LENZ structure consisting of a multilayer of dysprosium-doped cadmium oxide and silicon accounting for realistic losses, field intensity enhancement of 30 is obtained which is almost ten times larger than that obtained with realistic ENZ materials.

CHAPTER 2 : ENANTIO-SPECIFIC DETECTION OF CHIRAL NANO-SAMPLES USING PHOTO-INDUCED FORCE

Sec. 2.1 Motivation

In this chapter, we introduce a novel high resolution microscopy technique for enantio-specific detection of chiral samples down to sub-100 nm based on force measurement. Recently, optical force, as a powerful tool for a wide variety of applications from trapping [15]–[18] and manipulating of nanoparticles [19]–[21] to optical cooling [22]–[24] and imaging the electromagnetic fields [25], has been brought up for separation or manipulation of enantiomers [26]. Indeed, in contrast to the long-term common belief that particles are always pushed by light, in [27]–[30] lateral and pulling optical forces were discovered for chiral particles. Therefore, by taking the advantage of the discriminatory behavior of enantiomers, due to their optical activity, Tkachenko et al. in[31] have shown how to sort enantiomers in fluidic environments for micro-meter sized particles. In [32], separating of enantiomers has been expanded to nano-meter sized particles by the same concept using a plasmonic tweezer that rely on enhanced near-field gradients. However, optical force has not been exploited for characterization and enantio-detection of chiral particles.

The importance of detecting chirality at nanoscale in one hand and the lack of high resolution reliable measurement techniques on the other hand urges us to explore possible techniques for detection of chirality of nanoscale particles. Very recently, combining the advantages of atomic force microscopy (AFM)[33] and optical illumination in the so-called photo-

induced force microscopy (PiFM)[34]–[36], has provided the possibility of probing linear[37] and non-linear[38] optical characteristics at the nanoscale with higher accuracies compared to scattering measurement techniques. However, to the best of our knowledge, this encouraging technique which is highly appropriate and accurate to extract optical properties of materials (down to nanoscales) has never been opted to detect the materials' chirality.

In this chapter, we introduce the use of PiFM for enantiomeric detection of nanoscale chiral samples. We propose to probe the difference between the force exerted on the AFM tip in the vicinity of a sample for CP wave illuminations with opposite handedness, i.e., right and left hand. Though material chirality is a weak effect in the light-matter interaction compared to the electric property, we take its effect into account by using the dipolar approximation and considering both electric and magnetic dipole moments. This way, we provide analytical arguments which prove that for chiral samples, the proposed differential photo-induced force is nonzero whereas for achiral ones it vanishes. More importantly we demonstrate that for a specific enantiomer, the differential force is equal with opposite sign to its mirror image which paves the way toward revealing the enantiomer type for a chiral sample at nanoscale. Notice that conventional chiroptical methods such as CD for chirality detection are based on measurements related to averaged far-field scattering from the sample and require a substantial amount of a chiral material. Instead, our proposed technique is capable of enantio-specifically detect the chirality of samples down to sub-100 nm size with a chirality parameter of $\kappa = 0.04$. Future developments may even lead to the detection of weaker chirality.

The chapter is structured as follows. In Sec. 2, we outline the physical principle of PiFM operation by providing the model for tip-sample system and general formulation for the exerted force on the tip. In Sec. 3 we prove the concept of using PiFM as a chirality sensor and provide a

simple formulation to predict the differential photo-induced force on the tip and examine its accuracy by several examples. Then, in Sec. 4, we demonstrate the physics behind the tip-sample interactive system. We exhibit the potential dynamic range of our proposed method in detection of chirality at nanoscale in Sec. 5. At the end, we conclude the chapter with some remarks.

Sec. 2.2 Objective and general physical principle

Fig. 2-1(a) shows the photo-induced force measurement set-up using the PiFM that is investigated in this chapter. The system of nanoscale sample and the microscope tip are illuminated by an incident light from the bottom side. Incident light induces polarization currents on both the sample and tip. The sample and tip are located at the near-fields of their re-scattered fields so that they exert a notable amount of force on each other in the normal direction (the *z*-direction in Fig. 2-1) due to the gradients of their near-fields. Our goal is to show that it is possible to discriminate with respect to the handedness of the chiral sample particle based on applying CP light, with separately left and right polarization and measuring the force exerted to the tip for both polarizations and obtain the force difference.

In order to exemplify the fundamental physical principle of operation, we consider the sample and tip radius to be optically small. Therefore, we may model both the sample and tip as two particles illuminated by an external electromagnetic field with wave vector k [Fig. 2-1(b)]. The sample is characterized by a bianisotropic response (chirality is a special case) that provides both electric $\mathbf{p}_s$ and magnetic $\mathbf{m}_s$ dipolar moments (where subscript "s" represents "sample"). Indeed, the consideration of magnetic dipole moment is necessary in the analysis of the electromagnetic response of chiral particles since under electromagnetic illumination, a sample composed of chiral inclusions exhibits optical activity. Under the dipolar approximation, valid for subwavelength particles, such as molecule concentrations or engineered "meta-atoms", the optical

activity is well described by the introduction of the electric dipole-to-magnetic dipole (magnetoelectric) polarizability [39]. Notice, although this magnetoelectric polarizability is weak compared to that associated to the electric dipole polarizability, neglecting it in the analysis of chiral particles would result in an incorrect prediction of the electromagnetic response of the sample. Based on the above discussion, by using the polarizability tensor of such a chiral particle, the electric and magnetic dipole moments read[40]–[42]

$$\begin{bmatrix} \mathbf{p}_{\mathrm{s}} \\ \mathbf{m}_{\mathrm{s}} \end{bmatrix} = \begin{bmatrix} \underline{\boldsymbol{\alpha}}_{\mathrm{s}}^{ee} & \underline{\boldsymbol{\alpha}}_{\mathrm{s}}^{em} \\ \underline{\boldsymbol{\alpha}}_{\mathrm{s}}^{me} & \underline{\boldsymbol{\alpha}}_{\mathrm{s}}^{mm} \end{bmatrix} \begin{bmatrix} \mathbf{E}^{\mathrm{loc}}\left(\mathbf{r}_{\mathrm{s}}\right) \\ \mathbf{H}^{\mathrm{loc}}\left(\mathbf{r}_{\mathrm{s}}\right) \end{bmatrix} \tag{2.1}$$

here $\mathbf{E}^{\mathrm{loc}}$ and $\mathbf{H}^{\mathrm{loc}}$ are, respectively, the phasors of the local electric and magnetic field at the sample location $\mathbf{r}_{\mathrm{s}}$. Moreover, $\underline{\boldsymbol{\alpha}}^{ee}$, $\underline{\boldsymbol{\alpha}}^{mm}$, $\underline{\boldsymbol{\alpha}}^{em}$, and $\underline{\boldsymbol{\alpha}}^{me}$ are, respectively, electric, magnetic, magnetoelectric and electromagnetic polarizability tensors of the sample particle. The last two polarizability tensors are also called bianisotropic parameters which relate the local electric (magnetic) field to the magnetic (electric) dipole moment. In general, there are four classes of bianisotropic particles, i.e., omega, chiral, Tellegen, and "moving", which any dipole particle can be reduced to. The first two classes are reciprocal while the second two are nonreciprocal. Reciprocity implies $\underline{\boldsymbol{\alpha}}^{me} = -\left(\underline{\boldsymbol{\alpha}}^{em}\right)^{\mathrm{T}}$, where superscript "T" denotes the tensor transpose. In addition, for a pure chiral sample particle, the bianisotropic tensors are diagonal, hence one has $\alpha_{jj}^{me} = -\left(\alpha_{jj}^{em}\right)$, where $j=x,y,z$. Under the assumption of negligible sample losses α_{jj}^{me} is purely imaginary [41].

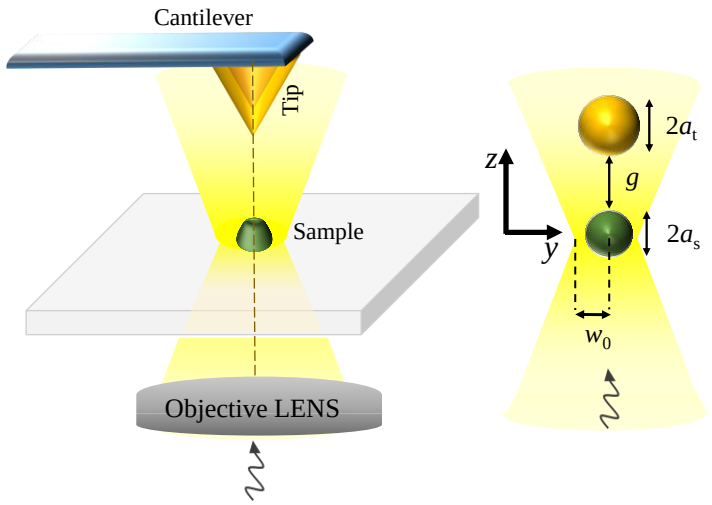

FIG. 2-1 (a) Schematic of photo-induced force microscopy capable of detecting the chirality of a sample based on differential force measurement. (b) Simplified model where the tip and sample are represented by nanospheres with electric (and perhaps magnetic) dipole moment(s).

In the following, we assume that the chiral sample has a spherical shape and has isotropic response (as in the case it contains an amorphous arrangement of many chiral molecules). The sample's isotropic response implies it has equal polarizability components in all spatial directions. Under this assumption, the electric and magnetic polarizability tensors reduce to $\underline{\boldsymbol{\alpha}}^{ee} = \alpha^{ee}\underline{\mathbf{I}}$ and $\underline{\boldsymbol{\alpha}}^{mm} = \alpha^{mm}\underline{\mathbf{I}}$, respectively, where $\underline{\mathbf{I}}$ is the identity tensor. Moreover, for a chiral isotropic particle $\underline{\boldsymbol{\alpha}}^{em} = \alpha^{em}\underline{\mathbf{I}}$ and $\underline{\boldsymbol{\alpha}}^{me} = -\left(\underline{\boldsymbol{\alpha}}^{em}\right)^{\mathrm{T}} = -\alpha^{em}\underline{\mathbf{I}}$ (where superscript "T" denotes the tensor transpose) would be the magnetoelectric and electromagnetic polarizability tensors, respectively. The expressions for polarizabilities of an isotropic spherical chiral particle in terms of its permittivity, permeability, and chirality parameter, obtained based on Mie scattering theory, are given in Appendix A. We assume the tip is achiral and model its response to an electromagnetic wave by electric and magnetic dipole moments

$$\mathbf{p}_{\mathrm{t}} = \underline{\boldsymbol{\alpha}}_{\mathrm{t}}^{ee} \cdot \mathbf{E}^{\mathrm{loc}}\left(\mathbf{r}_{\mathrm{t}}\right), \qquad \mathbf{m}_{\mathrm{t}} = \underline{\boldsymbol{\alpha}}_{\mathrm{t}}^{mm} \cdot \mathbf{H}^{\mathrm{loc}}\left(\mathbf{r}_{\mathrm{t}}\right). \tag{2.2}$$

Notice, the local electromagnetic field is considered at the tip location $\mathbf{r}_{\mathbf{t}}$, where subscript "t" represents "tip". Also, the local field at the tip position is the contribution of the external incident and the scattered fields of the sample, which is modeled as a dipolar system with the electric and magnetic moments as defined in Eq. (2.1). Considering this model, the general expression of the time-averaged optical force exerted on the tip is given by [30]

$$\begin{aligned}\left\langle \mathbf{F} \right\rangle = \frac{1}{2}\mathrm{Re}\Bigg[& \mathbf{p}_{\mathrm{t}} \cdot \left(\nabla \mathbf{E}^{\mathrm{loc}}(\mathbf{r}_{\mathrm{t}})\right)^{*} + \mathbf{m}_{\mathrm{t}} \cdot \left(\nabla \mathbf{H}^{\mathrm{loc}}(\mathbf{r}_{\mathrm{t}})\right)^{*} \\ & - \frac{ck^{4}}{6\pi}\left(\mathbf{p}_{\mathrm{t}} \times \mathbf{m}_{\mathrm{t}}^{*}\right)\Bigg],\end{aligned} \tag{2.3}$$

where the asterisk denotes complex conjugation, c is the speed of light and k is the wavenumber of host medium. Moreover, $\nabla\mathbf{E}$ and $\nabla\mathbf{H}$ are two tensors of the second rank (the gradient of a vector is defined in the Appendix B). In Eq. (2.3), the first and second terms represent the force acting on the corresponding electric and magnetic dipoles of the tip, respectively, while the third term represents the force due to the interaction between both induced electric and magnetics dipoles of the tip. We calculate the exerted force on the tip by using the above formalism. In this thesis every field is monochromatic and the time convention $e^{-i\omega t}$ is implicitly assumed and suppressed.

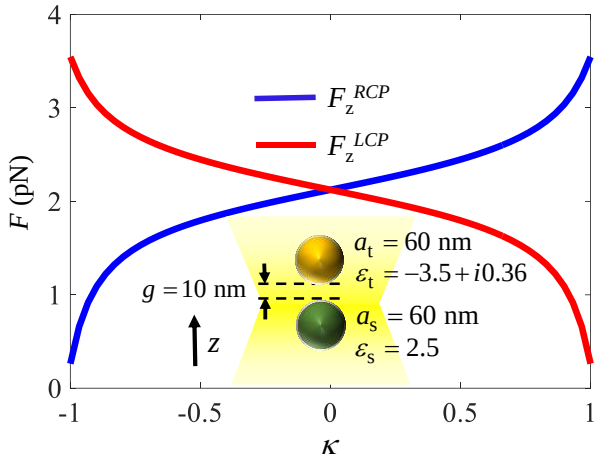

FIG. 2-2. The effect of sample chirality on the induced force on the tip for two incident scenarios of RCP and LCP light.

Sec. 2.3 PIFM as Chiralilty sensor at nanoscale

In this section, we illustrate the potential of PiFM in distinguishing enantiomer type of nanoscale samples. Based on the force formulation discussed in section II, i.e., by using dipole approximation limit and Mie scattering theory to calculate the polarizability of spherical chiral sample nanospheres, we examine the force induced on the achiral tip for different scenarios. As was discussed, we illuminate the tip-sample system with an incident light from the bottom side (see Fig. 2-1). We selectively apply CP light with both handedness, i.e. right and left hand CP (RCP and LCP) light. The induced polarizations on an achiral sample would be the same for the RCP and LCP beams. This results in identical re-scattered fields for an achiral sample when excited with the proposed RCP or LCP. Therefore, the exerted force on the tip alone (along the propagation *z*-direction) is the same for opposite sense of handedness of the incident light. In contrast, by virtue of its optical activity, the induced polarizations $\mathbf{p}_s$ and $\mathbf{m}_s$ on a chiral sample are not equal for opposite sense of incident light handedness, and hence, the re-scattered near-fields are different. Therefore, for a chiral sample, the exerted force on the tip would be different for opposite sense of

handedness of the incident light. To verify this, we consider an exemplary case when the sample and plasmonics tip are both considered to have equal radii $a_s = a_t = 60$ nm which are at a distance to form a particle-to-particle gap of $g = 10$ nm (see Fig. 2-3). Moreover, without loss of generality, the relative permittivity of the sample is assumed to be $\varepsilon_s = 2.5$ whereas the plasmonics tip is assumed to have a relative permittivity $\varepsilon_t = -3.5 + i0.35$ (this choice will be discussed later). The incident light is assumed to be CP Gaussian beam propagating along the *z*-direction with wavelength $\lambda = 504$ nm with 1mW power. The waist of the Gaussian beam (see Fig. 2-1) is set to $w_0 = 0.7\lambda$ and is positioned at the z=0 plane, where the sample is located, because of the higher strength of the field at the beam waist along the beam axis. The sample is made of a sphere composed of chiral material described by the chirality parameter κ that here varies from -1 to 1 (see Appendix A). By using the introduced analytical formalism, the force expression Eq. (2.3), we have calculated the *z*-component of the induced force on the tip F_z^{RCP} and F_z^{LCP} versus chirality parameter κ, for the two excitation scenarios with RCP and LCP beams. The results in Fig. 2-2 show that there is no force difference between two cases of RCP and LCP incidences for $\kappa = 0$. However, as we increase the amplitude of the chirality parameter κ of the sample, the differences between induced forces on the tip becomes more obvious, in the order of piconewtons. Moreover, if we define the differential photo-induced force as

$$\Delta F = F_z^{RCP} - F_z^{LCP}. \tag{2.4}$$

We note that for a pair of enantiomer ΔF is equal in amplitude but opposite in sign (we recall that the chirality parameters of an enantiomer and its mirror image have equal amplitude

with opposite sign). This example clearly demonstrates that by measuring differential photo-induced force, we can differentiate between chiral enantiomers.

To unravel the physical principle behind this interesting discriminatory behavior of chiral particles, we note that the local field acting on the sample to be used in Eq. (2.1), provided by both the incident field and the near-field generated by the tip, is found by

$$\begin{aligned}\mathbf{E}^{\mathrm{loc}}\left(\mathbf{r}_{\mathrm{s}}\right)&=\mathbf{E}^{\mathrm{inc}}\left(\mathbf{r}_{\mathrm{s}}\right)+\underline{\mathbf{G}}^{\mathrm{EP}}\left(\mathbf{r}_{\mathrm{s}},\mathbf{r}_{\mathrm{t}}\right)\cdot\mathbf{p}_{\mathrm{t}},\\ \mathbf{H}^{\mathrm{loc}}\left(\mathbf{r}_{\mathrm{s}}\right)&=\mathbf{H}^{\mathrm{inc}}\left(\mathbf{r}_{\mathrm{s}}\right)+\underline{\mathbf{G}}^{\mathrm{HP}}\left(\mathbf{r}_{\mathrm{s}},\mathbf{r}_{\mathrm{t}}\right)\cdot\mathbf{p}_{\mathrm{t}}.\end{aligned} \tag{2.5}$$

Here $\underline{\mathbf{G}}^{\mathrm{EP}}$ and $\underline{\mathbf{G}}^{\mathrm{HP}}$ are the dyadic Green's functions that provide the electric and magnetic fields, respectively, generated by an electric dipole [42]. As was discussed earlier, we investigate the case of an isotropic achiral tip, whose dipole moments $\mathbf{p}_{\mathrm{t}}$ and $\mathbf{m}_{\mathrm{t}}$ are given by Eq. (2.2). Moreover, in Eq. (2.5) we have assumed that the magnetic dipole moment $\mathbf{m}_{\mathrm{t}}$ of the tip is negligible which we clarify later to be an acceptable approximation for a tip made of plasmonic material (note that the results of Fig. 2-2 are obtained considering all dipole terms in Eq. (2.3) including a very small $\mathbf{m}_{\mathrm{t}}$, however, in deriving an approximate formula for the force we have neglected the magnetic dipole moment $\mathbf{m}_{\mathrm{t}}$ of the tip). The local electric field at the tip is provided by both the incident field and the near-field scattered by the sample that is assumed to possess both electric $\mathbf{p}_{\mathrm{s}}$ and magnetic $\mathbf{m}_{\mathrm{s}}$ dipole moments:

$$\mathbf{E}^{\mathrm{loc}}\left(\mathbf{r}_{\mathrm{t}}\right)=\mathbf{E}^{\mathrm{inc}}\left(\mathrm{r}_{\mathrm{t}}\right)+\underline{\mathbf{G}}^{\mathrm{EP}}\left(\mathrm{r}_{\mathrm{t}},\mathrm{r}_{\mathrm{s}}\right)\cdot\mathbf{p}_{\mathrm{s}}+\underline{\mathbf{G}}^{\mathrm{EM}}\left(\mathrm{r}_{\mathrm{t}},\mathrm{r}_{\mathrm{s}}\right)\cdot\mathbf{m}_{\mathrm{s}}. \tag{2.6}$$

Here $\underline{\mathbf{G}}^{\mathrm{EM}}$ is the dyadic Green's function that provides the electric field generated by a magnetic dipole. The expression for the time-averaged optical force exerted on the achiral tip (neglecting the effect of magnetic dipole i.e., $\mathbf{m}_{\mathrm{t}} = 0$) reads

$$\langle \mathbf{F} \rangle = \frac{1}{2} \mathrm{Re}\left[\mathbf{p}_{\mathrm{t}} \cdot \left(\nabla \mathbf{E}^{\mathrm{loc}}(\mathbf{r}_{\mathrm{t}}) \right)^{*} \right]. \tag{2.7}$$

Calculations are done by using all the dynamic terms in the Green's function. Next, neglecting the field's phase difference between the tip and sample, due to their subwavelength distance, it can be shown (see Appendix B for more details) that the difference between the forces exerted on the tip for two CP plane waves with opposite handedness reads

$$\Delta F \approx -\frac{3|\mathbf{E}_0|^2}{4\pi\sqrt{\varepsilon_0 \mu_0}\, d^4} \mathrm{Im}\left\{ \alpha_{\mathrm{t}}^{ee} \alpha_{\mathrm{s}}^{em} \right\}. \tag{2.8}$$

In deriving this approximate but physically insightful formula we have assumed the axial Gaussian beam field to be approximated with a CP plane wave with electric field magnitude $|\mathbf{E}_0|$. Furthermore, ε_0 and μ_0 are, respectively, the free space permittivity and permeability, and d is the center-to-center distance between tip and sample. Eq. (2.8) is a striking result since it clearly demonstrates that in the absence of the magnetoelectric polarizability (i.e., $\alpha_{\mathrm{s}}^{em} = 0$) ΔF would be zero, while for a chiral sample it is not the case. Therefore, we can distinguish between chiral and achiral samples by observing ΔF. More importantly, as is known, the quasi-static approximation for magnetoelectric polarizability α^{em} of a chiral sphere with material parameters ε_{s}, μ_{s} and κ is [43]

$$\alpha_s^{em} = 12i\pi a^3 \sqrt{\varepsilon_0 \mu_0}\, \frac{\kappa}{(\varepsilon_s + 2)(\mu_s + 2) - \kappa^2}, \tag{2.9}$$

where a is the radius of the sphere, and it is considered that $\mu_s = 1$. From Eq. (2.9) the sign of magnetoelectric polarizability α_s^{em} is dictated by the sign of chirality parameter of the sample κ. Therefore, Eq. (2.8) expresses that ΔF is equal in amplitude but opposite in sign for a pair of enantiomer, which affirms that our proposed method is capable of distinguishing enantiomer type. It is also worth mentioning that based on Eq. (2.8) and (2.9), ΔF is linearly proportional to chirality parameter κ of the sample (since κ^2 in the denominator of Eq. (2.9) is much smaller than the first term for natural materials) within the quasi-static approximation. Additionally, Eq. (2.8) states that ΔF is linearly dependent to the electric polarizability of the tip, emphasizing the importance of the tip material and its geometry. In our example we have assumed to have a plasmonic tip to boost its electric dipolar response and hence increasing the electric polarizability contribution. Furthermore, $\Delta F \propto 1/d^4$ (where d is the center-to-center distance between the tip and the sample) which illustrates the sensitivity of the probing force to the distance between the tip and the sample.

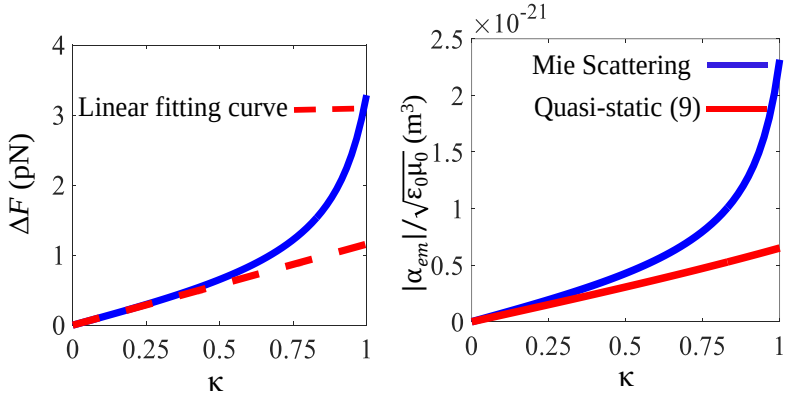

FIG.2-3. a) ΔF versus chirality parameter κ of the sample. Tip and sample spheres' radii are $a_s = a_t = 60$ nm and $\varepsilon_t = -3.5 + i0.35$ and $\varepsilon_s = 2.5$, and gap is $g = 10$ nm. For completeness we show a linear fitting curve

for ΔF b) Normalized magnetoelectric polarizability of the sample using Mie formula given in Appendix A and the quasi-static approximation Eq. (2.9).

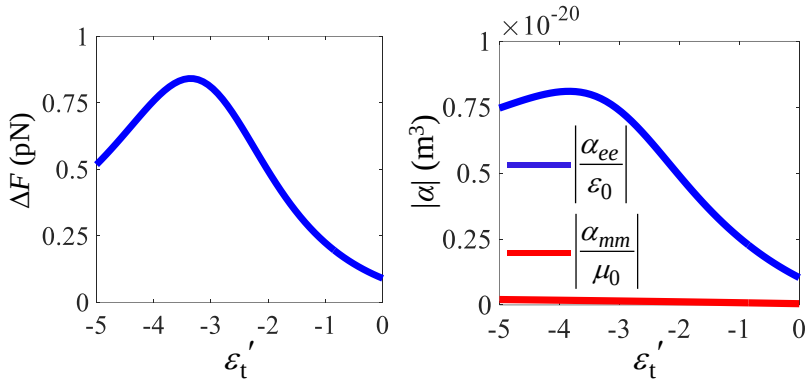

FIG. 2-4. Differential force ΔF and normalized electric and magnetic polarizability of the tip as a function of the real part of the tip relative permittivity. A plasmonics tip provides a stronger electric polarizability and hence a stronger force.

We have shown the main physical principle and we now dig into Eq. (2.8) to demonstrate how our analytical formalism boast itself in predicting the general trends of differential photo-induced force. To that end, we first emphasize on the dependence of the differential force on the chirality parameter κ. We assume equal radii for the tip and sample i.e., $a_s = a_t = 60$ nm with the gap $g = 10$ nm between the tip and sample. Furthermore, we consider the relative permittivity of the tip and sample to be $\varepsilon_t = -3.5 + i0.35$ and $\varepsilon_s = 2.5$, respectively, as was done for the result in Fig. 2-2. We then sweep over the chirality parameter of the tip from 0 to 1. By applying Eq. (2.3), we plot the differential induced forces ΔF on the tip for the two different incidence scenarios of RCP and LCP beams (solid blue line in Fig. 2-3(a)). As it is clear, ΔF shows linear dependence on κ when its chirality parameter is smaller than 0.5. For $\kappa > 0.5$ the differential force ΔF diverges from its linear fitting curve, the red dashed line in Fig. 2-3(a) which presents the asymptotic linear behavior of the differential force for small chirality parameter κ. To provide an

insight for the reason of this behavior, we have plotted the normalized (to 1/c) magnetoelectric polarizability of the sample as a function of chirality parameter [see Fig. 2-3(b)], calculated with two methods; i.e., the exact calculation using Mie coefficients (see Appendix A) and the approximate quasi-static formulation in Eq. (2.9). As it can be seen, for $\kappa < 0.5$ the results of both exact and approximate methods absolutely match whereas for higher values of κ the quasi-static approximation diverges from the accurate Mie coefficient result. Thus, α^{em} and hence ΔF are assumed to be linearly dependent on κ for $\kappa < 0.5$. Indeed the direct comparison between ΔF plotted in Fig 2-3(a) and the magnetoelectric polarizability α^{em} of the sample calculated through the exact Mie coefficient (in Appendix A) shown in Fig 2-3 (b) is decoding their linear dependence. This result is exactly what we previously stated based on Eq. (2.8).

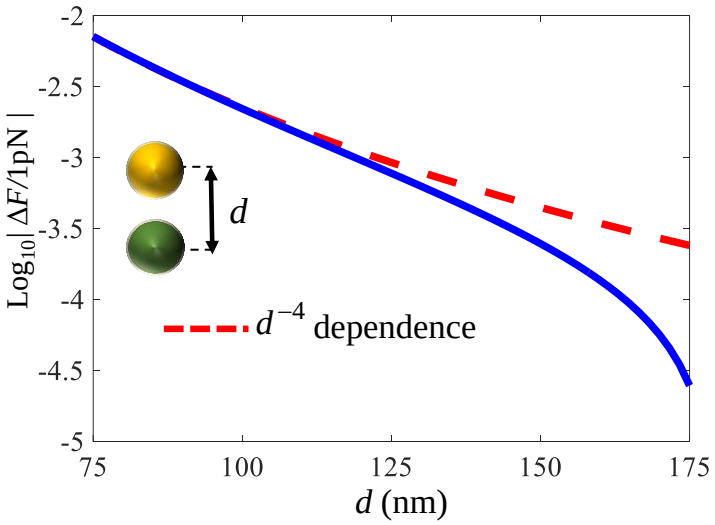

FIG. 2-5. ΔF in logarithmic scale versus the distance between the tip and sample (solid blue line) along with a d^{-4} dependent function (red dashed line).

As one can infer from the approximate formula (8), the next crucial parameter in determining differential induced force is the tip electric dipolar polarizability α_t^{ee}. In Fig. 2-4 we provide ΔF and normalized electric and magnetic polarizabilities as functions of real part of the

tip relative permittivity given by $\varepsilon_t = \varepsilon_t' + i0.35$ assuming $a_s = 60$ nm. As shown in Fig. 2-4 (a), ΔF peaks around $\varepsilon_t' = -3.5$ which corresponds to the electric resonance of the tip which is demonstrated in Fig. 2-4(b). From a comparison between Figs. 2-4(a) and 2-4(b) we conclude that ΔF and α_t^{ee} reveal similar behaviors as we sweep the real part of permittivity which once more proves the potential of using Eq. (2.8) to state that ΔF is linearly dependent on the tip electric polarizability α_t^{ee}. (Force calculation is done via Eq. (2.3) using the dynamic Green's function.) Notice that the magnetic polarizability is much smaller than its electric counterpart, emphasizing the negligible contribution of the second and third terms of Eq. (2.3). As a result of the above discussion, we conclude that the choice of material parameter for the tip is of quite high importance because the dynamic range of experimental measurement setup is limited by noise and the force value may be small depending on particle size, laser power, and materials. As we will discuss in the next section and as demonstrated in Eq. (2.8), a tip with strong electric polarizability enabled by plasmonic material enhances the measured photo-induced force response of a chiral sample and hence the differential force. Our goal is to enantio-specify samples with nanoscale size (microscopic chirality identification), despite the weak chiral response of their matter constituent, by using plasmonic material for the tip. It should be noted that the tip shape could also be engineered to provide even higher electric polarizability compared to a simple plasmonic sphere [11], [32], [44]–[49] (e.g. a triangular prism or truncated tetrahedron). However, considering the fact that our aim is to introduce the technique and to prove its capability, we assumed a plasmonic spherical tip (simplest shape) in our analysis. Nevertheless, in future study involving also experimental verification, the tip shape could be engineered to further enhance the ability in the detection of observable response of the chiral sample. Note that however shorter distances *d* may

provide a much stronger force but we cannot show it here since the dipolar representation of tip and sample loses validity for smaller distances.

Indeed, the last central parameter in the enantio-specific detection of chiral nano-samples is the tip-sample distance as illustrated in the differential force approximate expression Eq. (2.8). In Fig. 2-5, we have depicted ΔF in logarithmic scale, evaluated by Eq. (2.3), as a function of the tip-sample distance from 75 nm to 175 nm along with a d^{-4} dependent function for a tip-sample system with parameters as follows: $a_s = a_t = 25\ \text{nm}$, $\varepsilon_t = -3.5 + 0.35i$, $\varepsilon_s = 2.5$ and $\kappa = 0.6$. As shown, there is a good agreement between the force and d^{-4} function which was again predicted by Eq. (2.8).

So far, we have analytically proved that by using PiFM we not only detect chiral samples by using achiral probes, but also specifically determine the enantiomer type of a chiral sample. We have supported our analytical findings by numerical calculations. In the next section, by using analytical formulations we present the effective polarizability model for an achiral tip when it is closely positioned near a chiral sample, hence, give physical insight to explain the phenomena happened in the aforementioned discussion.

Sec. 2.4 Optical activity transfer from chiral sample to achiral tip

We provide here a simple formulation to predict the differential photo-induced force on the tip in the vicinity of a chiral sample. In this section we aim at delivering an equivalent representation of electric dipole moment which presents deep physical insight into a unique phenomenon: i.e., the transfer of optical activity from a chiral particle to an achiral one in its vicinity. In this equivalent representation, we rewrite the electric dipole moment of the tip as

$$\mathbf{p}_{\mathrm{t}} = \hat{\alpha}_{\mathrm{t}}^{ee}\mathbf{E}^{\mathrm{inc}} + \hat{\alpha}_{\mathrm{t}}^{em}\mathbf{H}^{\mathrm{inc}}. \tag{2.10}$$

in which $\hat{\alpha}_{\mathrm{t}}^{ee}$ and $\hat{\alpha}_{\mathrm{t}}^{em}$ are the effective electric and magnetoelectric polarizabilities of the tip when it is in the close vicinity of the chiral particle. As it is clear, in this representation, instead of local electric and magnetic fields, we use incident fields. In other words, we include the presence of the chiral particle near-field by modifying the polarizability of the tip. As shown in the Appendix C, effective electric and magnetoelectric polarizabilites are given by

$$\hat{\alpha}_{\mathrm{t}}^{ee} = \alpha_{\mathrm{t}}^{ee}\frac{1-\alpha_{\mathrm{s}}^{ee}G}{1-\alpha_{\mathrm{t}}^{ee}\alpha_{\mathrm{s}}^{ee}G^2}, \tag{2.11}$$

$$\hat{\alpha}_{\mathrm{t}}^{em} = -\alpha_{\mathrm{t}}^{ee}\frac{\alpha_{\mathrm{s}}^{em}G}{1-\alpha_{\mathrm{t}}^{ee}\alpha_{\mathrm{s}}^{ee}G^2}, \tag{2.12}$$

in which G is defined in (B4). It is very important to notice that although the tip is not chiral and is modeled by a simple electric dipole, the impact of the chiral sample makes the tip to effectively act as a chiral particle as in Eq. (2.10). That is to say, a chiral sample can induce chirality to an achiral particle if placed in vicinity of it which can be utilized in two ways: 1) creating artificial optically active particles using achiral materials, and 2) using plasmonic particles as a "reporter" (or equivalently an antenna) for chirality detection. Here we engineer a gold nanoparticle to be optically active by placing it in the vicinity of a chiral particle. Thanks to the strong electric resonance of plasmonic particles, the optical activity of the tip-sample interactive system will be enhanced compared to a single chiral particle. The advantage of creating a chirality reporter using a plasmonic particle can be understood by observing that the chiral response of most biomolecules peaks in UV regime, however, in the vicinity of a plasmonic particle, this signature can be brought to plasmonic band, making the measurement easier in the visible region. Although this phenomena has been already reported in [49]–[53], here we have provided a rigorous analytic representation

of it which allows to design proper antennas in order to maximize magnetoelectric coupling and hence improving chirality detection. Using this equivalent approach, we can show that the differential induced force on the tip at the close vicinity of the sample reads (see Appendix C)

$$\Delta F = F_z^{RCP} - F_z^{LCP} = \\ -\frac{|\mathbf{E}_0|^2}{\left|\alpha_t^{ee}\right|^2}\mathrm{Im}\left\{\alpha_t^{ee}\left(\hat{\alpha}_t^{ee}\frac{\partial\hat{\alpha}_t^{em*}}{\partial z}-\hat{\alpha}_t^{em}\frac{\partial\hat{\alpha}_t^{ee*}}{\partial z}\right)\right\}\Bigg|_{z=z_t}, \tag{2.13}$$

in which $\partial/\partial z$ represents partial derivative with respect to the position on the z-axis. This formula further emphasizes the dependence of ΔF on the effective parameters of the tip, i.e., effective electric and magnetoelectric polarizabilities.

We conclude this section by stating that our analytical formalism allows us to suggest another approach to maximize the signature of optical activity of nanoparticles by using properly engineered nano-antennas which enhance both electric and magnetic fields rather than only electric field [54] which is what we have shown here. Notice, the magnetic dipole of the antenna must be properly oriented in order to effectively couple to the chirality of sample particle. That is, if the antenna can be represented by dipole moments, its electric and magnetic moments must be collinear which implies a chiral response. To obtain such strong coupling between the antenna and the sample particle, and hence, a stronger optical response of the tip, we suggest to take the advantage of a proper combination of structured light excitation and antenna near-field response which can be a subject for further studies. For instance, one may use a chiral antenna [55], [56] with CP excitation. Alternatively, one may use an achiral antenna structure with both electric and magnetic responses and use a combination of the structured light as the excitation scheme to control the coupling between chiral samples and the tip.

In the next section, we provide a measure to clarify the dynamic range of our approach in probing chirality of optically small nano-samples down to sub-100 nm sizes.

Sec. 2.5 Potential of the approach in detecting nanoscale chiral inclusions

So far, we have demonstrated the possibility of detecting chirality and the enantiomer-type of nanoscale samples using photo-induced force. However, we have not yet discussed the resolution of our proposed method i.e., the minimum size of the specimen which results in a detectable ΔF and how misalignment of the tip affects the chirality detection. To investigate this first issue, in Fig. 2-6 we make a color map showing ΔF in the logarithmic scale versus chirality parameter κ (again in logarithmic scale) of the sample and radius of the sample a_{s}. We have assumed that the radius of the tip is $a_{\mathrm{t}} = 60$ nm and the gap is $g = 10$ nm and the sample is positioned at z=0 plane on the axis of the excitation beams at the minimum beam waist. As before, we assume relative permittivities of the tip and sample to be the same as Fig. 2-2. The chosen chirality parameter range binds the chirality parameter of common chiral specimens including DNA-assembled nanostructures and composite nanomaterials [32]. We have marked the 0.1pN force boundary with a black solid line. For the region above this black line, ΔF is greater than 0.1pN. This number is chosen based on[57] to be the instrument general sensitivity. It can be seen, the smallest detectable chirality parameter value κ for the maximum studied sample radius $a_{\mathrm{s}} = 70$ nm is 0.04 (shown with $\log_{10}|\kappa| = -1.39$).

It is worth noting that a chirality parameter of the order of $\kappa \sim 10^{-2}$ which corresponds to a specific rotation[1] of $[\alpha]_{\mathrm{D}} \sim 1000000^{\mathrm{o}}$ is still a giant value compared to that obtained with chiral

[1] Specific rotation is defined as the optical rotation in degrees per decimeter divided by the density of optically active material in grams per cubic centimeter [1].

molecules such as Glucose (C6H12O6), Carvone ($C_{10}H_{14}O$), Testosterone ($C_{19}H_{28}O_2$), etc., with a chirality parameter of the order of $\kappa \sim 10\text{-}6$[58]–[61] (which corresponds to a specific rotation in the order of $[\alpha]_D \sim (100\text{-}200)^o$). This giant chirality is only observed in a few molecules and compounds such as helicene or Norbornenone with specific rotation angles of the order of $[\alpha]_D \sim 1000000^o$ [62], [63]. However, we emphasize that our technique, in contrast with conventional chiroptical techniques, is capable of detecting such molecules when the size of a sample is in the order of ~100nm. The detection of chiral samples with smaller chirality parameter requires some extra considerations, like an increase of the incident power which is possible in cryogenic conditions [64] or in liquids to maintain the condition of gold coated tip [65]–[67] or using nanotips with stronger electric polarizability, or even explore nanotips able to express magnetic response.

Notice, on the other extreme side of the studied ranges of parameters, the smallest detectable radius for a sample with maximum chirality parameter $|\kappa| = 1$ (shown with $\log_{10}|\kappa| = 0$) is 25 nm.

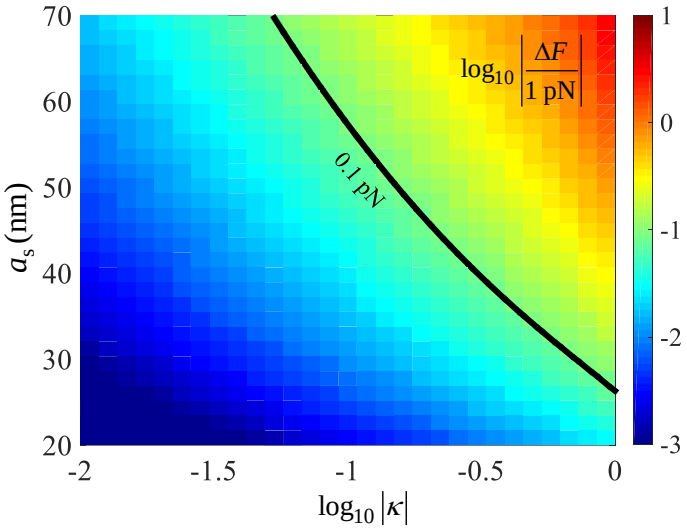

FIG. 2-6. Illustration of the sensitivity of our proposed technique. $\log_{10}|\Delta F / 1\text{pN}|$ is shown versus chirality parameter and radius of the sample.

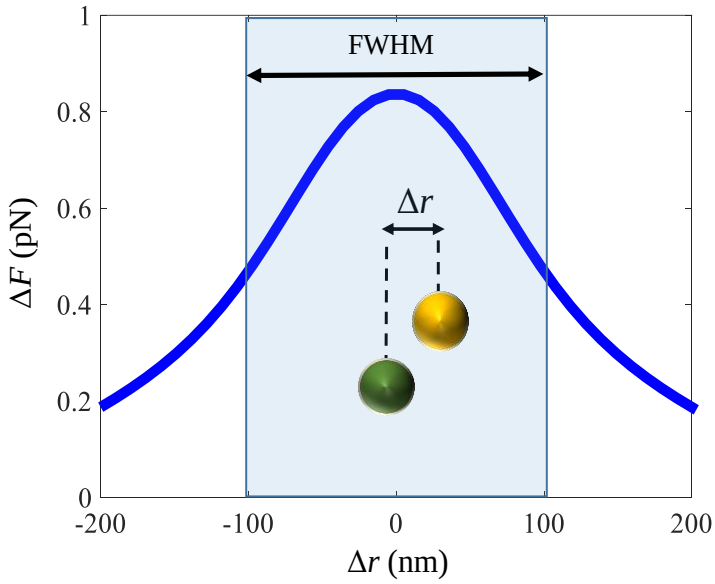

FIG. 2-7. ΔF versus lateral displacement of the tip versus sample. As the tip moves laterally the differential force decreases.

Next, we investigate the transverse resolution of the proposed PiFM technique by observing the detectability range of the sample by assuming a controlled misalignment of the tip. It is expected that this lateral misalignment will decrease the probed differential force. In the

following we estimate the full width at half maximum (FWHM) of the differential force. This is defined as the range of lateral distances between tip and sample in which the differential force is higher than the half of its maximum value (i.e., when the lateral distance between the tip and sample is zero) and shown in Fig. 2-7. In this figure, the differential force is depicted versus the lateral distance between the tip and sample assuming the system parameters as in Fig. 2-2 and $\kappa = 0.6$. As it is expected, when the tip moves laterally (in either direction), the differential *z*-directed force decreases and FWHM of the differential force is 200 nm. This example shows also how far the tip could be to be able to make an enantio-specific detection of chiral nano-samples. One may refer to section VI for more analyses on different parameters influencing the probed differential force such as the relative positioning of the tip-sample interactive system and the excitation beam, the tip-sample gap, the tip radius, etc.

Sec. 2.6 Force dependence on physical parameters

In this section we investigate the dependence of the induced force on the tip on its radius and on the tip-sample relative displacement with respect to the excitation beam. Incident light is assumed to be a CP Gaussian beam propagating along the positive *z*-direction with wavelength $\lambda = 504$ nm and 1mW power. The minimum waist of the Gaussian beam (see Fig.2-1) is positioned at the *z* = 0 plane, where the sample is, because of the higher strength of the field, and the waist parameter is set to $w_0 = 0.7\lambda$ (actual waist is $2w_0$).

A. Tip radius

Here we assume the relative permittivity of the plasmonic tip to be $\varepsilon_t = -3.5 + i0.35$, the sample radius to be $a_s = 60$ nm, and the gap between the tip and sample to be $g = 10$ nm (Fig. 2-

1). The effect of the tip radius a_t on the force difference ΔF between the two adopted CP polarizations is plotted in Fig. 2-8 for various values of the sample chirality parameter κ.

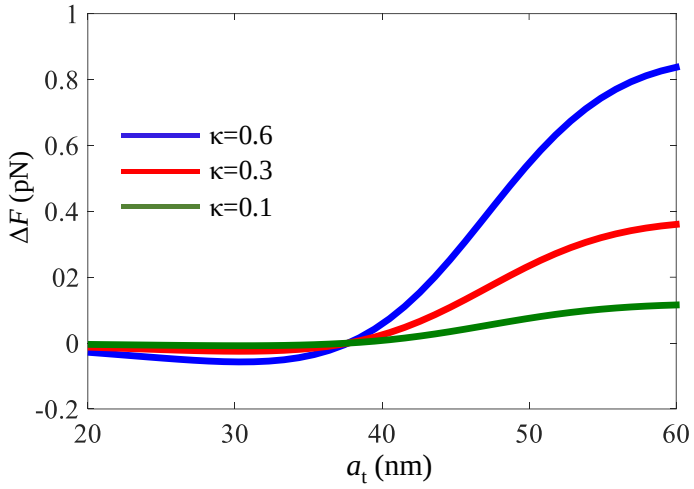

FIG. 2-8 Differential force ΔF for different chirality parameters of the sample as a function of the tip radius with $a_s = 60$ nm, $g = 10$ nm, $\varepsilon_t = -3.5 + i0.35$ and $\varepsilon_s = 2.5$.

It is observed that the differential force ΔF increases for tip radii larger than $a_t = 40$ nm and it is maximum for $a_t = 60$ nm in each κ case. We have not investigated larger values for a_t since the validity range of our analytical model based on dipole approximation dictates to keep the radius of the particles considerably smaller than the operational wavelength (here the largest sphere radius is such that $a_t / \lambda \leq 0.12$). Thus, in order to achieve the maximum distinction in the force between the two incident scenarios, it is better to choose $a_t = 60$ nm for the tip. Further studies could be pursued numerically or using multipole spherical harmonics.

B. Relative displacement of the tip-sample system and the focus of the beam

We now investigate the robustness of the proposed method for enantio-specific detection of chiral nano-samples by observing the sensitivity of the differential force ΔF to the position of the tip-sample interactive system with respect to the minimum waist location (maximum field

strength) of the excitation beam. As we discussed earlier, we are exciting the tip-sample system with CP Gaussian beams with $w_0 = 353\text{nm}$. First we study the effect of lateral displacement h of the minimum waist with respect to the tip-sample system on the differential force ΔF as shown in Fig. 2-9.

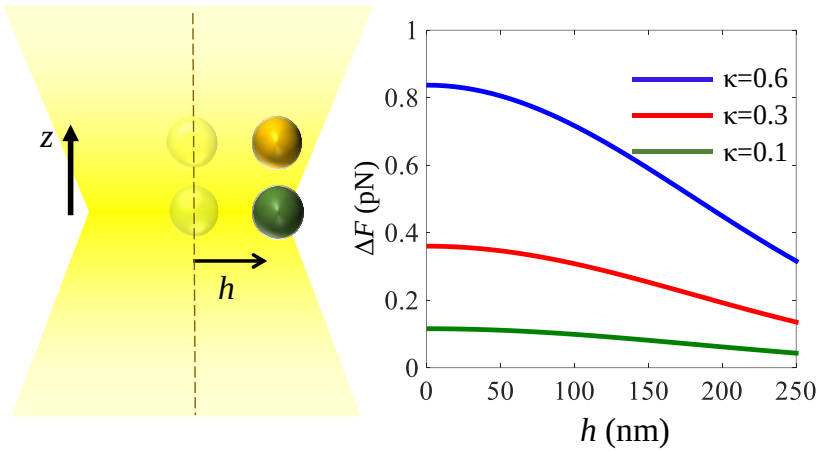

FIG. 2-9 Effect of lateral displacement of the tip-sample system with respect to the beam axis on differential force ΔF for $a_s = a_t = 60$ nm, $g = 10$ nm, $\varepsilon_t = -3.5 + i0.35$ and $\varepsilon_s = 2.5$.

When $h = 0$, the differential force ΔF is maximum and as h increases ΔF decreases because the maximum field strength occurs along the beam axis. However, even with a displacement as large as $h = 250$ nm, samples with chirality parameter as small as $\kappa = 0.1$ could still be detectable depending on the instrument sensitivity.

Next, we provide the results for a longitudinal displacement h of the minimum waist with respect to the tip-sample system as shown in Fig. 2-10.

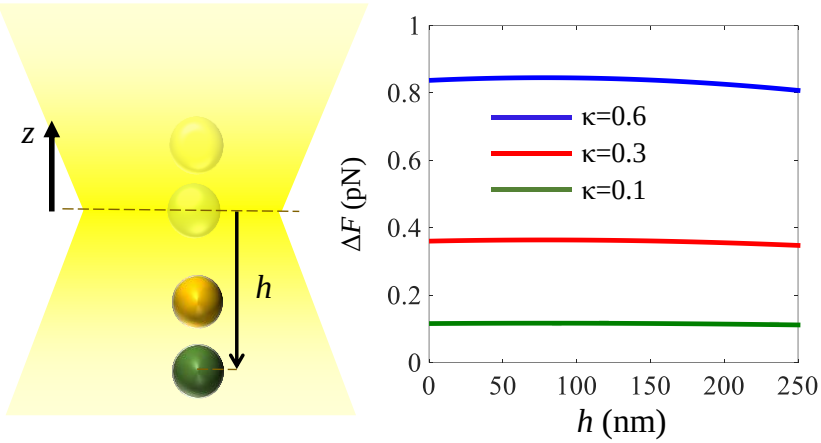

FIG. 2-10 Effect of longitudinal (i.e., vertical) displacement of the minimum waist with respect to the tip-sample interactive system for $a_s = a_t = 60$ nm , $g = 10$ nm , $\varepsilon_t = -3.5 + i0.35$ and $\varepsilon_s = 2.5$.

In this setup, when $h = 0$ the sample is at the minimum beam waist plane, whereas when $h = 130$ nm then the tip is located at the minimum waist. As noticed in Fig. 2-10, the longitudinal displacement of the waist with respect to the tip-sample system does not significantly influence the differential force ΔF since the maximum field strength is either on the sample or on the tip, and the field does not strongly change along the beam axis of a CP Gaussian beam when the waist moves in the upper direction.

Sec. 2.7 Conclusion

We have introduced the concept of photo-induced force microscopy for enantiomer-specific detection of nanoscale chiral samples. Although we use the same excitations as applied in standard CD and ROA scenarios for detecting chirality (i.e., two CP beams with opposite handedness), the idea of using such beams in photo-induced force microscopy enables an unprecedented method for detection of chiral samples down to nanoscale resolution and sample size. That is to say, we can specify the enantiomer type of a chiral particle (with a radius as small as 25 nm) with chirality parameter as small as $\kappa = 0.04$ with nanometric resolution. We have

demonstrated how an achiral plasmonic AFM tip effectively interacts with chiral nano-samples to enhance the probing force (that is in a measurable range) by providing an analytical formalism to predict the exerted force on the tip.

In a future study we plan to implement the proposed approach in an experimental set-up for the enantiomeric detection of chiral samples. We also discuss how the use of properly engineered nano-antennas with both electric and magnetic responses could maximize the measured force, hence, enabling the detection of even smaller particles or weaker chirality than the one assumed here.

Appendix A Mie polarizabilities for a chiral sphere

The chiral tensorial parameter $\underline{\boldsymbol{\kappa}}$ is defined via the constitutive relations [41]

$$\begin{aligned} \mathbf{D} &= \varepsilon_0 \underline{\boldsymbol{\varepsilon}} \cdot \mathbf{E} + i\sqrt{\varepsilon_0 \mu_0}\, \underline{\boldsymbol{\kappa}} \cdot \mathbf{H} \\ \mathbf{B} &= \mu_0 \underline{\boldsymbol{\mu}} \cdot \mathbf{H} - i\sqrt{\varepsilon_0 \mu_0}\, \underline{\boldsymbol{\kappa}}^{\mathrm{T}} \cdot \mathbf{E}, \end{aligned} \tag{2.A1}$$

which provide the connection between the electric field $\mathbf{E}$, magnetic field $\mathbf{H}$, magnetic induction $\mathbf{B}$, and electric displacement vector $\mathbf{D}$. The chirality tensor $\underline{\boldsymbol{\kappa}}$ provides an average measure of handedness of inclusions composing the bulk in accordance with the role of $\underline{\boldsymbol{\varepsilon}}$ and $\underline{\boldsymbol{\mu}}$ in the material constitutive relations (2.A1). Notice that the coefficient $\sqrt{\varepsilon_0 \mu_0}$ is introduced to make the chirality tensor $\underline{\boldsymbol{\kappa}}$ dimensionless as ε_0 and μ_0 are introduced to make the tensors $\underline{\boldsymbol{\varepsilon}}$ and $\underline{\boldsymbol{\mu}}$ dimensionless. It is shown in [41] that chirality originates from a first order spatial dispersion in material.

For a small (at the wavelength scale) sphere with radius a, and isotropic materials parameters $\underline{\boldsymbol{\varepsilon}} = \varepsilon_S \underline{\mathbf{I}}$, $\underline{\boldsymbol{\mu}} = \mu_S \underline{\mathbf{I}}$ and $\underline{\boldsymbol{\kappa}} = \kappa \underline{\mathbf{I}}$ located in free space, we approximate the electromagnetic response

with only dipolar terms whose electric, magnetic, and magnetoelectric polarizabilities $\alpha_{\mathrm{s}}^{ee}, \alpha_{\mathrm{s}}^{mm}$, and α_{s}^{em} are simply related to the material parameters via the Mie scattering as [68]

$$\alpha_{\mathrm{s}}^{ee} = -6i\pi\varepsilon_0 \frac{a_1}{k^3}, \quad \alpha_{\mathrm{s}}^{mm} = -6i\pi\mu_0 \frac{b_1}{k^3}, \quad \alpha_{\mathrm{s}}^{em} = 6\pi\sqrt{\varepsilon_0\mu_0}\frac{c_1}{k^3}. \tag{2.A2}$$

Here k is the free space wavenumber and coefficients a_1, b_1 and c_1 are given by

$$\begin{aligned}
a_1 &= -\frac{1}{\Delta} i\left(1-a_R a_L\right)\left(X_L X_R Y_2 Y_4 + U_L U_R Y_1 Y_3\right) + \\
&\left(X_L U_R + X_R U_L\right)\left(a_L \mu_0 \frac{\omega Y_1 Y_4}{k} + k a_R \frac{Y_2 Y_3}{\omega\mu_0}\right) \\
b_1 &= -\frac{1}{\Delta} i\left(1-a_R a_L\right)\left(X_L X_R Y_2 Y_4 + U_L U_R Y_1 Y_3\right) \times \\
&\qquad \left(a_L \mu_0 \frac{\omega Y_2 Y_3}{k} + k a_R \frac{Y_1 Y_4}{\omega\mu_0}\right) \\
c_1 &= \frac{1}{\Delta}\Delta_1\left(Y_2 Y_3 - Y_1 Y_4\right)
\end{aligned} \tag{2.A3}$$

In the above equations, ω is the angular frequency and Δ, Δ_1, Y_1 to Y_4, X_L, X_R, U_L, U_R, a_L and a_R are given by

$$\begin{cases}
\Delta = i\left(1-a_R a_L\right)\left(X_L X_R Y_4^2 + U_L U_R Y_3^2\right) + \\
\quad \left(X_L U_R + X_R U_L\right)\left(a_L \mu_0 \dfrac{\omega}{k} + \dfrac{k a_R}{\omega\mu_0}\right) Y_3 Y_4 \\
\Delta_1 = X_L U_R + a_R a_L U_L X_R
\end{cases} \tag{2.A4}$$

$$\begin{cases} Y_1 = \dfrac{\sin(ka)}{ka} - \dfrac{\cos(ka)}{ka} \\ Y_2 = \dfrac{1}{ka}\left(\dfrac{\cos(ka)}{ka} - \dfrac{\sin(ka)}{(ka)^2} + \sin(ka) \right) \\ Y_3 = \left(\dfrac{-i}{(ka)^2} - \dfrac{1}{ka} \right) e^{ika} \\ Y_4 = \dfrac{1}{ka}\left(\dfrac{i}{(ka)^2} + \dfrac{1}{ka} - i \right) e^{ika} \end{cases} \tag{2.A5}$$

$$\begin{cases} X_R = \dfrac{\sin(k_R a)}{(k_R a)^2} - \dfrac{\cos(k_R a)}{k_R a} \\ X_L = \dfrac{\sin(k_L a)}{(k_L a)^2} - \dfrac{\cos(k_L a)}{k_L a} \end{cases} \tag{2.A6}$$

$$\begin{cases} U_R = \dfrac{1}{k_R a}\left(\dfrac{\cos(k_R a)}{k_R a} - \dfrac{\sin(k_R a)}{(k_R a)^2} + \sin(k_R a) \right) \\ U_L = \dfrac{1}{k_L a}\left(\dfrac{\cos(k_L a)}{k_L a} - \dfrac{\sin(k_L a)}{(k_L a)^2} + \sin(k_L a) \right) \end{cases} \tag{2.A7}$$

$$\begin{cases} a_R = -i\dfrac{1}{\omega\varepsilon_1}\left(k_R\left(1-\beta^2\omega^2\varepsilon_1\mu_1\right) + \beta\omega^2\varepsilon_1\mu_1 \right) \\ a_L = -i\dfrac{1}{\omega\varepsilon_1}\left(k_L\left(1-\beta^2\omega^2\varepsilon_1\mu_1\right) - \beta\omega^2\varepsilon_1\mu_1 \right) \end{cases} \tag{2.A8}$$

In the above equations, $\varepsilon_1 = \varepsilon_0\varepsilon_s$, $\mu_1 = \mu_0\mu_s$ are the sphere's permittivity and permeability whereas β is the phenomenological coefficient related to chirality parameter as

$$\beta = \frac{\kappa}{\omega\sqrt{\varepsilon_1\mu_1}}. \tag{2.A9}$$

Moreover k_R and k_L are the chiral sphere's wavenumbers for right and left hand CP waves, respectively, and given by

$$\begin{cases} k_R = \omega\sqrt{\varepsilon_1\mu_1}\left(1-\beta\omega\sqrt{\varepsilon_1\mu_1}\right)\dfrac{1}{1-\beta^2\omega^2\varepsilon_1\mu_1} \\ k_L = \omega\sqrt{\varepsilon_1\mu_1}\left(1+\beta\omega\sqrt{\varepsilon_1\mu_1}\right)\dfrac{1}{1-\beta^2\omega^2\varepsilon_1\mu_1} \end{cases} \tag{2.A10}$$

Appendix B: Differential optical force exerted on the tip

We show here the steps that lead to the approximate formula in Eq. (2.8) for the differential exerted force on the tip in the near field region of a chiral sample when the tip-sample system is excited by CP plane waves with opposite handedness. The expression for the time-averaged optical force exerted on the achiral tip modeled as two coexisting electric and magnetic dipoles $\mathbf{p}_{\mathrm{t}}$ and $\mathbf{m}_{\mathrm{t}}$ is given in Eq. (2.3) where $\mathbf{E}^{\mathrm{loc}}(\mathbf{r}_{\mathrm{t}})$ and $\mathbf{H}^{\mathrm{loc}}(\mathbf{r}_{\mathrm{t}})$ are the local electric and magnetic fields (phasors) at the tip position. They are defined as

$$\begin{aligned} \mathbf{E}^{\mathrm{loc}}\left(\mathbf{r}_{\mathrm{t}}\right) &= \mathbf{E}^{\mathrm{inc}}\left(\mathbf{r}_{\mathrm{t}}\right) + \mathbf{E}_{\mathrm{scat}}\big|_{\mathrm{s}\to\mathrm{t}}, \\ \mathbf{H}^{\mathrm{loc}}\left(\mathbf{r}_{\mathrm{t}}\right) &= \mathbf{H}^{\mathrm{inc}}\left(\mathbf{r}_{\mathrm{t}}\right) + \mathbf{H}_{\mathrm{scat}}\big|_{\mathrm{s}\to\mathrm{t}}, \end{aligned} \tag{2.B1}$$

in which $\mathbf{E}^{\mathrm{inc}}$ and $\mathbf{H}^{\mathrm{inc}}$ are the incident (i.e., external) electric and magnetic fields evaluated at the tip location. Furthermore, $\mathbf{E}_{\mathrm{scat}}\big|_{\mathrm{s}\to\mathrm{t}}$ and $\mathbf{H}_{\mathrm{scat}}\big|_{\mathrm{s}\to\mathrm{t}}$ are the scattered fields generated by the sample at the tip position. Despite all the calculations in this chapter use all the dynamic terms of the Green's function [42], here we approximate the scattered fields by an electric $\mathbf{p}$ and a magnetic $\mathbf{m}$ dipole in the near field region by retaining only the stronger term [69]

$$\begin{aligned}\mathbf{E}_{\text{scat}} &\approx \frac{e^{ikr}}{4\pi\varepsilon_0 r^3}\left[3\hat{\mathbf{r}}\left(\hat{\mathbf{r}}\cdot\mathbf{p}\right)-\mathbf{p}\right],\\ \mathbf{H}_{\text{scat}} &\approx \frac{e^{ikr}}{4\pi\mu_0 r^3}\left[3\hat{\mathbf{r}}\left(\hat{\mathbf{r}}\cdot\mathbf{m}\right)-\mathbf{m}\right],\end{aligned} \tag{2.B2}$$

in which $\hat{\mathbf{r}} = \mathbf{r}/r$ is the unit vector of the radial direction in spherical coordinates centered at the source location, $\mathbf{r}$ is the vector from the source to the observation point and k is the ambient wavenumber. Consequently, the scattered fields due to sample at the tip position are simply rewritten as

$$\begin{aligned}\mathbf{E}_{\text{scat}}\big|_{\text{s}\to\text{t}} &= -\frac{G}{\varepsilon_0}\left[p_{\text{s},x}\hat{\mathbf{x}} + p_{\text{s,y}}\hat{\mathbf{y}} - 2p_{\text{s,z}}\hat{\mathbf{z}}\right],\\ \mathbf{H}_{\text{scat}}\big|_{\text{s}\to\text{t}} &= -\frac{G}{\mu_0}\left[m_{\text{s},x}\hat{\mathbf{x}} + m_{\text{s,y}}\hat{\mathbf{y}} - 2m_{\text{s,z}}\hat{\mathbf{z}}\right],\end{aligned} \tag{2.B3}$$

in which

$$G = \frac{e^{ik|z_{\text{t}}-z_{\text{s}}|}}{4\pi\left|z_{\text{t}}-z_{\text{s}}\right|^3}. \tag{2.B4}$$

Note that subscripts *x*, *y* and *z* are representing the related components in the Cartesian coordinates, z_{t} and z_{s} are the tip and sample positions, respectively.

The electric and magnetic dipole moments of the sample, assumed to have isotropic polarizability, are calculated as

$$\begin{aligned}\mathbf{p}_{\text{s}} &= \alpha_{\text{s}}^{ee}\mathbf{E}^{\text{loc}}\left(z_{\text{s}}\right) + \alpha_{\text{s}}^{em}\mathbf{H}^{\text{loc}}\left(z_{\text{s}}\right),\\ \mathbf{m}_{\text{s}} &= \alpha_{\text{s}}^{me}\mathbf{E}^{\text{loc}}\left(z_{\text{s}}\right) + \alpha_{\text{s}}^{mm}\mathbf{H}^{\text{loc}}\left(z_{\text{s}}\right),\end{aligned} \tag{2.B5}$$

Moreover, the magnetic dipole moment associated to a current density in a given volume is defined as $\mathbf{m} = \frac{1}{2}\mu_0\int dv\,\mathbf{r}\times\mathbf{J}$, with $\mathbf{J}$ and $\mathbf{r}$ being the volumetric current and the position vector

in the same volume, respectively. Next, by using Eqs. (2.B3) and (2.B5), the local fields at the tip location in Eq. (2.B1) are found to be

$$\begin{bmatrix} E_x^{\mathrm{loc}}(z_\mathrm{t}) \\ E_y^{\mathrm{loc}}(z_\mathrm{t}) \\ E_z^{\mathrm{loc}}(z_\mathrm{t}) \end{bmatrix} = \begin{bmatrix} E_x^{\mathrm{inc}}(z_\mathrm{t}) \\ E_y^{\mathrm{inc}}(z_\mathrm{t}) \\ E_z^{\mathrm{inc}}(z_\mathrm{t}) \end{bmatrix} - \frac{G}{\varepsilon_0} \begin{bmatrix} \alpha_\mathrm{s}^{ee} E_x^{\mathrm{loc}}(z_\mathrm{s}) + \alpha_\mathrm{s}^{em} H_x^{\mathrm{loc}}(z_\mathrm{s}) \\ \alpha_\mathrm{s}^{ee} E_y^{\mathrm{loc}}(z_\mathrm{s}) + \alpha_\mathrm{s}^{em} H_y^{\mathrm{loc}}(z_\mathrm{s}) \\ -2\alpha_\mathrm{s}^{ee} E_z^{\mathrm{loc}}(z_\mathrm{s}) - 2\alpha_\mathrm{s}^{em} H_z^{\mathrm{loc}}(z_\mathrm{s}) \end{bmatrix}, \tag{2.B6}$$

$$\begin{bmatrix} H_x^{\mathrm{loc}}(z_\mathrm{t}) \\ H_y^{\mathrm{loc}}(z_\mathrm{t}) \\ H_z^{\mathrm{loc}}(z_\mathrm{t}) \end{bmatrix} = \begin{bmatrix} H_x^{\mathrm{inc}}(z_\mathrm{t}) \\ H_y^{\mathrm{inc}}(z_\mathrm{t}) \\ H_z^{\mathrm{inc}}(z_\mathrm{t}) \end{bmatrix} - \frac{G}{\mu_0} \begin{bmatrix} \alpha_\mathrm{s}^{me} E_x^{\mathrm{loc}}(z_\mathrm{s}) + \alpha_\mathrm{s}^{mm} H_x^{\mathrm{loc}}(z_\mathrm{s}) \\ \alpha_\mathrm{s}^{me} E_y^{\mathrm{loc}}(z_\mathrm{s}) + \alpha_\mathrm{s}^{mm} H_y^{\mathrm{loc}}(z_\mathrm{s}) \\ -2\alpha_\mathrm{s}^{me} E_z^{\mathrm{loc}}(z_\mathrm{s}) - 2\alpha_\mathrm{s}^{mm} H_z^{\mathrm{loc}}(z_\mathrm{s}) \end{bmatrix}, \tag{2.B7}$$

where the local electric and magnetic fields at the sample position can be obtained by

$$\begin{aligned} \mathbf{E}^{\mathrm{loc}}(z_\mathrm{s}) &= \mathbf{E}^{\mathrm{inc}}(z_\mathrm{s}) + \mathbf{E}_{\mathrm{scat}}\big|_{\mathrm{t}\to\mathrm{s}}, \\ \mathbf{H}^{\mathrm{loc}}(z_\mathrm{s}) &= \mathbf{H}^{\mathrm{inc}}(z_\mathrm{s}) + \mathbf{H}_{\mathrm{scat}}\big|_{\mathrm{t}\to\mathrm{s}}, \end{aligned} \tag{2.B8}$$

in which $\mathbf{E}_{\mathrm{scat}}\big|_{\mathrm{t}\to\mathrm{s}}$ and $\mathbf{H}_{\mathrm{scat}}\big|_{\mathrm{t}\to\mathrm{s}}$ are the electric and magnetic fields scattered by the tip at the sample position and similar to Eq. (2.B3) are calculated by

$$\mathbf{E}_{\text{scat}}\big|_{\text{t}\to\text{s}} = -\frac{G}{\varepsilon_0}\Big[\, p_{\text{t},x}\hat{\mathbf{x}} + p_{\text{t,y}}\hat{\mathbf{y}} - 2\,p_{\text{t,z}}\hat{\mathbf{z}}\Big],$$
$$\mathbf{H}_{\text{scat}}\big|_{\text{t}\to\text{s}} = -\frac{G}{\mu_0}\Big[\, m_{\text{t},x}\hat{\mathbf{x}} + m_{\text{t,y}}\hat{\mathbf{y}} - 2m_{\text{t,z}}\hat{\mathbf{z}}\Big]. \tag{2.B9}$$

Since the tip is achiral, the electric and magnetic dipole moments of the tip read

$$\mathbf{p}_{\text{t}} = \alpha_{\text{t}}^{ee}\mathbf{E}^{\text{loc}}\left(z_{\text{t}}\right),$$
$$\mathbf{m}_{\text{t}} = \alpha_{\text{t}}^{mm}\mathbf{H}^{\text{loc}}\left(z_{\text{t}}\right). \tag{2.B10}$$

Now, combining Eqs. (2.B8)-(2.B10) and considering that the incident CP plane waves (note that in the numerical examples in this chapter, we assumed structures to be illuminated by CP Gaussian beams whereas here, for the sake of simplicity, we assume plane waves) lack *z*-polarized field components, Eqs. (2.B6) and (2.B7) read

$$\begin{bmatrix} E_x^{\text{loc}}\left(z_{\text{t}}\right) \\ E_y^{\text{loc}}\left(z_{\text{t}}\right) \end{bmatrix} = \begin{bmatrix} E_x^{\text{inc}}\left(z_{\text{t}}\right) \\ E_y^{\text{inc}}\left(z_{\text{t}}\right) \end{bmatrix} - \frac{G}{\varepsilon_0}\times$$
$$\begin{bmatrix} \alpha_{\text{s}}^{ee}\left(E_x^{\text{inc}}\left(z_{\text{t}}\right) - \dfrac{G}{\varepsilon_0}\alpha_{\text{t}}^{ee}E_x^{\text{loc}}\left(z_{\text{t}}\right)\right) + \alpha_{\text{s}}^{em}H_x^{\text{inc}}\left(z_{\text{t}}\right) \\ \alpha_{\text{s}}^{ee}\left(E_y^{\text{inc}}\left(z_{\text{t}}\right) - \dfrac{G}{\varepsilon_0}\alpha_{\text{t}}^{ee}E_y^{\text{loc}}\left(z_{\text{t}}\right)\right) + \alpha_{\text{s}}^{em}H_y^{\text{inc}}\left(z_{\text{t}}\right) \end{bmatrix}, \tag{2.B11}$$

and

$$\begin{bmatrix} H_x^{\text{loc}}\left(z_{\text{t}}\right) \\ H_y^{\text{loc}}\left(z_{\text{t}}\right) \end{bmatrix} = \begin{bmatrix} H_x^{\text{inc}}\left(z_{\text{t}}\right) \\ H_y^{\text{inc}}\left(z_{\text{t}}\right) \end{bmatrix} - \frac{G}{\mu_0}\times$$
$$\begin{bmatrix} \alpha_{\text{s}}^{me}\left(E_x^{\text{inc}}\left(z_{\text{t}}\right) - \dfrac{G}{\varepsilon_0}\alpha_{\text{t}}^{ee}E_x^{\text{loc}}\left(z_{\text{t}}\right)\right) + \alpha_{\text{s}}^{mm}H_x^{\text{inc}}\left(z_{\text{t}}\right) \\ \alpha_{\text{s}}^{me}\left(E_y^{\text{inc}}\left(z_{\text{t}}\right) - \dfrac{G}{\varepsilon_0}\alpha_{\text{t}}^{ee}E_y^{\text{loc}}\left(z_{\text{t}}\right)\right) + \alpha_{\text{s}}^{mm}H_y^{\text{inc}}\left(z_{\text{t}}\right) \end{bmatrix}. \tag{2.B12}$$

The *z*-component of the local fields at the tip location are not shown above since it is vanishing. In obtaining the above equations, we have used the assumption that at resonance of the chiral sample the following approximation holds $\alpha_{\mathrm{s}}^{ee}\alpha_{\mathrm{s}}^{mm} \approx \alpha_{\mathrm{s}}^{me}\alpha_{\mathrm{s}}^{em}$ [70]–[72]. This is a good approximation for most dipole scatterers close to their resonance and when both the electric and magnetic dipole response originate from the same equation of motion for charge. Next, by simplifying Eqs. (2.B11) and (2.B12), for the *x*-component of the electric and magnetic fields we get

$$E_x^{\mathrm{loc}}\left(z_{\mathrm{t}}\right) = \frac{1}{1-G^2\dfrac{\alpha_{\mathrm{t}}^{ee}}{\varepsilon_0}\dfrac{\alpha_{\mathrm{s}}^{ee}}{\varepsilon_0}} \times \left[\left(1-G\frac{\alpha_{\mathrm{s}}^{ee}}{\varepsilon_0}\right)E_x^{\mathrm{inc}}\left(z_{\mathrm{t}}\right) - \frac{\alpha_{\mathrm{s}}^{em}}{\varepsilon_0}H_x^{\mathrm{inc}}\left(z_{\mathrm{t}}\right)\right], \tag{2.B13}$$

and

$$H_x^{\mathrm{loc}}\left(z_{\mathrm{t}}\right) = \left(-G\frac{\alpha_{\mathrm{s}}^{me}}{\mu_0} + \frac{\left(1-G\dfrac{\alpha_{\mathrm{s}}^{ee}}{\varepsilon_0}\right)G^2}{1-G^2\dfrac{\alpha_{\mathrm{t}}^{ee}}{\varepsilon_0}\dfrac{\alpha_{\mathrm{s}}^{ee}}{\varepsilon_0}}\frac{\alpha_{\mathrm{t}}^{ee}}{\varepsilon_0}\frac{\alpha_{\mathrm{s}}^{me}}{\mu_0}\right)E_x^{\mathrm{inc}}\left(z_{\mathrm{t}}\right) + \left(1-G\frac{\alpha_{\mathrm{s}}^{mm}}{\mu_0} - \frac{G^3}{1-G^2\dfrac{\alpha_{\mathrm{t}}^{ee}}{\varepsilon_0}\dfrac{\alpha_{\mathrm{s}}^{ee}}{\varepsilon_0}}\frac{\alpha_{\mathrm{t}}^{ee}}{\varepsilon_0}\frac{\alpha_{\mathrm{s}}^{me}}{\mu_0}\frac{\alpha_{\mathrm{s}}^{em}}{\varepsilon_0}\right)H_x^{\mathrm{inc}}\left(z_{\mathrm{t}}\right). \tag{2.B14}$$

Similar expressions can be obtained for the *y*-component of the fields. The incident fields for the CP waves propagating along the *z*-direction are

$$\mathbf{E}^{\text{inc}} = |\mathbf{E}_0| \frac{(\hat{\mathbf{x}} \pm i\hat{\mathbf{y}})}{\sqrt{2}} \mathrm{e}^{ikz}$$
$$\mathbf{H}^{\text{inc}} = \frac{|\mathbf{E}_0|}{\eta_0} \frac{(\mp i\hat{\mathbf{x}} + \hat{\mathbf{y}})}{\sqrt{2}} \mathrm{e}^{ikz} \tag{2.B15}$$

in which +/– signs represent right (upper sign) and left (lower sign) handed CP waves, with electric field magnitude $|\mathbf{E}_0|$. By replacing these incident fields in Eqs. (2.B13) and (2.B14) we find the local fields of the tip and by inserting the values of the local fields in Eq. (2.B10) we obtain the dipole moments. Then, we use Eq. (3) to find the exerted force on the tip. As was emphasized before, we neglect the magnetic dipole moment of the tip in obtaining our approximate formula, thus based on Eq. (3) the differential force is calculated as

$$\Delta F = |\mathbf{E}_0|^2 \, \mathrm{Im}\left\{ \frac{\alpha_{\mathrm{t}}^{ee}}{\sqrt{\varepsilon_0 \mu_0} d} \left(\frac{Num}{Den} \right) \right\}, \tag{2.B16}$$

with

$$Num = \Lambda \left[1 - (1 - ikd) \frac{\alpha_{\mathrm{s}}^{ee}}{4\pi d^3} \right] \frac{\left(\alpha_{\mathrm{s}}^{em}\right)^*}{4\pi d^3} + \left(\Lambda - 3 \frac{\left(\alpha_{\mathrm{t}}^{ee}\right)^*}{2\pi d^3} \right) \left[(1 - ikd) \frac{\left(\alpha_{\mathrm{s}}^{ee}\right)^*}{4\pi d^3} \right] \frac{\alpha_{\mathrm{s}}^{em}}{4\pi d^3}$$
$$Den = \left[1 - \frac{\left(\alpha_{\mathrm{t}}^{ee}\right)^*}{4\pi d^3} \frac{\left(\alpha_{s}^{ee}\right)^*}{4\pi d^3} \right]^2 \left[1 - \frac{\alpha_{\mathrm{t}}^{ee}}{4\pi d^3} \frac{\alpha_{\mathrm{s}}^{ee}}{4\pi d^3} \right] \tag{2.B17}$$

where

$$\Lambda = (3 + 2ikd) + (3 + 4ikd) \frac{\left(\alpha_{\mathrm{t}}^{ee}\right)^*}{4\pi d^3} \frac{\left(\alpha_{\mathrm{s}}^{ee}\right)^*}{4\pi d^3}, \tag{2.B18}$$

Note that in the calculation of Eq. (2.B16) we take the gradients of electric and magnetic field vectors $\mathbf{E}^{\mathrm{loc}}$ and $\mathbf{H}^{\mathrm{loc}}$. In Cartesian coordinates, the gradient of a representative vector A is defined as

$$\nabla\mathbf{A} = \begin{bmatrix} \partial_x \mathrm{A}_x & \partial_y \mathrm{A}_x & \partial_z \mathrm{A}_x \\ \partial_x \mathrm{A}_y & \partial_y \mathrm{A}_y & \partial_z \mathrm{A}_y \\ \partial_x \mathrm{A}_z & \partial_y \mathrm{A}_z & \partial_z \mathrm{A}_z \end{bmatrix}.$$

Next, considering the quasi-static limit by assuming $kd \to 0$ and neglecting the terms that contain polarizability power orders higher than the second, Eq. (2.B16) simplifies to Eq. (8). When either the tip or the sample is lossless Eq. (8) is further simplified to

$$\Delta F \approx -\frac{3\left|\mathbf{E}_0\right|^2}{4\pi d^4\sqrt{\varepsilon_0\mu_0}}\mathrm{Re}\left\{\alpha_{\mathrm{t}}^{ee}\right\}\mathrm{Im}\left\{\alpha_{\mathrm{s}}^{em}\right\}. \tag{2.B19}$$

We recall that $\alpha_{\mathrm{s}}^{em} = -\alpha_{\mathrm{s}}^{me}$, and that under the assumption of negligible sample losses α_{s}^{me} is purely imaginary [41].

Appendix C: Equivalent representation of effective polarizability of the tip

In Sec. 1.4 we explained how optical activity is transferred from a chiral sample to an achiral tip thanks to their near field coupling. Here we show the details that lead to Eq. (13). We first insert Eqs. (11) and (12) into Eq. (10). Then, based on Eq. (7), the induced force on the tip in the *z*-direction reads

$$F_{\mathrm{z}}^{\pm} = \frac{\left|\mathbf{E}_0\right|^2}{2\left|\alpha_{\mathrm{t}}^{ee}\right|^2}\mathrm{Re}\left\{\alpha_{\mathrm{t}}^{ee}\left(\hat{\alpha}^{\pm}\frac{\partial\left(\hat{\alpha}^{\pm}\right)^*}{\partial z} - ik\left|\hat{\alpha}^{\pm}\right|^2\right)\right\}, \tag{2.C1}$$

where the + and – signs represent right and left handed CP waves, respectively. In Eq. (2.C1) we have defined the effective polarizability parameter $\hat{\alpha}^{\pm}$ for the right/left CP wave as

$$\hat{\alpha}^{\pm} = \hat{\alpha}_{\mathrm{t}}^{ee} \mp i\hat{\alpha}_{\mathrm{t}}^{em}. \tag{2.C2}$$

where $\hat{\alpha}_{\mathrm{t}}^{ee}$ and $\hat{\alpha}_{\mathrm{t}}^{em}$ are defined in Eqs. (11) and (12). Therefore, the differential force is calculated as

$$\Delta F = F_z^{RCP} - F_z^{LCP} = \frac{\left|\mathbf{E}_0\right|^2}{2\left|\alpha_{\mathrm{t}}^{ee}\right|^2} \mathrm{Re}\left\{ \alpha_{\mathrm{t}}^{ee} \left(\hat{\alpha}^{+} \frac{\partial\left(\hat{\alpha}^{+}\right)^*}{\partial z} - \hat{\alpha}^{-} \frac{\partial\left(\hat{\alpha}^{-}\right)^*}{\partial z} \right) \right\} \Bigg|_{z=z_{\mathrm{t}}} . \tag{2.C3}$$

The derivative is taken with respect to the observation *z*-coordinate (i.e., the tip location). Now, inserting Eq. (2.C2) into Eq. (2.C3) leads to Eq. (13).

CHAPTER 3 : UNSCRAMBLING STRUCTURED CHIRALITY WITH STRUCTURED LIGHT AT THE NANOSCALE USING PHOTOINDUCED FORCE

Sec. 3.1 Motivation

Structure determination of chiral specimens is of great interest since the fundamental building blocks of life, i.e., proteins and nucleic acids are built of chiral amino acids and chiral sugar [1]. Indeed, the optical activity of chiral structures, is a key parameter in molecular identification techniques to recognize the type of a molecule or to determine its structure thanks to the discriminatory behavior of chiral molecules in interaction with the incident light possessing distinct sense of polarization [12], [13]. For instance, for a protein, determining the structure refers to resolving its four levels of complexity, i.e., primary, secondary, tertiary and quaternary which defines not only the sequence of amino acids but also reveals the three dimensional arrangement of atoms in that protein [73]. This information is of supreme importance in modifying and utilizing proteins for new purposes such as creating protein-based anti-body drug conjugates for cancer treatment or modifying the proteins in the bread [74]–[78]. To determine the structure of chiral samples such as protein, noninvasive spectroscopic techniques based on optical rotation (OR), circular dichroism (CD), and Raman optical activity (ROA) have been proposed and vastly studied [3]–[5], [79]. In these methods, owing to the optical activity of chiral structures, the difference between the absorbed left-hand and right-hand circularly polarized (CP) light is measured and not only the chirality but also some important information about the structure of chiral sample is obtained [7]–[9]. Specifically using CD, one can approximate the secondary structure of a protein.

However, the main limitations of this method are as following: (i) it is unable of providing high resolution structural details and (ii) it demands considerable amount of the material for detection. These limitations mainly originate from the fact that CD measures the averaged far-field radiation which misses the essential information only carried in near field, thus, this dearth calls for possible potent near-field measurement techniques which are more promising for providing nanoscale details.

In this chapter, by taking the advantage of PiFM concept, we propose a new technique to determine the longitudinal and transverse chirality components of specimens with high resolution. Unlike CD, this method has high spatial resolution of sub 100-nm-scale. In particular, we calculate the exerted force on the tip in the vicinity of a test sample to identify the different components of the sample handedness which are identified through the magnetoelectric polarizability (or equivalently chirality parameter). Specifically, we prove that proper excitations for detection of transverse (with respect to the propagation direction) components of sample chirality in our proposed method are CP waves since they possess field components transverse to the direction of propagation. Despite this capability, we unravel the failure of CP waves in detecting the longitudinal (i.e., along the propagation direction) component of sample chirality. We particularly prove that a light beam with longitudinal electric or (and) magnetic field component(s) would be an appropriate candidate for the detection of longitudinal chirality component. In this context, optical vortices with longitudinal electric or magnetic field component along the vortex axis[80] serve as suitable practical excitations. With the goal of detection of longitudinal component of chirality and in order to optimize the interaction between the chiral sample and the excitation, we propose a combination of an azimuthally and a radially polarized beam (APB and RPB)[81]–[83] with an appropriate phase difference as the illumination. Indeed, vortex beams have been brought

up as a potent tool in engineering the light-matter interaction [84], [85]. As we prove, our proposed technique for the excitation and probing longitudinal chirality component provides a fundamental advantage in experiments when we are limited to illumination from one side which is common and applied in most PiFM cases.

This chapter is structured as follows: First, we demonstrate the operation principle of our proposed method by applying the dipolar approximation technique. Then we exhibit CP excitations to detect the transverse components of the sample handedness (or equivalently magnetoelectric polarizability), and show how they fail in probing the longitudinal chirality component. Next, we bring up the idea of superposition of an APB and an RPB as a suitable excitation scenario for detecting the longitudinal component of the sample handedness which was unrecognizable under the CP excitation. Lastly, we conclude this chapter with some remarks.

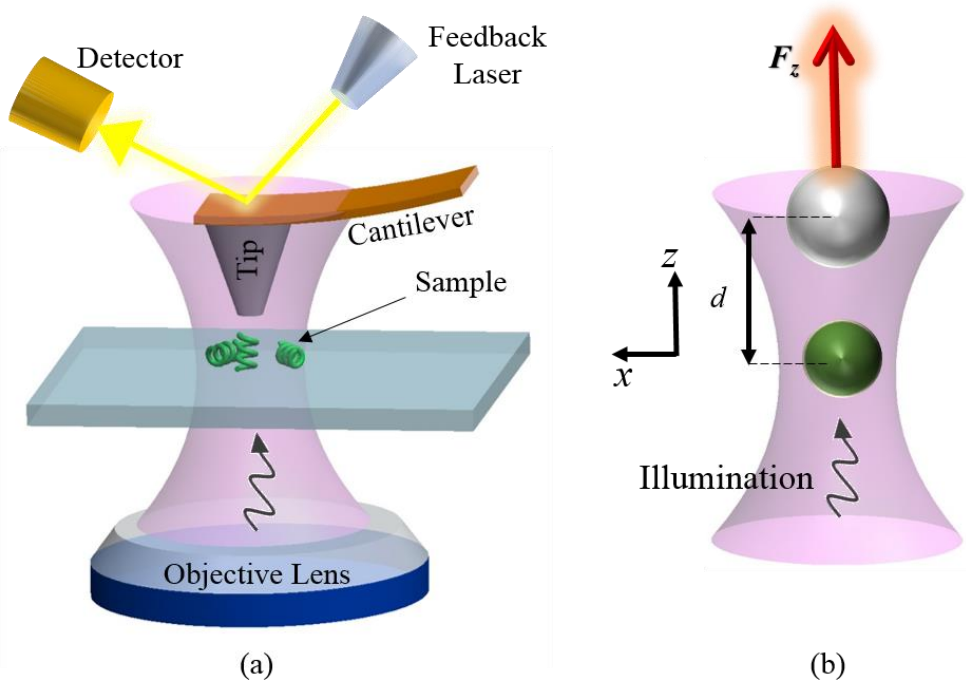

FIG. 3-1. (a) Schematic of photo-induced force microscopy capable of probing different components of the handedness of a chiral sample particle. (b) Simplified model where the tip-apex and sample are

represented by nanospheres with electric (and perhaps magnetic) dipole moment(s). We investigate electromagnetic forces due to near-field interaction between the two nanostructures, the plasmonic tip and the chiral sample, under external illumination with structured chiral light. The transverse components refer to the *x* and *y* directions whereas the longitudinal one refers to the *z* direction.

Sec. 3.2 Objective and operational principle

Figure 3-1 depicts the PiFM set-up which is utilized throughout this chapter for both the transverse and longitudinal chirality investigations. As it is shown, the interactive system composed of a nanoscale chiral sample and the microscope tip is illuminated by incident focused light propagating along the positive *z* direction (referred here as the longitudinal direction) from the bottom side through an objective lens. The incident beam induces electric and perhaps magnetic polarization currents on both the sample and tip-apex which consequently provide secondary scattered electromagnetic waves. In the PiFM technique, the sample and tip-apex are supposed to be close enough (compared to the operational wavelength), so that they interact through each other's near-zone scattered fields. That is why a noticeable force is exerted on the tip-apex due to the transfer of momentum from the scattered photons. We are specifically interested in the force exerted on the tip-apex in the longitudinal direction (*z*-direction in Fig. 3-1) since it can be measured using a PiFM. Moreover, as discussed previously, unlike conventional chiroptical techniques such as CD for detecting chirality, PiFM is capable of detecting chirality at nanoscale since it exploits the information carried in the near-field scattered by the sample. It is important to mention that the nanoscale sample does not need to be in a solution, but it can be tethered to the tip or on the substrate, for which the orientation of the sample can be controlled [86], [87].

We assume both tip-apex and sample to be small compared to the wavelength of incident light so that their main interaction feature is modeled via dipoles' near-field scattering. In our

theoretical analysis and for the proof of concept, we approximate the tip-apex and sample as two nanospheres and model the tip-apex by equivalent electric and magnetic dipoles, as already done in chapter 2 and the chiral sample by its bianisotropic polarizability and use the dipole approximation to investigate their interaction (see Fig 3-1 (b)). Note that this dipolar approximation has successfully been exploited to model photo-induced force microscopy in Refs. [36], [38], [88], [89] to extract optical properties of samples. Here, we model the sample with its photo-induced electric and magnetic dipole moments $\mathbf{p}$ and $\mathbf{m}$ as in chapter 1 (see Eq. (2.1) and Eq. (2.2)). Note that throughout this thesis the magnetic dipole moment is defined as $\mathbf{m} = \mu_0 \int_V dv\, \mathbf{r} \times \mathbf{J} / 2$, with **J** and **r** being the volumetric current density and the position vector in volume V, respectively, and μ_0 is the vacuum permeability. This definition (that includes μ_0) provides the same units for the electromagnetic and magnetoelectric polarizabilities $\underline{\boldsymbol{\alpha}}^{em}$, and $\underline{\boldsymbol{\alpha}}^{me}$ and is chosen following Ref.[89]. See chapter I of Refs.[41], [90], [91] for a detailed discussion about bianisotropic particles, and also a summary in the Supporting Information. To summarize, a chiral particle must possess two specific properties in terms of the induced moment and the incident field: a) it should be bi-isotropic (or bianisotropic), that is, the electric (magnetic) dipole response must be induced by the incident magnetic (electric) field, and b) the induced electric and magnetic dipole moments **p** and **m** must be parallel. For chiral particles the magnetoelectric and electromagnetic polarizability tensors reduce to a single one since $\underline{\boldsymbol{\alpha}}^{me} = -\left(\underline{\boldsymbol{\alpha}}^{em}\right)^T$ (which is true for any reciprocal particle, see Supporting Information) where T is the tensor transpose and in particular they are diagonal. The magnetoelectric polarizability tensor of a particle in Cartesian coordinates is represented by the matrix

$$\underline{\boldsymbol{\alpha}}^{em} = \begin{bmatrix} \alpha_{xx}^{em} & \alpha_{xy}^{em} & \alpha_{xz}^{em} \\ \alpha_{xx}^{em} & \alpha_{yy}^{em} & \alpha_{yz}^{em} \\ \alpha_{zx}^{em} & \alpha_{zy}^{em} & \alpha_{zz}^{em} \end{bmatrix}. \tag{3.1}$$

In this thesis, we investigate reciprocal chiral particles, that is, magnetoelectric polarizability is diagonal, having only α_{xx}^{em} , α_{yy}^{em} or α_{zz}^{em} as non-vanishing components. Since the propagation direction of the incident field in our set-up is along the *z*-axis, in the following we refer to the first two polarizability components α_{xx}^{em} and α_{yy}^{em} as the transverse components and the last component α_{zz}^{em} as the longitudinal one.

As we discussed, the goal is to characterize the transverse and longitudinal magnetoelectric polarizabilities of a chiral nanoparticle by exploiting different structured light illumination scenarios and by exploring the exerted force on the tip in the vicinity of the chiral sample. Note that in our set-up, we employ an achiral tip-apex, i.e., $\underline{\alpha}_{\mathrm{t}}^{me} = \underline{\alpha}_{\mathrm{t}}^{em} = 0$ $\underline{\alpha}_{\mathrm{t}}^{me} = \underline{\alpha}_{\mathrm{t}}^{em} = 0$. Accordingly, the local electric and magnetic fields at the tip position are described by

$$\begin{aligned} \mathbf{E}^{\mathrm{loc}}\left(\mathbf{r}_{\mathrm{t}}\right) &= \mathbf{E}^{\mathrm{inc}}\left(\mathbf{r}_{\mathrm{t}}\right) + \underline{\mathbf{G}}^{\mathrm{EE}}\left(\mathbf{r}_{\mathrm{t}}, \mathbf{r}_{\mathrm{s}}\right) \cdot \mathbf{p}_{\mathrm{s}} + \underline{\mathbf{G}}^{\mathrm{EM}}\left(\mathbf{r}_{\mathrm{t}}, \mathbf{r}_{\mathrm{s}}\right) \cdot \mathbf{m}_{\mathrm{s}}, \\ \mathbf{H}^{\mathrm{loc}}\left(\mathbf{r}_{\mathrm{t}}\right) &= \mathbf{H}^{\mathrm{inc}}\left(\mathbf{r}_{\mathrm{t}}\right) + \underline{\mathbf{G}}^{\mathrm{ME}}\left(\mathbf{r}_{\mathrm{t}}, \mathbf{r}_{\mathrm{s}}\right) \cdot \mathbf{p}_{\mathrm{s}} + \underline{\mathbf{G}}^{\mathrm{MM}}\left(\mathbf{r}_{\mathrm{t}}, \mathbf{r}_{\mathrm{s}}\right) \cdot \mathbf{m}_{\mathrm{s}}. \end{aligned} \tag{3.2}$$

here $\underline{\mathbf{G}}^{\mathrm{EE}}$ and $\underline{\mathbf{G}}^{\mathrm{ME}}$ are the dyadic Green's functions that provide the electric and magnetic fields due to an electric dipole $\mathbf{p}_{\mathrm{s}}$, whereas $\underline{\mathbf{G}}^{\mathrm{EM}}$ and $\underline{\mathbf{G}}^{\mathrm{MM}}$ are the dyadic Green's functions that provide the electric and magnetic fields due to a magnetic dipole $\mathbf{m}_{\mathrm{s}}$, respectively[42], [69], [92]. The Green's functions include all the near-field and radiative terms, used in the numerical simulations, though the analytic results are based on the quasi static approximation (see Supporting Information) that depends on the cubic distance between the tip and the sample.

In this chapter, we employ right and left handed CP Gaussian beams as excitation for probing the transverse component of the sample's magnetoelectric polarizability. However, we prove that the CP illumination scenario is unable of identifying the longitudinal component of the magnetoelectric polarizability. Consequently, for the detection of longitudinal component of the magnetoelectric polarizability, we propose an alternative illumination scheme based on a combination of an APB and RPB with a proper phase difference. The reason is that such combination exclusively interacts with the electric and magnetic dipoles of the sample in the longitudinal direction, interacting with the sample's longitudinal chirality, whereas CP waves that propagate along the longitudinal direction lack such characteristic. Note that the dipolar approximation validity range for various inclusions and within different wavelength ranges has been investigated in Refs.[93], [94], and as shown in these studies, it successfully predicts the electromagnetic response (i.e., force and scattering) of small inclusions and acceptably provides a physical trend and insight for optically large inclusions within a specific wavelength range.

Moreover, it has been shown that knowing electric and magnetic polarizability, it is sufficient to determine the longitudinal and transverse polarizability by 6 illuminations and measurements [95], however, it requires a more complicated experimental set-up and special cares about the phases of exciting beams compared to our proposal.

Sec. 3.3 Probing the transverse handedness of chiral samples

As discussed, CP beams are used as excitation in our proposed PiFM set-up. Specifically, we first send a right-hand CP (RCP) beam and then a left hand CP (LCP) beam and calculate the *z*-directed exerted force on the tip-apex in the vicinity of the sample for each case. For an achiral sample, the calculated forces exerted on the tip-apex are equal for both excitation scenarios. However, owing to the optical activity of chiral materials and their rotational asymmetry, a chiral

sample reacts differently under illuminations with opposite sense of handedness (here RCP and LCP). This distinction is manifested in the exerted force on the tip-apex. Note that we use the general expression of the time-averaged optical force exerted on the tip which is given in Eq. (2.3) of chapter 2.

As our first example, we consider an example when the test sample and the plasmonic tip-apex are illuminated with a CP Gaussian beam propagating along the z-direction with a 1mW incident power at a wavelength of $\lambda = 400$ nm . We assume that the waist of the Gaussian beam is $w_0 = 0.7\lambda$ (note that the actual waist of the beam is $2w_0$ [81]). Moreover, the sample is placed at the minimum waist *z*-plane of the beam (which hereafter we call beam waist) due to the higher strength of the field. For simplicity and in order to demonstrate the capability of our proposed method, we first assume that the sample is isotropic, i.e., $\underline{\boldsymbol{\alpha}}_{\mathrm{s}}^{em} = \alpha_{\mathrm{s}}^{em}\underline{\mathbf{I}}$ and spherical. The chirality of the sample is denoted by the chirality parameter κ which describes the degree of handedness of a material [89] and here we vary it from -1 to 1. The tip-apex is also assumed to be isotropic and spherical and both the sample and the tip-apex are considered to have equal radii $a_{\mathrm{s}} = a_{\mathrm{t}} = 50$ nm with center-to-center distance of $d = 110$ nm (see Fig. 3-2). Furthermore, without loss of generality and for the proof of concept, the relative permittivity of the sample is assumed to be $\varepsilon_{\mathrm{s}} = 2.4$ whereas that of the plasmonic tip-apex is assumed to be $\varepsilon_{\mathrm{t}} = -3.6 + i0.19$ (this is the relative permittivity of silver at the operational wavelength). In Fig. 3-2, we have depicted the *z*-component of the exerted force on the plasmonic tip-apex versus chirality parameter of the sample for both RCP and LCP incident waves using Eq. (5). The results clearly exhibit the potential of our proposed method in the detection of sample chirality at nanoscale. We define the time-averaged differential force along the *z* direction as $\Delta F_z = F_{\mathrm{z}}^{RCP} - F_{\mathrm{z}}^{LCP}$, i.e., the difference

between the *z*-component of the exerted force on the tip-apex when the illumination is, respectively, an RCP and an LCP wave. This differential force is able to separate the effect of chirality of the sample from its other properties, i.e., electric and perhaps magnetic (represented by the electric and magnetic polarizabilities). As it is illustrated in Fig. 3-2, the exerted differential force on the tip-apex for an achiral sample, i.e. $\kappa = 0$, is zero, however, as the magnitude of the chirality parameter of the sample grows, the differential force exerted on the tip-apex increases. Though in all the figures, results are obtained considering also the small force contribution due to the negligible magnetic dipole of the tip-apex as in Eq. (2.3) in the following we provide simple formulas obtained by neglecting such contribution. In this regard, the *z*-component of the general force expression of Eq. (2.3) reduces to (see Eq. 2.2 of Ref. [96], and Eq. (6) of Ref. [97]) $F_z = \frac{1}{2}\mathrm{Re}\left[\left(\partial E_x^{\mathrm{loc}}(z)/\partial z\right)^*_{z=z_t} p_{\mathrm{t},x} + \left(\partial E_y^{\mathrm{loc}}(z)/\partial z\right)^*_{z=z_t} p_{\mathrm{t},y}\right]$. Furthermore, neglecting the field's phase difference between the tip-apex and sample, due to their subwavelength distance, it is shown that the difference between the forces exerted on the tip-apex for two CP plane wave illuminations with opposite handedness reads [89], [98], [99]

$$\Delta F_z \approx -\frac{3|\mathbf{E}_0|^2}{4\pi\sqrt{\varepsilon_0\mu_0}d^4}\,\mathrm{Im}\left\{\alpha_{\mathrm{t}}^{ee}\left(\alpha_{\mathrm{s}}^{em}\right)^*\right\}. \tag{3.3}$$

in which d is the center-to-center distance between the sample and tip-apex. Note that in deriving this formula, we assume CP plane waves with electric field magnitude $|\mathbf{E}_0|$ on the beam axis since it simplifies our analytical calculations. Gaussian beams with a large beam waist can be reliably approximated by plane waves around their beam axis. Note that the optical force calculated in Eq. (3.3) modifies the vibration of the cantilever in the PiFM system and the cantilever dynamics is comprehensively studied in Ref.[37]. First, Eq. (3.3) clearly demonstrates that the differential

force depends linearly on the electric polarizability of the tip-apex, hence, the material, size and shape of the tip-apex play crucial roles in determining the differential force. Specifically, in a previous study[89] the importance of the shape and material of the tip-apex has been further discussed [44], [45], [54], [100].

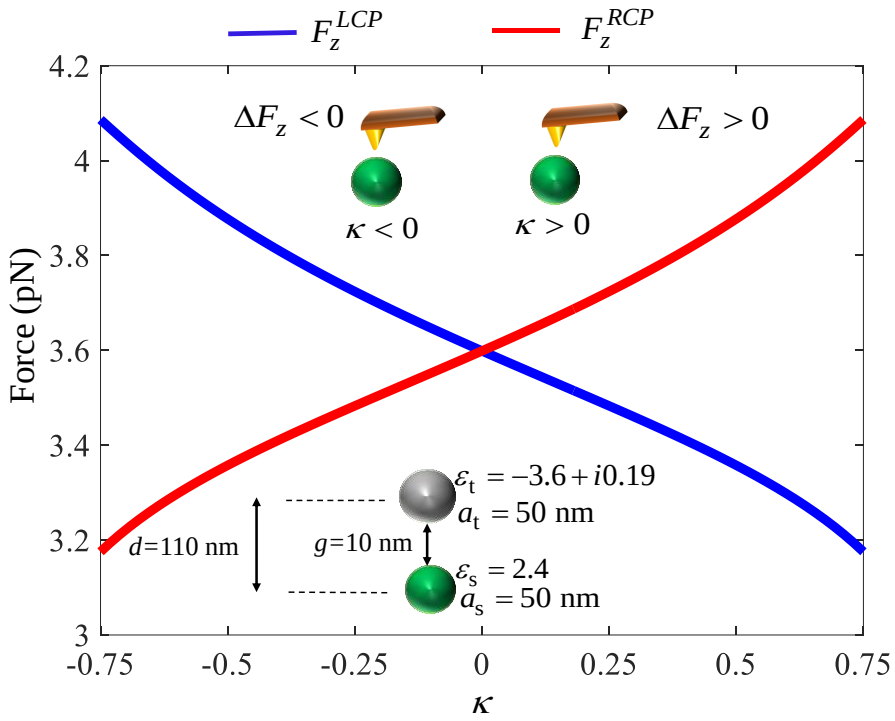

FIG. 3-2. The exerted force on the tip-apex for two incident scenarios of RCP and LCP illumination. Here, a and ε represent radius and permittivity, respectively.

So far, we have shown the ability of our proposed technique to detect and characterize isotropic chiral particles, i.e, particles with $\alpha_{s,xx}^{em} = \alpha_{s,yy}^{em} = \alpha_{s,zz}^{em}$ at nanoscale. However, as we have already discussed, it would be interesting to investigate the capability of our proposed excitation scenario (RCP/LCP waves) in distinguishing between the transverse and longitudinal components of the magnetoelectric polarizability. To that end, we note that the magnetoelectric polarizability tensor of the sample, in Cartesian coordinates is represented by the matrix

$$\underline{\boldsymbol{\alpha}}_{\mathrm{s}}^{em}=\begin{bmatrix}\alpha_{\mathrm{s},xx}^{em} & 0 & 0\\ 0 & \alpha_{\mathrm{s},yy}^{em} & 0\\ 0 & 0 & \alpha_{\mathrm{s},zz}^{em}\end{bmatrix}. \tag{3.4}$$

We assume here the exciting beam and the tip-apex have the same parameters as in the previous example related to Fig. 3-2. We study two different cases with samples' polarizabilities given by: 1) and $\alpha_{\mathrm{s},zz}^{em}=0$; and 2) $\alpha_{\mathrm{s},zz}^{em}\neq 0$ and $\alpha_{\mathrm{s},xx}^{em}=\alpha_{\mathrm{s},yy}^{em}=0$. In this work we do not distinguish between the two transverse polarizability components $\alpha_{\mathrm{s},xx}^{em}$ and $\alpha_{\mathrm{s},yy}^{em}$, but we only distinguish between the transverse (i.e., $\alpha_{\mathrm{s},xx}^{em}$ and $\alpha_{\mathrm{s},yy}^{em}$) and longitudinal ($\alpha_{\mathrm{s},zz}^{em}$) polarizability components of the sample nanoscatterer. In Fig. 3-3 we have depicted the *z*-component of the differential force versus nonzero component of magnetoelectric polarizability for each case normalized to the magnetoelectric polarizability of the isotropic sample sphere studied in Fig. 3-2 with $\kappa=0.75$, i.e. $\alpha_{\mathrm{s,iso}}^{em}(\kappa=0.75)$. (An analytic expression of such a polarizability for a chiral sphere is shown in Ref.[89] based on Ref.[68]) As it is clear, for a chiral sample with any nonzero transverse polarizability we can detect chirality with RCP and LCP illuminations since $\Delta F_{\mathrm{z}}\neq 0$. However, for samples with only longitudinal magnetoelectric polarizability (with vanishing transverse magnetoelectric polarizability components) we are not able to characterize chirality with CP since $\Delta F_{\mathrm{z}}=0$. To clarify the reason of the failure of CP excitation in detecting longitudinal chirality component, we note that under paraxial approximation the *z*-components of the local fields, both at the tip-apex and sample location vanish for any excitation field that lacks the *z*-component (see Supporting Information). This means that the longitudinal component of the

magnetoelectric polarizability does not contribute to the calculation of the electric and magnetic dipole moments in Eq. (2.1), and hence, in the calculation of exerted force on the tip-apex in Eq. (2.3) . To clarify this issue, note that by using Eq. (3.4), we expand Eq. (2.1) as

$$\begin{aligned}\mathbf{p}_{\mathrm{s}} &= \underline{\boldsymbol{\alpha}}_{\mathrm{s}}^{ee}\cdot\mathbf{E}^{\mathrm{loc}}\left(\mathbf{r}_{\mathrm{s}}\right)+\hat{\mathbf{x}}\alpha_{\mathrm{s},xx}^{em}H_{x}^{\mathrm{loc}}\left(\mathbf{r}_{\mathrm{s}}\right)+\hat{\mathbf{y}}\alpha_{\mathrm{s},yy}^{em}H_{y}^{\mathrm{loc}}\left(\mathbf{r}_{\mathrm{s}}\right)+\hat{\mathbf{z}}\alpha_{\mathrm{s},zz}^{em}H_{z}^{\mathrm{loc}}\left(\mathbf{r}_{\mathrm{s}}\right),\\ \mathbf{m}_{\mathrm{s}} &= \underline{\boldsymbol{\alpha}}_{\mathrm{s}}^{mm}\cdot\mathbf{H}^{\mathrm{loc}}\left(\mathbf{r}_{\mathrm{s}}\right)+\hat{\mathbf{x}}\alpha_{\mathrm{s},xx}^{me}E_{x}^{\mathrm{loc}}\left(\mathbf{r}_{\mathrm{s}}\right)+\hat{\mathbf{y}}\alpha_{\mathrm{s},yy}^{me}E_{y}^{\mathrm{loc}}\left(\mathbf{r}_{\mathrm{s}}\right)+\hat{\mathbf{z}}\alpha_{\mathrm{s},zz}^{me}E_{z}^{\mathrm{loc}}\left(\mathbf{r}_{\mathrm{s}}\right).\end{aligned} \tag{3.5}$$

It should be mentioned that the electric polarizability of the sample is isotropic, i.e. $\alpha_{\mathrm{s},xx}^{ee}=\alpha_{\mathrm{s},yy}^{ee}=\alpha_{\mathrm{s},zz}^{ee}$ but its magnetoelectric and electromagnetic polarizabilities are not. As it is observed from this equation, although the tip is plasmonic, because of the vanishing *z*-components of the local fields (see appendix B of Ref. [89]), the longitudinal components of both the magnetoelectric and electromagnetic polarizabilities $\alpha_{\mathrm{s},zz}^{me}$ and $\alpha_{\mathrm{s},zz}^{em}$ do not contribute to the determination of the induced electric and magnetic dipole moments of the sample, and hence, they do not contribute to the force calculation in Eq. (2.3). Indeed, based on Eq. (2.3), the exerted force on the tip-apex depends on the induced electric and magnetic dipole moments $\mathbf{p}_{\mathrm{s}}$ and $\mathbf{m}_{\mathrm{s}}$ of the sample through local fields $\mathbf{E}^{\mathrm{loc}}\left(\mathbf{r}_{\mathrm{t}}\right)$ and $\mathbf{H}^{\mathrm{loc}}\left(\mathbf{r}_{\mathrm{t}}\right)$ at the tip-apex position (see Eq. (2.6)). In conclusion, CP wave excitation or any excitation type that lacks the *z*-component of the electric and/or magnetic field would be an improper choice for the characterization of the longitudinal magnetoelectric polarizability component.

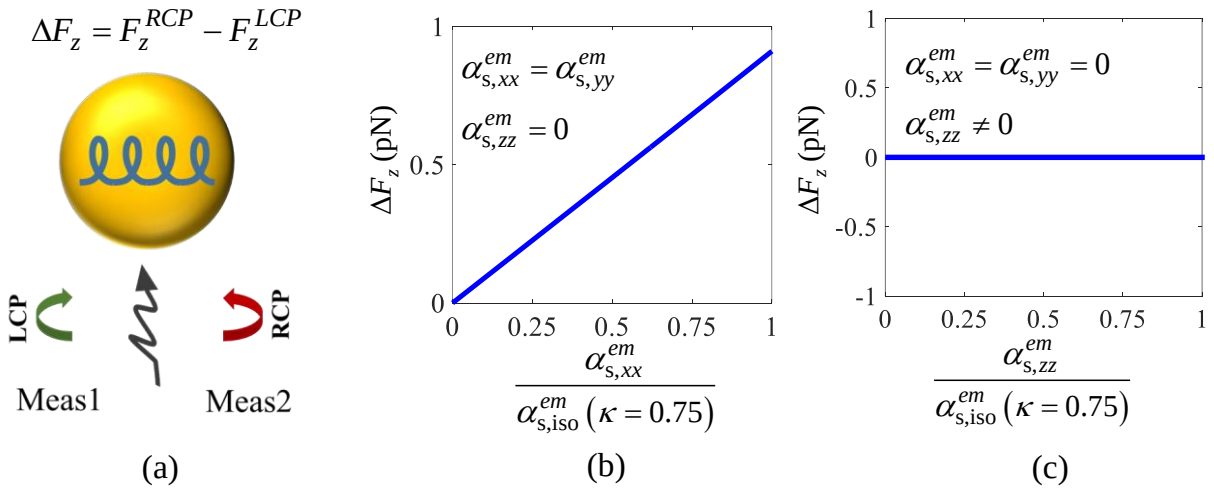

FIG. 3-3. (a) Schematic of appropriate structured light illumination for detection of transverse chirality. Differential force exerted on the tip-apex versus the non-vanishing component of the magnetoelectric polarizability normalized to $\alpha_{s,iso}^{em}(\kappa = 0.75)$ for two different cases: (b) $\alpha_{s,xx}^{em} = \alpha_{s,yy}^{em} \neq 0$ and $\alpha_{s,zz}^{em} = 0$; (c) $\alpha_{s,zz}^{em} \neq 0$ and $\alpha_{s,xx}^{em} = \alpha_{s,yy}^{em} = 0$.

Based on the above discussion, the problem of probing the longitudinal magnetoelectric polarizability component calls for utilizing alternative types of beam illuminations which is the subject of the next section.

Sec. 3.4 Probing the longitudinal handedness of chiral samples

As was explained in the previous section, it is infeasible to detect the longitudinal component of the sample's magnetoelectric polarizability since the CP exciting field lacks the longitudinal field components. It is worth mentioning here that one may use CP waves which are incident obliquely with respect to the transverse plane (here, the *x*-*y* plane), and hence, providing field components in the *z*-direction (i.e., longitudinal direction in our formalism). However, utilizing a single oblique illumination results in the simultaneous presence of both the transverse

and longitudinal field components and make it impossible to distinguish the transverse and longitudinal polarizability components. Furthermore, in the scenario of oblique illumination, in order to create a purely longitudinal field component we require to illuminate the tip-sample system from both sides which requires more complicated experimental set-up and special cares about the phases of exciting beams compared to our proposal.

Therefore, in order to exclusively determine the longitudinal component of the magnetoelectric polarizability it is essential to utilize illuminating beams that exclusively possess longitudinal electric and/or magnetic field components without the transverse components. Moreover, for the reason of experimental convenience, it is desirable to use beams that excite the sample from the bottom side of the surface where the sample is located, as customary in several microscopy systems. As mentioned earlier, APB and RPB are suitable candidates for our purpose since they have either purely longitudinal magnetic or electric field component along their vortex axes, respectively. Indeed, as we show next, we utilize structured light excitation made of a combination of these two beams, with proper phase difference, to retrieve the sample handedness. In other words, we use a superposition of an APB and a RPB [101]–[103] with a specific phase difference ψ (hereafter, we call it the phase parameter) with their electric and magnetic fields given by

$$\begin{aligned} \mathbf{E}^{\mathrm{ARPB}} &= \mathbf{E}^{\mathrm{APB}} e^{i\psi} + \mathbf{E}^{\mathrm{RPB}}, \\ \mathbf{H}^{\mathrm{ARPB}} &= \mathbf{H}^{\mathrm{APB}} e^{i\psi} + \mathbf{H}^{\mathrm{RPB}}, \end{aligned} \tag{3.6}$$

in which $\mathbf{E}^{\mathrm{APB}}$, $\mathbf{H}^{\mathrm{APB}}$, $\mathbf{E}^{\mathrm{RPB}}$ and $\mathbf{H}^{\mathrm{RPB}}$ are the electric and magnetic fields of the APB and RPB, respectively. The electric and magnetic fields of an APB in cylindrical coordinates under paraxial approximation are given by [82]

$$\mathbf{E}^{\mathrm{APB}} = E_{\varphi}\hat{\boldsymbol{\varphi}} = \frac{V}{\sqrt{\pi}}\frac{2\rho}{w^2}e^{-(\rho/w)^2\varsigma}e^{-2i\tan^{-1}(z/z_R)}e^{ik_0 z}\hat{\boldsymbol{\varphi}}, \tag{3.7}$$

$$\mathbf{H}^{\mathrm{APB}} = -\frac{1}{\eta_0}E_{\varphi}\left[1+\frac{1}{k_0 z_R}\frac{\rho^2-2w_0^2}{w^2}\right]\hat{\boldsymbol{\rho}} - \frac{V}{\sqrt{\pi}}\frac{4i}{w^2\omega\mu_0}\left[1-\left(\frac{\rho}{w}\right)^2\zeta\right]e^{-(\rho/w)^2\zeta}e^{-2i\tan^{-1}(z/z_R)}e^{ik_0 z}\hat{\mathbf{z}}, \tag{3.8}$$

in which V is the amplitude coefficient, $\eta_0 = \sqrt{\mu_0/\varepsilon_0}$ is the ambient wave impedance, and z_R (Rayleigh range), ζ and w are given by

$$w = w_0\sqrt{1+\left(\frac{z}{z_R}\right)^2}, \quad \zeta = \left(1-i\frac{z}{z_R}\right), \qquad z_R = \pi\frac{w_0^2}{\lambda}, \tag{3.9}$$

in which w_0 is called the beam parameter and controls the spatial extent of the beam in the transverse plane, i.e., the beam waist (w_0 tends to be the same as the beam waist for non-sharply collimated beams). The power carried by an APB reads [82]

$$P^{\mathrm{APB}} = \frac{|V|^2}{2\eta_0}\left(1-\frac{1}{2(\pi w_0/\lambda)^2}\right). \tag{3.10}$$

It is worth mentioning that in order to obtain Eqs. (11) and (12), we first calculate the transverse electric field with paraxial approximation and subsequently obtain the magnetic field using Maxwell's equation $i\omega\mu_0\mathbf{H} = \nabla\times\mathbf{E}$. For an RPB, the expressions of the electric and magnetic fields read (note that these fields are dual of the APB fields)

$$\mathbf{H}^{\mathrm{RPB}} = H_{\varphi}\hat{\boldsymbol{\varphi}} = -\frac{I}{\sqrt{\pi}}\frac{2\rho}{w^2}e^{-(\rho/w)^2\varsigma}e^{-2i\tan^{-1}(z/z_R)}e^{ik_0 z}\hat{\boldsymbol{\varphi}}, \tag{3.11}$$

$$\mathbf{E}^{\mathrm{RPB}} = -\eta_0 H_{\varphi}\left[1+\frac{1}{k_0 z_R}\frac{\rho^2-2w_0^2}{w^2}\right]\hat{\boldsymbol{\rho}} - \frac{I}{\sqrt{\pi}}\frac{4i}{w^2\omega\varepsilon_0}\left[1-\left(\frac{\rho}{w}\right)^2\zeta\right]e^{-(\rho/w)^2\zeta}e^{-2i\tan^{-1}(z/z_R)}e^{ik_0 z}\hat{\mathbf{z}} \tag{3.12}$$

and I is the amplitude coefficient of the RPB. The power carried by an RPB reads

$$P^{\mathrm{RPB}} = \eta_0 \frac{|I|^2}{2}\left(1-\frac{1}{2\left(\pi w_0/\lambda\right)^2}\right). \tag{3.13}$$

In order to obtain Eqs. (15) and (16), we calculate the transverse magnetic field with paraxial approximation and subsequently obtain the electric field using Maxwell's equation $-i\omega\varepsilon_0\mathbf{E}=\nabla\times\mathbf{H}$. On the axis of an ARPB, i.e., at $\rho=0$, only the longitudinal field components are non-vanishing, and assuming the combined APB and RPB have the same beam parameter w_0 and same focal plane, the fields ratio is

$$\frac{H_z^{\mathrm{ARPB}}}{E_z^{\mathrm{ARPB}}} = \frac{H_z^{\mathrm{APB}}e^{i\psi}}{E_z^{\mathrm{RPB}}} = \frac{1}{\eta_0^2}\frac{V}{I}e^{i\psi}. \tag{3.14}$$

in which H_z^{ARPB} and E_z^{ARPB} represent the *z*-component of the magnetic and electric field of the ARPB, respectively. The magnitude of different electric and magnetic field components of the ARPB has been demonstrated in the Supporting Information for various phase difference parameter ψ. Using the aforementioned combination of the beams with coincident vortex axes (the *z*-axis), assuming each of them (APB and RPB) has 1 mW power at $\lambda = 400\,\mathrm{nm}$, we place the tip-apex and chiral sample with parameters given in Fig. 3-2 along the axis of the two beams, on which the transverse components of the electric and magnetic fields are vanishing whereas the longitudinal components are not. Specifically, we assume the chiral sample to be on the focal plane of the beams due to high field intensity. Furthermore, we consider the beam parameter of both RPB and APB to be $w_0 = 0.7\lambda$. In order to detect the chirality, we change the phase-shift parameter ψ in Eq. (3.10) and calculate the exerted force on the tip-apex for two distinct cases: (a)

a case with azimuthal chirality with $\alpha_{s,xx}^{em} = \alpha_{s,yy}^{em} = \alpha_{s,iso}^{em}(\kappa = 0.75)$ and $\alpha_{s,zz}^{em} = 0$, and b) a case with longitudinal chirality with $\alpha_{s,zz}^{em} = \alpha_{s,iso}^{em}(\kappa = 0.75)$ and $\alpha_{s,xx}^{em} = \alpha_{s,yy}^{em} = 0$, where $\alpha_{s,iso}^{em}(\kappa = 0.75)$ is the magnitude of magnetoelectric polarizability of the isotropic sphere of Fig. 3-2 with $\kappa = 0.75$. In Fig. 3-4 (a) and (b), we have depicted the *z*-component of the force exerted on the tip-apex versus the phase parameter ψ of the ARPB. In all the following figures results are obtained including the small (though negligible) force contribution due to the magnetic polarizability of the tip-apex. We have also assumed that the ARPB has $F_Y = \left|\eta_0 H_z^{\mathrm{APB}} / E_z^{\mathrm{RPB}}\right| = \left|V/(\eta_0 I)\right| = 1$. We recall that the field admittance normalized to the free space wave impedance $F_Y = \left|\eta_0 H_z^{\mathrm{APB}} / E_z^{\mathrm{RPB}}\right|$ was defined previously in Refs. [82], [83], [100]to describe the magnetic to electric field ratio compared to that of a plane wave, since this is an important parameter when light interacts with magnetic dipoles [we discuss the field admittance parameter in more details later in Eq.(3.19)]. As it is clearly observed, with this illumination, it is possible to distinguish between the sample's transverse and longitudinal chirality handedness by investigating the exerted force on the tip-apex by varying the values of phase parameter ψ. Note that the transverse component of the handedness cannot be probed by using this excitation since the exerted force on the tip-apex does not depend on the phase parameter, i.e., swing of the exerted force is zero (see Fig. 3-4(a)).

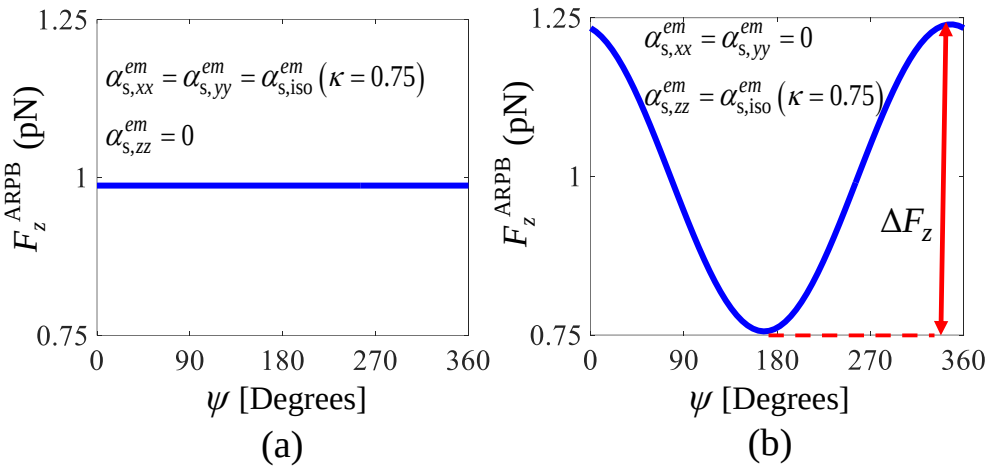

FIG. 3-4. Force exerted on the tip-apex in the *z*-direction when using a combination of phase-shifted APB and ARB, for two cases: (a) Case with $\alpha_{s,xx}^{em} = \alpha_{s,yy}^{em} = \alpha_{s,iso}^{em}\left(\kappa = 0.75\right)$ and $\alpha_{s,zz}^{em} = 0$ that lacks longitudinal chirality; (b) Case with $\alpha_{s,zz}^{em} = \alpha_{s,iso}^{em}\left(\kappa = 0.75\right)$ and $\alpha_{s,xx}^{em} = \alpha_{s,yy}^{em} = 0$, that has only longitudinal chirality. ARPB has $\left|V/\left(\eta_0 I\right)\right| = 1$, i.e., F_Y =1 and *V* and *I* are in phase.

Indeed, we propose to use the "swing" of the exerted force on the tip-apex defined as

$$\Delta F_z = \max\left(F_z^{\mathrm{ARPB}}\right) - \min\left(F_z^{\mathrm{ARPB}}\right) \tag{3.15}$$

where $\max\left(F_z^{\mathrm{ARPB}}\right)$ and $\min\left(F_z^{\mathrm{ARPB}}\right)$ represent the maximum and the minimum of the exerted force on the tip-apex when varying the phase shift parameter ψ, observable in Fig. 3-4(b). These quantities are observed for two phase shift parameters that are 180 degrees apart, i.e. $\left|\psi_{F_z\max} - \psi_{F_z\min}\right| = 180^o$ as shown in Fig. 3-4(b) (see Supporting Information). In summary we propose to use the swing in (19) to calculate longitudinal chirality. We want to quantify the physical properties that determine the force on the tip-apex, in terms of electric and magnetoelectric polarizabilities of the tip-apex and sample, respectively. In the following we provide simple formulas for the *z*-component of the force obtained from Eq. (2.3) by neglecting

the tip-apex magnetic dipole moment, leading to $F_z^{\mathrm{ARPB}} = \mathrm{Re}\left[\left(\partial E_z^{\mathrm{loc}}(z)/\partial \mathrm{z}\right)^*_{z=z_\mathrm{t}} \; p_{\mathrm{t},z}\right]/2$ [96].

The difference between the two optical forces for ARPB illuminations with two different phase parameters ψ_1 and ψ_2 reads (see Supporting Information)

$$F_z^{\mathrm{ARPB}}|_{\psi_2} - F_z^{\mathrm{ARPB}}|_{\psi_1} \approx -\frac{3F_Y |\mathbf{E}_0|^2}{4\pi\sqrt{\varepsilon_0\mu_0}d^4}\left[\mathrm{Re}\left(e^{-i\psi_2}\alpha_\mathrm{t}^{ee}\alpha_{\mathrm{s},zz}^{em\,*}\right) - \mathrm{Re}\left(e^{-i\psi_1}\alpha_\mathrm{t}^{ee}\alpha_{\mathrm{s},zz}^{em\,*}\right)\right]. \tag{3.16}$$

here, $\alpha_{\mathrm{s},zz}^{em}$ is the longitudinal component of the magnetoelectric polarizability of the chiral sample and α_t^{ee} is the electric polarizability of the tip-apex. In the calculation of the above equations we have neglected the field's phase difference between the tip and sample due to their subwavelength distance. Moreover, we have simplified the electric and magnetic field expressions of the illuminating beam at the beam axis (i.e., at $\rho = 0$ since both the tip-apex and sample are placed on the axis of the beam) and have rewritten Eq. (3.6)as

$$\begin{aligned} E^{\mathrm{ARPB}} &= E_z = |\mathbf{E}_0| e^{-2i\tan^{-1}(\mathrm{z}/z_R)} e^{ik_0 z}, \\ H^{\mathrm{ARPB}} &= H_z = \frac{|\mathbf{E}_0|}{\eta_0} e^{-2i\tan^{-1}(\mathrm{z}/z_R)} e^{ik_0 z} e^{i\psi}, \end{aligned} \tag{3.17}$$

where $|\mathbf{E}_0| = 4|I|/\left(\sqrt{\pi}w^2\omega\varepsilon_0\right)$ is the amplitude of the electric field (directed along *z*) at the origin, i.e., at $\rho = 0$ and $\mathrm{z} = 0$, where the sample is located. The swing of the exerted force on the tip-apex by varying the phase parameter ψ of the ARPB, neglecting the losses of the particles and assuming F_Y=1 (i.e., assuming that the powers of APB and RPB are equal, see Eq.(3.19)) is given by the approximate formula (details in the Supporting Information)

$$\Delta F_z \approx -\frac{3|\mathbf{E}_0|^2}{2\pi\sqrt{\varepsilon_0\mu_0}d^4}\mathrm{Re}\left(\alpha_\mathrm{t}^{ee}\right)\mathrm{Im}\left\{\left(\alpha_{\mathrm{s},zz}^{em}\right)^*\right\}. \tag{3.18}$$

In derivation of Eq. (3.18) we have neglected the field's phase delay in the field interaction between the tip-apex and sample, due to their subwavelength distance, i.e., we have used a quasi-static Green's function[89], [104].

Equation (3.18) which is similar to the differential force formula for the CP illumination, demonstrates that the sample's longitudinal magnetoelectric polarizability $\alpha_{s,zz}^{em}$ is determined by exploiting a combination of two vortex beams (the ARPB) and a simple algorithm where the phase shift ψ between the composing APB and ARB is varied.

In Fig. 3-5, we further demonstrate the ability of ARPB in detecting the longitudinal chirality for two cases similar to those in Fig. 3-3: 1) $\alpha_{s,xx}^{em} = \alpha_{s,yy}^{em} \neq 0$ and $\alpha_{s,zz}^{em} = 0$; and 2) $\alpha_{s,zz}^{em} \neq 0$ and $\alpha_{s,xx}^{em} = \alpha_{s,yy}^{em} = 0$. We depict the swing of the *z*-component of the exerted force on the tip-apex versus the nonzero component of the magnetoelectric polarizability, normalized to the magnetoelectric polarizability of the isotropic sample sphere studied in Fig. 3-2 with $\kappa = 0.75$, i.e. $\alpha_{s,iso}^{em}(\kappa = 0.75)$. As one observes, this type of illumination is suitable for characterizing the longitudinal magnetoelectric polarizability $\alpha_{s,zz}^{em}$ since $\Delta F_z \neq 0$ in Fig. 3-5(c). It is noteworthy that the proposed ARPB field combinations with properly designed phases to be used for chirality detection are fields with well-defined helicities [105], [106].

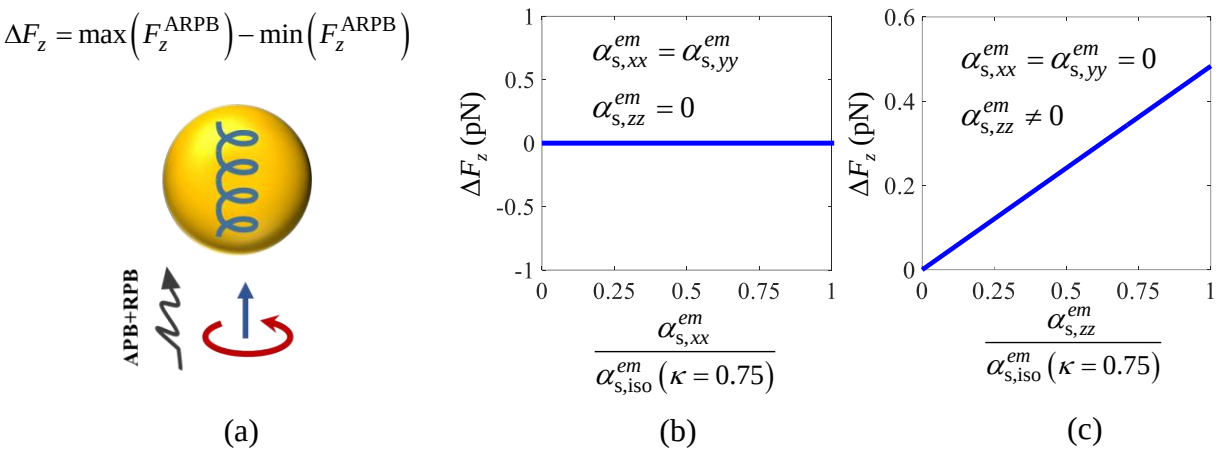

(a) (b) (c)

FIG. 3-5. (a) Schematic of appropriate structured light illumination for detection of longitudinal chirality. Maximum force swing exerted on the tip-apex versus the non-vanishing component of the magnetoelectric polarizability normalized to $\alpha^{em}_{\mathrm{s,iso}}(\kappa = 0.75)$ for two different cases: (b) $\alpha^{em}_{\mathrm{s},xx} = \alpha^{em}_{\mathrm{s},yy} \neq 0$ and $\alpha^{em}_{\mathrm{s},zz} = 0$; (c) $\alpha^{em}_{\mathrm{s},zz} \neq 0$ and $\alpha^{em}_{\mathrm{s},xx} = \alpha^{em}_{\mathrm{s},yy} = 0$. Result in (b) demonstrates the possibility of probing the longitudinal magnetoelectric polarizability $\alpha^{em}_{\mathrm{s},zz}$ using the superposition of an APB and an RPB with proper phase difference.

Figure 3-6 summarizes the main results of the current study in a concise table. It demonstrates different scenarios of illumination beams and test samples. In summary, for samples with longitudinal chirality components, the ARPB is a proper choice, whereas for samples with transverse chirality components, CP beams are suitable. The suitable proposed scenarios are highlighted by a gray color where the differential force is nonzero and the sample's chirality is retrievable from two distinct measurements.

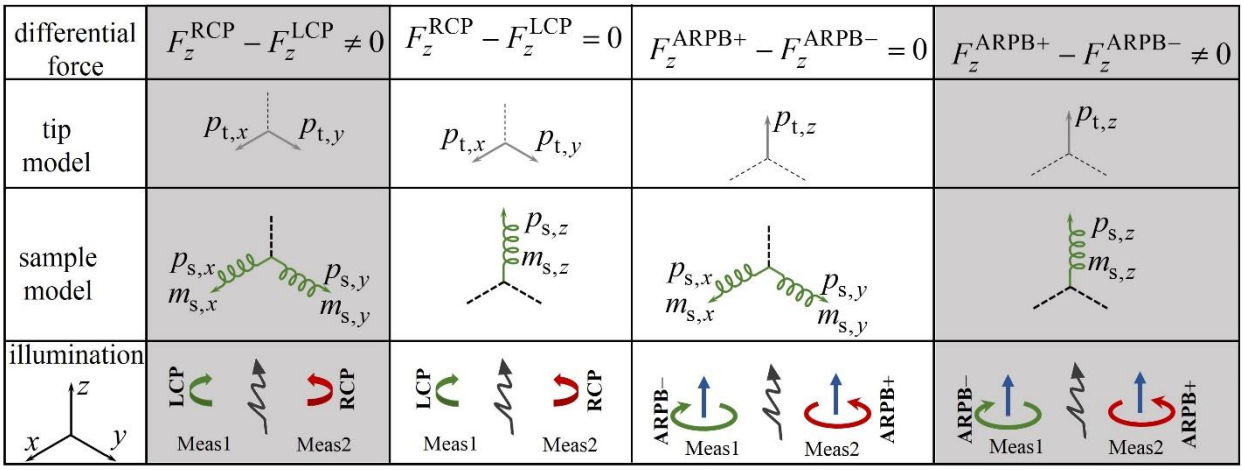

FIG. 3-6. Summary of the suitable proposed illumination type to retrieve chirality of anisotropic chiral samples. In each case two measurements Meas1 and Meas2 are necessary. An experiment with two CP beams is (not) able to determine the transverse (longitudinal) chirality. An experiment with two ARPB is (not) able to determine the longitudinal (transverse) chirality. ARPB+ and ARPB-- represent the two APRBs which lead to $\max\left(F_z^{\mathrm{ARPB}}\right)$ and $\min\left(F_z^{\mathrm{ARPB}}\right)$, respectively. The chirality in each direction is schematized by a helix and the proper choice of excitation is highlighted with a shaded gray area. In all cases the tip-apex is modeled by an electric polarizable dipole and the choice of the excitation influences the direction of the induced dipole on the tip-apex although the tip-apex is isotropic.

In the previous discussion and results we have assumed that $\eta_0 H_z^{\mathrm{APB}} / E_z^{\mathrm{RPB}} = V/(\eta_0 I) = 1$, which means that both the APB and RPB carry the same power (assuming they have the same beam waist) and V and I have the same phase, since the phase difference between these two beams is represented by ψ.

Our final discussion before conclusion is about having different illumination powers of the APB and RPB, and then we justify the choice done beforehand, where $F_Y = 1$, that leads to the best result. Therefore we now assume that the parameter F_Y^2 differs from unity, where F_Y^2 is the figure of merit which shows the ratio between the illumination power of the APB and RPB, previously defined as

$$F_Y^2 = \left|\frac{P^{\mathrm{APB}}}{P^{\mathrm{RPB}}}\right| = \eta_0^2 \left|\frac{H_z}{E_z}\right|^2_{\substack{\rho=0 \\ z=0}} = \frac{1}{\eta_0^2}\left|\frac{V}{I}\right|^2 \tag{3.19}$$

Note that F_Y^2 represents the intensity of the longitudinal magnetic field over the intensity of the longitudinal electric field, at the focus of the beams (i.e., at the chiral sample location). This figure of merit is the squared magnitude of the normalized field admittance introduced in previous studies 31,32,58. We assume that the total power of the APB and RPB exciting beams is constant, and in particular $P^{\mathrm{APB}} + P^{\mathrm{RPB}} = 2\,\mathrm{mW}$ (there is no cross power term since the polarization of the two beams is orthogonal). We also assume that the tip-apex and the sample have the same polarizability characteristics used in the example in Fig. 3-4 (a), i.e., $\alpha_{\mathrm{s},zz}^{em} = \alpha_{\mathrm{s},iso}^{em}\left(\kappa = 0.75\right)$ and $\alpha_{\mathrm{s},xx}^{em} = \alpha_{\mathrm{s},yy}^{em} = 0$. The color map in Fig. 3-7(a) describes the exerted force on the tip-apex versus F_Y^2 (in logarithmic scale) and phase difference ψ between the APB and RPB. One observes that as F_Y^2 increases (increases the ratio between the APB to RPB power, or alternatively the magnetic field increases with respect to the electric field), the exerted force on the tip-apex decreases, for all phase parameters ψ. The reason is that for both the tip-apex and sample, in general the electric responses are stronger than their magnetic counterparts, thus, weaker electric field (larger F_Y^2) leads to weaker observed optical force on the tip-apex. However, it is important to note that for a reliable measurement, the most important property is to observe the largest swing of the force i.e. $\max\left(\Delta F_z\right)$ (note that ΔF_z is defined in Eq.(3.15)) which leads to higher resolution in detection of nanoscale chirality, and this feature may be more interesting than a large observable force. In other words, a stronger force does not necessarily lead to a larger swing force. In Fig. 3-7(b) we have depicted ΔF_z versus F_Y^2 , and we observe that the maximum swing occurs when $F_Y^2 = 1$,

i.e., when the illumination powers of the APB and RPB are equal or equivalently when $|E_z|/|H_z|=\eta_0$ or $|V|/|I|=\eta_0$. Indeed, it can be analytically proved (details in the Supporting Information) that assuming a constant total power of APB and RPB (i.e., a constant power density), the maximum swing occurs when F_Y=1.

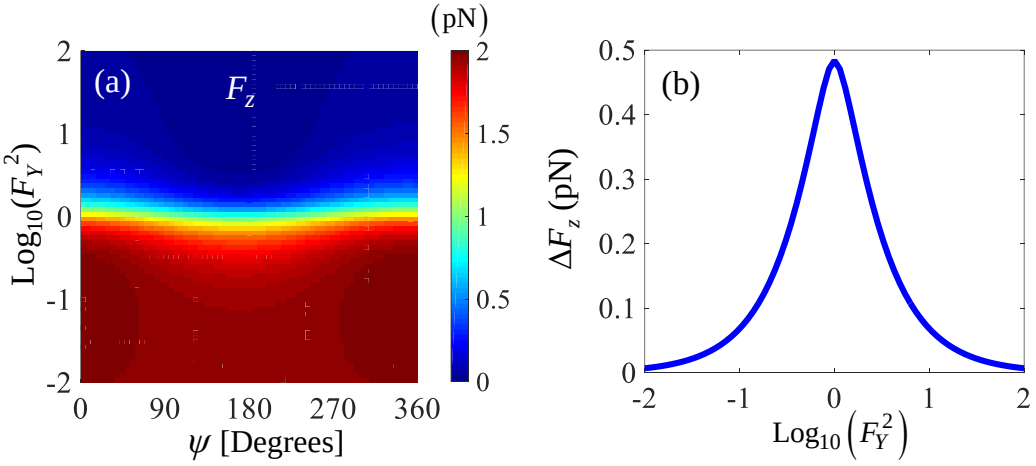

FIG. 3-7. (a) Photo-induced optical force on the tip-apex varying the power distribution between the APB and the RPB, and their phase difference ψ. The force increases with decreasing F_Y^2. (b) Swing of the force versus F_Y^2. In conclusion the maximum swing corresponds to the best possible scenario for longitudinal chirality detection, and it occurs when $F_Y^2=1$, or equivalently when $|E_z|/|H_z|=\eta_0$.

With the above considerations, we conclude the discussion on introducing suitable high resolution approaches to unscramble the chirality structure of a chiral sample. However, future work is necessary to distinguish between the two transverse components of the magnetoelectric polarizability tensor, i.e., $\alpha_{s,xx}^{em}$ and $\alpha_{s,yy}^{em}$. For that azimuthally anisotropic case, excitation types that possess either a pure electric or a pure magnetic field component in the transverse plane i.e., the *xy*-plane, would be useful following the proposed scheme.

Sec. 3.5 Conclusion

Based on the concept of photo-induced optical force, we have presented how different structured-light excitation scenarios result in chirality characterization at nanoscale. We have shown an approach based on force detection to determine not only the enantiomer type of a chiral sample but also to distinguish between its transverse and longitudinal chirality components at nanoscale. Particularly, we have proved that when we are limited to the illumination from the bottom side of the tip-sample system (as shown in Fig. 3-1), probing the transverse sample's chirality requires transverse field components (with respect to the propagation direction) as in CP beams. Instead, probing longitudinal chirality is achievable by using a combination of longitudinal field components, obtained by performing two experiments, each one with a superposition of an APB and an RPB with proper phase shift ψ. There is an underlined difference between CP beams, whose light is chiral, and APBs and RPBs, whose light is not chiral. However combinations of an APB and an RPB leads to chiral light, therefore we propose to use them together with a proper controlled phased shift ψ , and perform two experiments, with two different phase shifts. The difference between these two experiments, denoted as ΔF_z , takes the maximum value when the APB and RPB exhibit the same power density at the chiral sample location. The quantification of the longitudinal and transverse components of the magnetoelectric polarizability helps to unscramble the structure of chiral specimen. This work has the potential to advance studies of chirality of nanosamples and molecular concentrations, since chirality is a fundamental building block of nature.

Appendix A Local fields at the tip and the sample locations under ARPB illumination

We prove that under ARPB excitation the local fields at the tip and sample locations (both on the ARPB axis) lack transverse components and we determine the longitudinal field components that include the near-field interaction between sample and tip. We consider the schematic of the problem in Fig. 3.1 and assume that the tip and sample are located at z_t and z_s, respectively. We start from Eqs. (B6) and (B7) in Ref. [89] which are the local electric and magnetic fields at the position of the tip and generalize them to the case of anisotropic sample. This leads to

$$\begin{bmatrix} E_x^{\mathrm{loc}}(z_t) \\ E_y^{\mathrm{loc}}(z_t) \\ E_z^{\mathrm{loc}}(z_t) \end{bmatrix} = \begin{bmatrix} E_x^{\mathrm{inc}}(z_t) \\ E_y^{\mathrm{inc}}(z_t) \\ E_z^{\mathrm{inc}}(z_t) \end{bmatrix} - \frac{G}{\varepsilon_0} \begin{bmatrix} \alpha_s^{ee} E_x^{\mathrm{loc}}(z_s) + \alpha_{s,xx}^{em} H_x^{\mathrm{loc}}(z_s) \\ \alpha_s^{ee} E_y^{\mathrm{loc}}(z_s) + \alpha_{s,yy}^{em} H_y^{\mathrm{loc}}(z_s) \\ -2\alpha_s^{ee} E_z^{\mathrm{loc}}(z_s) - 2\alpha_{s,zz}^{em} H_z^{\mathrm{loc}}(z_s) \end{bmatrix},$$

(3.A1)

and

$$\begin{bmatrix} H_x^{\mathrm{loc}}(z_t) \\ H_y^{\mathrm{loc}}(z_t) \\ H_z^{\mathrm{loc}}(z_t) \end{bmatrix} = \begin{bmatrix} H_x^{\mathrm{inc}}(z_t) \\ H_y^{\mathrm{inc}}(z_t) \\ H_z^{\mathrm{inc}}(z_t) \end{bmatrix} - \frac{G}{\mu_0} \begin{bmatrix} \alpha_{s,xx}^{me} E_x^{\mathrm{loc}}(z_s) + \alpha_s^{mm} H_x^{\mathrm{loc}}(z_s) \\ \alpha_{s,yy}^{me} E_y^{\mathrm{loc}}(z_s) + \alpha_s^{mm} H_y^{\mathrm{loc}}(z_s) \\ -2\alpha_{s,zz}^{me} E_z^{\mathrm{loc}}(z_s) - 2\alpha_s^{mm} H_z^{\mathrm{loc}}(z_s) \end{bmatrix}, \qquad (3.A2)$$

respectively. We recall that in this chapter the electric polarizability of the sample is isotropic i.e. $\alpha_{s,xx}^{ee} = \alpha_{s,yy}^{ee} = \alpha_{s,zz}^{ee}$ but its magnetoelectric and electromagnetic polarizability are not. The free space Green's function includes all the dynamic terms, but it may be approximated by its strongest term when analytic expression have to be derived (see Ref [89] in this Supporting Information)

$$G \approx \frac{e^{ik_0|z_t - z_s|}}{4\pi|z_t - z_s|^3}. \qquad (3.A3)$$

here subscripts “s” and “t” denote sample and tip, respectively. Combining Eqs. (3.B8)-(3.B10) in Ref [89] in this supporting information and noting that the incident azimuthally and radially polarized waves lack transverse components on their axis (the *z* axis), and since both the tip and sample are located along the optical axis, Eqs. (3.A1) and (3.A2) reduce to

$$\begin{bmatrix} E_x^{\mathrm{loc}}(z_\mathrm{t}) \\ E_y^{\mathrm{loc}}(z_\mathrm{t}) \\ E_z^{\mathrm{loc}}(z_\mathrm{t}) \end{bmatrix} = \begin{bmatrix} 0 \\ 0 \\ E_z^{\mathrm{inc}}(z_\mathrm{t}) \end{bmatrix} - \frac{G}{\varepsilon_0} \begin{bmatrix} \alpha_\mathrm{s}^{ee}\left(-\frac{G}{\varepsilon_0}\alpha_\mathrm{t}^{ee}E_x^{\mathrm{loc}}(z_\mathrm{t})\right) \\ \alpha_\mathrm{s}^{ee}\left(-\frac{G}{\varepsilon_0}\alpha_\mathrm{t}^{ee}E_y^{\mathrm{loc}}(z_\mathrm{t})\right) \\ -2\alpha_\mathrm{s}^{ee}\left(E_z^{\mathrm{inc}}(z_\mathrm{s}) + 2\frac{G}{\varepsilon_0}\alpha_\mathrm{t}^{ee}E_z^{\mathrm{loc}}(z_\mathrm{t})\right) - 2\alpha_{\mathrm{s},zz}^{em}H_z^{\mathrm{inc}}(z_\mathrm{s}) \end{bmatrix}, \quad (3.A4)$$

and

$$\begin{bmatrix} H_x^{\mathrm{loc}}(z_\mathrm{t}) \\ H_y^{\mathrm{loc}}(z_\mathrm{t}) \\ H_z^{\mathrm{loc}}(z_\mathrm{t}) \end{bmatrix} = \begin{bmatrix} 0 \\ 0 \\ H_z^{\mathrm{inc}}(z_\mathrm{t}) \end{bmatrix} - \frac{G}{\mu_0} \begin{bmatrix} \alpha_{s,xx}^{me}\left(-\frac{G}{\varepsilon_0}\alpha_\mathrm{t}^{ee}E_x^{\mathrm{loc}}(z_\mathrm{t})\right) \\ \alpha_{s,yy}^{me}\left(-\frac{G}{\varepsilon_0}\alpha_\mathrm{t}^{ee}E_y^{\mathrm{loc}}(z_\mathrm{t})\right) \\ -2\alpha_{\mathrm{s},zz}^{me}\left(E_z^{\mathrm{inc}}(z_\mathrm{s}) + 2\frac{G}{\varepsilon_0}\alpha_\mathrm{t}^{ee}E_z^{\mathrm{loc}}(z_\mathrm{t})\right) - 2\alpha_\mathrm{s}^{mm}H_z^{\mathrm{inc}}(z_\mathrm{s}) \end{bmatrix}, \quad (3.A5)$$

respectively. Analogous equations can be obtained for the local field acting on the sample. Solving Eqs. (3.A4) and (3.A5) for the longitudinal field components (there are 6 equations and 6 unknowns), the transverse *x* and *y* components of the local fields vanish and the longitudinal *z*-component of the electric and magnetic fields read

$$E_z^{\mathrm{loc}}(z_\mathrm{t}) = \frac{1}{1-(2G)^2\frac{\alpha_\mathrm{t}^{ee}}{\varepsilon_0}\frac{\alpha_\mathrm{s}^{ee}}{\varepsilon_0}}\left[\left(1+2G\frac{\alpha_\mathrm{s}^{ee}}{\varepsilon_0}\right)E_z^{\mathrm{inc}}(z_\mathrm{t}) + 2G\frac{\alpha_{\mathrm{s},zz}^{em}}{\varepsilon_0}H_z^{\mathrm{inc}}(z_\mathrm{t})\right], \quad (3.A6)$$

and

$$H_z^{\mathrm{loc}}(z_{\mathrm{t}}) = \left(2G\frac{\alpha_{s,zz}^{me}}{\mu_0} + \frac{\left(1+2G\frac{\alpha_{\mathrm{s}}^{ee}}{\varepsilon_0}\right)(2G)^2}{1-(2G)^2\frac{\alpha_{\mathrm{t}}^{ee}}{\varepsilon_0}\frac{\alpha_{\mathrm{s}}^{ee}}{\varepsilon_0}}\frac{\alpha_{\mathrm{t}}^{ee}}{\varepsilon_0}\frac{\alpha_{\mathrm{s,zz}}^{me}}{\mu_0} \right) E_z^{\mathrm{inc}}(z_{\mathrm{t}}) +$$

$$\left(1+2G\frac{\alpha_{\mathrm{s}}^{mm}}{\mu_0} + \frac{(2G)^3}{1-(2G)^2\frac{\alpha_{\mathrm{t}}^{ee}}{\varepsilon_0}\frac{\alpha_{\mathrm{s}}^{ee}}{\varepsilon_0}}\frac{\alpha_{\mathrm{t}}^{ee}}{\varepsilon_0}\frac{\alpha_{\mathrm{s,zz}}^{me}}{\mu_0}\frac{\alpha_{\mathrm{s,zz}}^{em}}{\varepsilon_0} \right) H_z^{\mathrm{inc}}(z_{\mathrm{t}}), \qquad (3.A7)$$

respectively, where we have neglected the phase difference between the tip and sample since their distance is electrically small and we choose to have slowly varying incident field with *z* compared to the scattered field [107]. Using a similar approach, one may derive the local electric and magnetic fields at the sample location and it is clear that for ARPB excitation, the local electric and magnetic fields at the tip and sample locations lack transverse components.

Appendix B Swing of the optical force for the ARPB excitation

In this section we summarize the steps to obtain an approximate formulation for the swing of the force exerted on the tip in the near field region of a chiral sample for ARPB illumination discussed in Sec. 3.4. Neglecting the effect of magnetic dipole of the tip (compared to its electric dipole effect), the expression for the time-averaged optical force exerted on the achiral tip reads

$$\mathbf{F} = \frac{1}{2}\mathrm{Re}\left[\left(\nabla \mathbf{E}^{\mathrm{loc}}(\mathbf{r}) \right)^{*}_{\mathbf{r}=\mathbf{r}_{\mathrm{t}}} \cdot \mathbf{p}_{\mathrm{t}} \right]. \qquad (3.B1)$$

The gradient operator for vector A, in matrix representation based on Cartesian coordinates is defined as

$$\nabla \mathbf{A} = \begin{bmatrix} \partial_x \mathrm{A}_x & \partial_y \mathrm{A}_x & \partial_z \mathrm{A}_x \\ \partial_x \mathrm{A}_y & \partial_y \mathrm{A}_y & \partial_z \mathrm{A}_y \\ \partial_x \mathrm{A}_z & \partial_y \mathrm{A}_z & \partial_z \mathrm{A}_z \end{bmatrix}. \tag{3.B2}$$

Since local APRB fields possess only *z*-components on the beam axis, the tip dipole has only the *z*-component, and as a consequence the force exerted on the tip possess only the *z*-component, given by

$$F_z = \frac{1}{2}\mathrm{Re}\left[\left(\frac{\partial}{\partial z} E_z^{\mathrm{loc}}(z)\right)^*_{z=z_\mathrm{t}} p_{\mathrm{t},z}\right]. \tag{3.B3}$$

Note that the local field acting on the tip is $E_z^{\mathrm{loc}}(z_\mathrm{t}) \approx E_z^{\mathrm{inc}}(z_\mathrm{t}) + 2p_{\mathrm{s},z}G/\varepsilon_0$ since $\mathbf{E}^{\mathrm{loc}}\left(\mathrm{z_t}\right) = \mathbf{E}^{\mathrm{inc}}\left(\mathrm{z_t}\right) + \mathbf{E}_{\mathrm{scat}}\big|_{\mathrm{s}\to\mathrm{t}}$ and $\mathbf{E}_{\mathrm{scat}}\big|_{\mathrm{s}\to\mathrm{t}} = -G/\varepsilon_0\left[p_{\mathrm{s},x}\hat{\mathbf{x}} + p_{\mathrm{s},y}\hat{\mathbf{y}} - 2p_{\mathrm{s},z}\hat{\mathbf{z}}\right]$. Now assuming that $\mathrm{E}_\mathrm{z}^{inc}$ is slowly varying with *z* compared to the scattered near field acting on the tip generated by the sample, we obtain [107]

$$F_z \approx \frac{1}{2}\mathrm{Re}\left[\left(2p_{\mathrm{s},z}\frac{\partial}{\partial z}\frac{G}{\varepsilon_0}\right)^*_{z=z_\mathrm{t}} p_{\mathrm{t},z}\right]. \tag{3.B4}$$

Next, we need to express both $p_{\mathrm{s},z}$ and $p_{\mathrm{t},z}$ in terms of the incident field. To do that we use $p_{\mathrm{t},z} = \alpha_\mathrm{t}^{ee} E_z^{\mathrm{loc}}(z_\mathrm{t})$, and substitute the local fields $E_z^{\mathrm{loc}}(z_\mathrm{t})$ acting on the tip from Eq. (3.A6). We recall that in this chapter the electric polarizability of the sample is isotropic i.e. $\alpha_{\mathrm{s},xx}^{ee} = \alpha_{\mathrm{s},yy}^{ee} = \alpha_{\mathrm{s},zz}^{ee}$ but its magnetoelectric and electromagnetic polarizability are not. We then substitute $p_{\mathrm{s},z} = \alpha_\mathrm{s}^{ee} E_z^{\mathrm{loc}}(z_\mathrm{s}) + \alpha_{\mathrm{s},zz}^{em} H_z^{\mathrm{loc}}(z_\mathrm{s})$ in (3.B4) where

$$E_z^{\mathrm{loc}}\left(z_{\mathrm{s}}\right)=E_z^{\mathrm{inc}}\left(z_{\mathrm{s}}\right)+\frac{G}{\varepsilon_0}\frac{\alpha_{\mathrm{t}}^{ee}}{1-\left(2G\right)^2\frac{\alpha_{\mathrm{t}}^{ee}}{\varepsilon_0}\frac{\alpha_{\mathrm{s}}^{ee}}{\varepsilon_0}}\left[\left(1+2G\frac{\alpha_{\mathrm{s}}^{ee}}{\varepsilon_0}\right)E_z^{\mathrm{inc}}\left(z_{\mathrm{t}}\right)+2G\frac{\alpha_{\mathrm{s},zz}^{em}}{\varepsilon_0}H_z^{\mathrm{inc}}\left(z_{\mathrm{t}}\right)\right], \quad (3.B5)$$

and

$$H_z^{\mathrm{loc}}\left(z_{\mathrm{s}}\right)=H_z^{\mathrm{inc}}\left(z_{\mathrm{s}}\right)+2G\frac{\alpha_{\mathrm{t}}^{mm}}{\mu_0}\left(\left(2G\frac{\alpha_{\mathrm{s},zz}^{me}}{\mu_0}+\frac{\left(1+2G\frac{\alpha_{\mathrm{s}}^{ee}}{\varepsilon_0}\right)\left(2G\right)^2}{1-\left(2G\right)^2\frac{\alpha_{\mathrm{t}}^{ee}}{\varepsilon_0}\frac{\alpha_{\mathrm{s}}^{ee}}{\varepsilon_0}}\frac{\alpha_{\mathrm{t}}^{ee}}{\varepsilon_0}\frac{\alpha_{\mathrm{s},zz}^{me}}{\mu_0}\right)E_z^{\mathrm{inc}}\left(z_{\mathrm{t}}\right)+\right.$$
$$\left.\left(1+2G\frac{\alpha_{\mathrm{s}}^{mm}}{\mu_0}+\frac{\left(2G\right)^3}{1-\left(2G\right)^2\frac{\alpha_{\mathrm{t}}^{ee}}{\varepsilon_0}\frac{\alpha_{s}^{ee}}{\varepsilon_0}}\frac{\alpha_{\mathrm{t}}^{ee}}{\varepsilon_0}\frac{\alpha_{\mathrm{s},zz}^{me}}{\mu_0}\frac{\alpha_{\mathrm{s},zz}^{em}}{\varepsilon_0}\right)H_z^{\mathrm{inc}}\left(z_{\mathrm{t}}\right)\right), \quad (3.B6)$$

are the local fields acting on the sample. In conclusion, the *z* component of the time-averaged force exerted on the tip is approximated as

$$F_z \approx \frac{1}{2}\mathrm{Re}\left\{\frac{2\alpha_{\mathrm{t}}^{ee}}{1-(2G)^2\frac{\alpha_{\mathrm{t}}^{ee}}{\varepsilon_0}\frac{\alpha_{\mathrm{s}}^{ee}}{\varepsilon_0}}\left[\left(1+2G\frac{\alpha_{\mathrm{s}}^{ee}}{\varepsilon_0}\right)E_z^{\mathrm{inc}}(z_{\mathrm{t}})+2G\frac{\alpha_{\mathrm{s},zz}^{em}}{\varepsilon_0}H_z^{\mathrm{inc}}(z_{\mathrm{t}})\right]\times\right.$$

$$\left[\frac{\alpha_{\mathrm{s}}^{ee}}{1-(2G)^2\frac{\alpha_{\mathrm{t}}^{ee}}{\varepsilon_0}\frac{\alpha_{\mathrm{s}}^{ee}}{\varepsilon_0}}\left[\left(1+2G\frac{\alpha_{\mathrm{t}}^{ee}}{\varepsilon_0}\right)E_z^{\mathrm{inc}}(z_{\mathrm{s}})\right]+\alpha_{\mathrm{s},zz}^{em}\left(H_z^{\mathrm{inc}}(z_{\mathrm{s}})+\ldots\right.\right.$$

$$2G\frac{\alpha_{\mathrm{t}}^{mm}}{\mu_0}\left(\left(2G\frac{\alpha_{\mathrm{s},zz}^{me}}{\mu_0}+\frac{\left(1+2G\frac{\alpha_{\mathrm{s}}^{ee}}{\varepsilon_0}\right)(2G)^2}{1-(2G)^2\frac{\alpha_{\mathrm{t}}^{ee}}{\varepsilon_0}\frac{\alpha_{\mathrm{s}}^{ee}}{\varepsilon_0}}\frac{\alpha_{\mathrm{t}}^{ee}}{\varepsilon_0}\frac{\alpha_{\mathrm{s},zz}^{me}}{\mu_0}\right)E_z^{\mathrm{inc}}(z_{\mathrm{t}})+\ldots\right.$$

$$\left.\left.\left.\left.\left(1+2G\frac{\alpha_{\mathrm{s}}^{mm}}{\mu_0}+\frac{(2G)^3}{1-(2G)^2\frac{\alpha_{\mathrm{t}}^{ee}}{\varepsilon_0}\frac{\alpha_{\mathrm{s}}^{ee}}{\varepsilon_0}}\frac{\alpha_{\mathrm{t}}^{ee}}{\varepsilon_0}\frac{\alpha_{\mathrm{s},zz}^{me}}{\mu_0}\frac{\alpha_{\mathrm{s},zz}^{em}}{\varepsilon_0}\right)H_z^{\mathrm{inc}}(z_{\mathrm{t}})\right)\right)\right]^*\frac{-3}{4\pi\varepsilon_0 d^4}\right\},$$

(3.B7)

where we used $\partial G/\partial z \approx -3/(4\pi d^4)$ with d the distance between the sample and the tip and we have neglected the phase term because of the assumption $k_0 d << 1$. Next, expanding in power series and after neglecting the terms that contain polarizability power of high orders compared to lower orders we approximate Eq. (3.B7) as

$$F_z \approx \frac{1}{2}\mathrm{Re}\left\{\alpha_{\mathrm{t}}^{ee}E_z^{\mathrm{inc}}(z_{\mathrm{t}})\left[\alpha_{\mathrm{s}}^{ee}E_z^{\mathrm{inc}}(z_{\mathrm{s}})+\alpha_{\mathrm{s},zz}^{em}H_z^{\mathrm{inc}}(z_{\mathrm{s}})\right]^*\frac{-3}{2\pi\varepsilon_0 d^4}\right\}. \qquad (3.B8)$$

In the next step, we consider the ARPB incident fields, that on the beam axis (i.e., at $\rho = 0$ since both the tip and sample are placed on the axis of the beam) reduce to

$$E = E_z^{\mathrm{RPB}} = |\mathbf{E}_0| e^{-2i\tan^{-1}(z/z_R)} e^{ik_0 z},$$
$$H_z^{\mathrm{ARPB}} = H_z^{\mathrm{APB}} e^{i\psi} = F_Y \frac{|\mathbf{E}_0|}{\eta_0} e^{-2i\tan^{-1}(z/z_R)} e^{ik_0 z} e^{i\psi}. \tag{3.B9}$$

Note that when $F_Y = 1$, the powers of the APB and RPB illuminations are equal. Next, considering the quasistatic limit by assuming $k_0 d \to 0$ (which means $E_z^{\mathrm{inc}}(z_t) \approx E_z^{\mathrm{inc}}(z_s)$), and assuming that the sample is located at $z_s = 0$ we obtain

$$F_z \approx \frac{1}{2}\mathrm{Re}\left[\left(\frac{\alpha_s^{ee}}{\varepsilon_0} + F_Y \frac{\alpha_{s,zz}^{em}}{\sqrt{\varepsilon_0\mu_0}} e^{i\psi}\right)^* \frac{-3}{2\pi d^4} |\mathbf{E}_0|^2 \alpha_t^{ee}\right]. \tag{3.B10}$$

Therefore, the force difference between two cases with any two phase parameters ψ_1 and ψ_2 reads

$$F_z^{ARPB}|_{\psi_2} - F_z^{ARPB}|_{\psi_1} \approx -\frac{3F_Y |\mathbf{E}_0|^2}{4\pi\sqrt{\varepsilon_0\mu_0} d^4}\left[\mathrm{Re}\left(e^{-i\psi_2}\alpha_t^{ee}\alpha_{s,zz}^{em\,*}\right) - \mathrm{Re}\left(e^{-i\psi_1}\alpha_t^{ee}\alpha_{s,zz}^{em\,*}\right)\right], \tag{3.B11}$$

Now, we prove that the maximum force difference for any two phase parameters ψ_1 and ψ_2 occurs when $F_Y^2 = |V/(\eta_0 I)|^2 = 1$, i.e., when the illumination powers of the APB and RPB (with the same waist parameter) are equal. To this end, we assume the amplitude coefficient of the RPB, defined in Sec. 3.4, to be *I* and the amplitude coefficient of APB, defined in Sec. 3.4, to be $V = F_Y I/\eta_0$. According to Eq. (3.10) and (3.13), the total ARPB power reads

$$P_{\mathrm{tot}} = F_Y^2 \frac{|I|^2}{2}\eta_0\left(1 - \frac{1}{2(\pi w_0/\lambda)^2}\right) + \frac{|I|^2}{2}\eta_0\left(1 - \frac{1}{2(\pi w_0/\lambda)^2}\right). \tag{3.B12}$$

(we recall that $|\mathbf{E}_0| = 4|I|/\left(\sqrt{\pi} w^2 \omega \varepsilon_0\right)$). Under the above assumption the force difference between two measurements for ARPB illuminations with two different phase parameters ψ_1 and ψ_2 in Eq. (3.B11) reads

$$\Delta F = -\frac{12 F_Y \eta_0 |I|^2}{\pi^2 w_0^4 \omega^2 \sqrt{\varepsilon_0 \mu_0}\, d^4 \varepsilon_0^2}\left[\mathrm{Re}\left(e^{-i\psi_2}\alpha_{\mathrm{t}}^{ee}\alpha_{\mathrm{s},zz}^{em\,*}\right) - \mathrm{Re}\left(e^{-i\psi_1}\alpha_{\mathrm{t}}^{ee}\alpha_{\mathrm{s},zz}^{em\,*}\right)\right]. \tag{3.B13}$$

where

$$|I|^2 = \frac{1}{\left(1+F_Y^2\right)}\frac{2P_{\mathrm{tot}}}{\left(1-\dfrac{1}{2\left(\pi w_0/\lambda\right)^2}\right)}, \tag{3.B14}$$

from Eq. (3.B12). To find the value of F_Y for which ΔF peaks, assuming a constant P_{tot}, we replace $|I|^2$ from Eq. (3.B14) into Eq. (3.B13) and set the derivative of Eq. (3.B13) with respect to F_Y equal to zero and get

$$\frac{1}{F_Y^2+1} - \frac{2F_Y^2}{\left(F_Y^2+1\right)^2} = 0. \tag{3.B15}$$

For this equation to hold, we require to have $F_Y = 1$.

Let us now investigate the maximum force difference for any arbitrary F_Y, i.e., the swing as defined in Eq. (3.15). To this end, we expand Eq. (3.B13) as

$$\Delta F = -\frac{12F_Y\eta_0|I|^2}{\pi^2 w_0^4\omega^2\sqrt{\varepsilon_0\mu_0}d^4\varepsilon_0^2}\left[(\cos\psi_2-\cos\psi_1)\,\mathrm{Re}\left(\alpha_{\mathrm{t}}^{ee}\alpha_{\mathrm{s},zz}^{em\,*}\right)+(\sin\psi_2-\sin\psi_1)\,\mathrm{Im}\left(\alpha_{\mathrm{t}}^{ee}\alpha_{\mathrm{s},zz}^{em\,*}\right)\right].$$

(3.B16)

As it is observed from this equation, since $\alpha_{\mathrm{t}}^{ee}\alpha_{\mathrm{s},zz}^{em\,*}$ has a complex value for a general lossy particle, then, it is not straightforward to conclude that the swing happens when $|\psi_2-\psi_1|\approx 180^\circ$. However, as we have shown in the Sec. 3.4 (see e.g. Figure 3.5(b)) our numerical analyses demonstrate such a conclusion and we analytically prove it here for special case of particles with negligible losses.

Assuming tip and sample to have negligible losses (under this assumption α_{s}^{em} is purely imaginary) Eq. (3.B16) reduces to

$$\Delta F \approx -\frac{3F_Y|\mathbf{E}_0|^2}{4\pi\sqrt{\varepsilon_0\mu_0}d^4}\,\mathrm{Re}\left(\alpha_{\mathrm{t}}^{ee}\right)\mathrm{Im}\left(\alpha_{\mathrm{s},zz}^{em\,*}\right)(\sin\psi_2-\sin\psi_1). \qquad (3.B17)$$

Since $|\sin\psi|<1$, then, the maximum value of Eq. (3.B17) occurs when $|\psi_2-\psi_1|=180^\circ$ which results in $|\sin\psi_2-\sin\psi_1|=2$. Therefore, the maximum swing force, i.e., the difference between the maximum and minimum of F_z exerted force on the tip, defined in Eq. (3.15), is obtained from Eq. (3.B17) when $F_Y=1$ and is given as Eq. (3.18).

It is important to note that in deriving Eq. (3.B17) we have assumed two lossless nanoparticles have a small (subwavelength) distance, i.e., $k_0 d\to 0$, however, both the tip and the sample have finite dimensions and these assumptions may not necessarily hold. This approximation is used here to lead to a very simple formula that shows what the main features to

characterize the force on the tip are. When these approximation do not hold, the minimum and maximum of the force exerted on the tip does not happen for the phase parameter sets of $\psi_1 = 90^\circ$ and $\psi_2 = 270^\circ$ (or $\psi_1 = 270^\circ$ and $\psi_2 = 90^\circ$) as it is expected from Eq. (3.B17). For example, in Figure 3.4(b), where we used the exact force formula (Eq. (2.3)) with the full dynamic Green's function and proper losses, the approximations here described would not lead to an accurate result, and indeed the minimum and maximum of the force on the tip occur for phase parameter sets of $\psi_1 = 165^\circ$ and $\psi_2 = 345^\circ$ as shown in Figure 3.4(b) (or $\psi_1 = 345^\circ$ and $\psi_2 = 165^\circ$). The important thing to be noted is that in order to reach the maximum swing force in the two experiments what is obvious is not the absolute values of the phase parameters in the two sets of experiments but the difference between them which should be $|\psi_2 - \psi_1| = 180^\circ$. Anyway, the absolute values of desired phase parameters are not known prior to calculations, and in order to specify them one requires to examine for all values of phase parameters and to plot a curve as is given in Figure 3.4(b). In an experiment the phase difference ψ should be scanned for each of the two measurements in order to find the maximum swing.

Appendix C. A discussion on bianisotropy of particles

The electric and magnetic dipole moments of a polarizable particle are given by Eq. (2.1). In general, dipolar particles have electric and/or magnetic properties given by the polarizabilities . $\underline{\boldsymbol{\alpha}}^{ee}$ and $\underline{\boldsymbol{\alpha}}^{mm}$, however dipolar particles can also have bianisotropic properties represented by the polarizability terms $\underline{\boldsymbol{\alpha}}^{em}$ and $\underline{\boldsymbol{\alpha}}^{me}$. All bianisotropic particles may be classified into four types, i.e., chiral, omega, Tellegen, and "moving". While the first two (chiral and omega) lie into the category of reciprocal particles, the last two types (Tellegen, and "moving") are nonreciprocal. For

reciprocal particles the magnetoelectric and electromagnetic polarizability tensors reduce to a single one since $\underline{\boldsymbol{\alpha}}^{me} = -\left(\underline{\boldsymbol{\alpha}}^{em}\right)^{T}$ whereas the electric and magnetic polarizability tensors are related as $\underline{\boldsymbol{\alpha}}^{ee} = \left(\underline{\boldsymbol{\alpha}}^{ee}\right)^{T}$ and $\underline{\boldsymbol{\alpha}}^{mm} = \left(\underline{\boldsymbol{\alpha}}^{mm}\right)^{T}$, where T is the tensor transpose. The magnetoelectric polarizability tensor of a particle in the Cartesian coordinates reads

$$\underline{\boldsymbol{\alpha}}^{em} = \begin{bmatrix} \alpha_{xx}^{em} & \alpha_{xy}^{em} & \alpha_{xz}^{em} \\ \alpha_{yx}^{em} & \alpha_{yy}^{em} & \alpha_{yz}^{em} \\ \alpha_{zx}^{em} & \alpha_{zy}^{em} & \alpha_{zz}^{em} \end{bmatrix}. \tag{3.C1}$$

The particle is called chiral (pseudo-chiral) if at least one of the diagonal components is nonzero. Moreover, nonzero off-diagonal components imply omega type bianisotropic particles.

CHAPTER 4 : DISCRIMINATING CHIRALITY FROM ANISOTROPY USING FORCE PHOTO-INDUCED BY AZIMUTHALLY-RADIALLY POLARIZED BEAM

Sec. 4.1 Motivation

As was discussed in Chapters 2 and Chapter 3, spectroscopic techniques based on circular dichroism (CD), optical rotation (OR) and Raman optical activity (ROA) have been introduced and studied to detect and characterize chiral samples [108]–[110]. However, these methods encounter major challenges due to the very weak interaction of light with chiral nanoparticles. To overcome this deficiency, we introduced the theory of using PiFM to unravel the structure of chiral nanosamples and determine the type of enantiomer. However, as was demonstrated in previous studies and also will be shown in this chapter, when circularly polarized beams are used, this method can't differentiate between chiral sample and anisotropic achiral sample [41]. In other words, PiFM detects anisotropic achiral samples as chiral.

Here, by taking advantage of the combination of vortex beams, azimuthally polarized beam (APB) and radially polarized beam (RPB), we demonstrate how to differentiate chiral sample from anisotropic achiral sample.

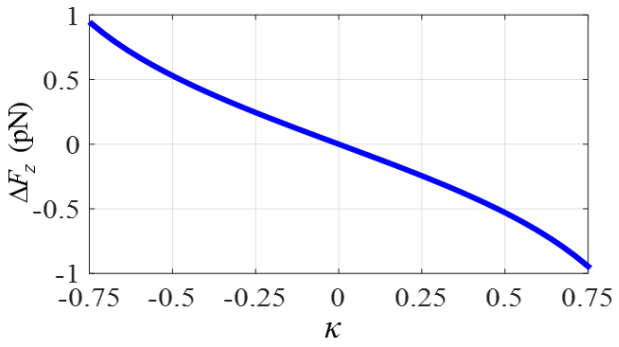

FIG. 4-1. Exerted differential force on the tip-apex for isotropic sample with chirality parameter κ and permittivity $\varepsilon_s = 2.4$. Note that for, $\kappa = 0$ differential force is zero.

Sec. 4.2 Deficiency of CP beam in differentiating chirality from anisotropy

We first show the deficiency of circularly polarized waves in distinguishing chiral from anisotropic particles. In analogy to what shown in [111], we consider an example when the sample and tip are illuminated with circularly polarized Gaussian beam propagating along the positive *z*-direction with 1mW power at wavelength $\lambda = 400$ nm. We assume the waist parameter of the Gaussian beam [89] to be $w_0 = 0.7\lambda$ and the sample is placed at the beam waist. The chiral material is described by the chirality parameter κ (which describes the degree of handedness of a material, see Eq. (A1) of Ref. [89]) that here varies from –0.75 to 0.75. Both the sample and the tip are considered to be nanospheres with equal radii $a_s = a_t = 50$ nm and the gap between them is $g = 10$ nm. (In experiments gaps may be even smaller than that [112] leading to stronger field gradients, but here we do not investigate that since this study is based on dipolar approximation.) Furthermore, without loss of generality, the relative permittivity of the sample is assumed to be $\varepsilon_s = 2.4$ (in this case the sample is isotropic) and its electromagnetic and magnetoelectric polarizability expressions α^{em} and α^{me} are calculated as in Eq. (A2)-(A10) of Ref. [113]. The tip is assumed to be made of silver with relative permittivity $\varepsilon_t = -3.6 + i0.19$ as in [111]. In Fig. 4-1 we have depicted the differential force on the tip defined as $\Delta F = F_z^{\mathrm{RCP}} - F_z^{\mathrm{LCP}}$ versus chirality parameter of the sample (Note that F_z^{RCP} and F_z^{LCP} are the force exerted on the tip for RCP and LCP illuminations respectively). As it can be seen, the exerted differential force on the tip for an achiral sample ($\kappa = 0$) is zero, however, as the magnitude of the chirality parameter of the sample

grows, the differential force exerted on the tip grows as well. Moreover, for samples with $\kappa > 0$, the differential force is positive while for samples with $\kappa < 0$ the differential force is negative which verifies the capability of this method in enantiomer detection of chiral samples. Indeed, it has been shown in [89] that differential force is linearly dependent on both the chiral response of the sample and the electric response of the tip and is inversely related to the quartic power of probe-sample distance. Note that even if we used the complete formula (3) the sample and tip have negligible magnetic polarizabilities (calculated via Mie theory) and $\mathbf{m}_t$ is negligible.

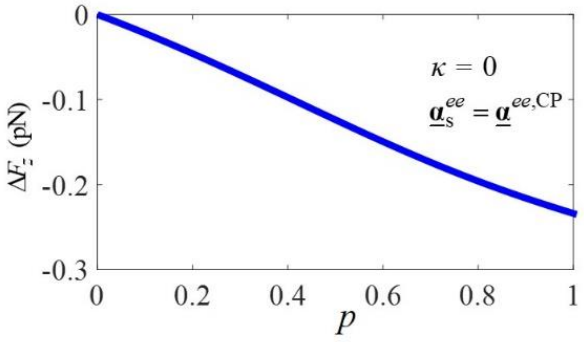

FIG. 4-2. Exerted differential force on the tip-apex for anisotropic achiral sample with $\underline{\boldsymbol{\alpha}}_s^{ee} = \underline{\boldsymbol{\alpha}}^{ee,\mathrm{CP}}$. Note that as c increases, the sample becomes more anisotropic. Based on LCP and RCP illuminations. The differential force is zero only for *p*=0 (isotropic case), and different from zero for the anisotropic case showing that LCP and RCP may give ambiguous results about chirality.

Now we turn our attention to a case of an anisotropic achiral sample. We keep all the parameters for the beam, tip and sample as in Fig. 4-1 except that in this case we assume that the particle is achiral i.e. $\kappa = 0$. Moreover, we consider the electric polarizability of the sample as

$$\underline{\boldsymbol{\alpha}}_s^{ee} = \underline{\boldsymbol{\alpha}}^{ee,\mathrm{CP}} = 5^p \alpha_0^{ee} \hat{\mathbf{x}}\hat{\mathbf{x}} + 3^p \alpha_0^{ee} \hat{\mathbf{y}}\hat{\mathbf{y}} + \alpha_0^{ee} \hat{\mathbf{z}}\hat{\mathbf{z}} \tag{4.1}$$

For *p*=0, the sample is isotropic and as p increases, the sample becomes more anisotropic. In Fig. 4-2 the differential force, still based on LCP and RCP illuminations., is demonstrated for

values of p between 0 and 1. As it is shown, for an isotropic sample (p=0), the differential force is zero. However, as the anisotropy of the sample increases, so does the differential force. This example clearly exhibits the inability of circular polarization in distinguishing chirality from anisotropy which calls for utilizing alternative types of beam illuminations to characterize chirality of samples.

Sec. 4.3 Using ARPB to differentiate chirality and anisotropy

As was mentioned earlier in this chapter, we show how to solve this problem using the ARPB. To demonstrate the ability of an ARPB in detecting chirality, we assume that the illuminating ARPB has 2 mW power at $\lambda = 400$ nm, and $V/(\eta_0 I) = 1$, in which $\eta_0 = \sqrt{\mu_0 / \varepsilon_0}$ is the free space wave impedance [111], [114], [115]. Therefore, each beam carries 1 mW. We place the tip and sample with permittivity, radii and gap given in the example of Fig. 4-1 along the axis of the ARPB, on which the transverse components of the electric and magnetic fields are vanishing whereas the longitudinal components are not.

We also assume the sample to be at the focus of the beams, i.e., at the beam waist, due to higher intensity of the fields. Furthermore, we consider the beam parameter of both RPB and APB (which are forming the ARPB) to be $w_0 = 0.7\lambda$ and chirality parameter of the sample to be constant $\kappa = 0.5$. As suggested in [111], in order to detect chirality, we vary the phase parameter ψ in and measure the time-average exerted force on the tip. As it is clearly exhibited in Fig 4-3 (a), with this illumination, by sweeping the phase parameter, the exerted force on the tip varies for a chiral particle. Next, we reveal the most important ability of an ARPB beam, differentiating a chiral sample from an anisotropic one. To that end, we assume illumination, tip and sample to remain

the same as in Fig.4-3 (a) except the sample that is now achiral and the electric polarizability of the sample is given by Eq. (4.1) when p=1 i.e. $\underline{\boldsymbol{\alpha}}^{ee,\mathrm{ARPB}} = 5\alpha_0^{ee}\hat{\mathbf{x}}\hat{\mathbf{x}} + 3\alpha_0^{ee}\hat{\mathbf{y}}\hat{\mathbf{y}} + \alpha_0^{ee}\hat{\mathbf{z}}\hat{\mathbf{z}}$.

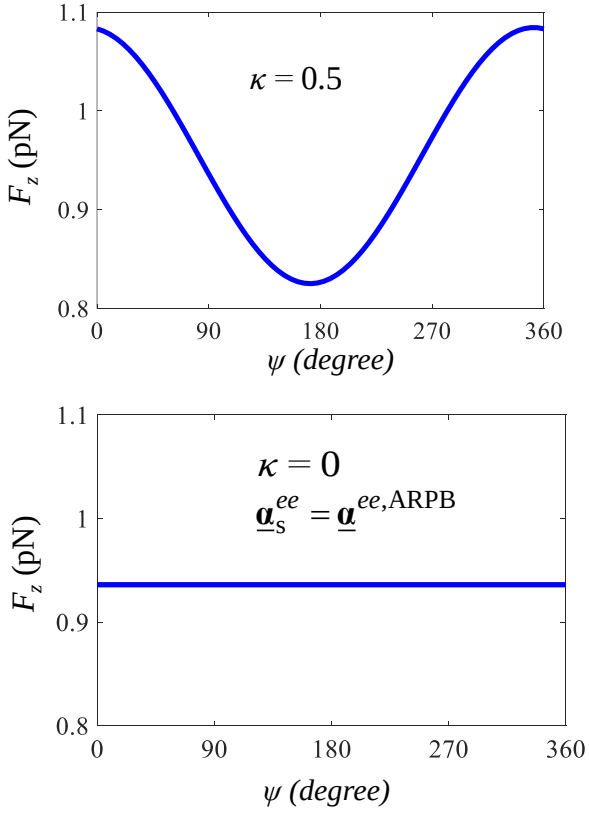

FIG. 4-3. Force exerted on the tip-apex in the z-direction when using a combination of phase-shifted APB and ARB for (a) isotropic chiral sample with $\kappa = 0.5$ and $\varepsilon_s = 2.4$, and (b) anisotropic achiral sample with $\kappa = 0$ and electric polarizability $\underline{\boldsymbol{\alpha}}^{ee} = \underline{\boldsymbol{\alpha}}_{\mathrm{S}}^{ee,\mathrm{ARPB}}$. These results demonstrate the possibility of distinguishing chirality from anisotropy by utilizing an APRB with sweeping phase parameter ψ.

The exerted force on the tip versus phase parameter ψ is depicted in Fig. 4-3 (b). As the figure demonstrates, under ARPB illumination, by varying the phase parameter ψ the exerted

force on the tip remains constant and thus, the ARPB successfully distinguishes between chiral and anisotropic sample.

Fig. 4-4 summarizes the main results of the chapter in a concise flowchart. Based on this flowchart, we first consider LCP and RCP beams as illuminations. If the differential force is zero, then the sample is an anisotropic achiral one. If not, we use the ARPB illumination and measure the force exerted on the tip by varying the phase parameter. If the force stays constant by varying the phase parameter ψ, the sample is anisotropic achiral whereas if the exerted force varies, the sample is chiral. The first step with CP could also be eliminated and the investigation could be carried out by using only the APRB with sweeping phase parameter. In all these examples we are not considering chiral anisotropy whose effect is considered negligible compared to anisotropy in the electric polarizability.

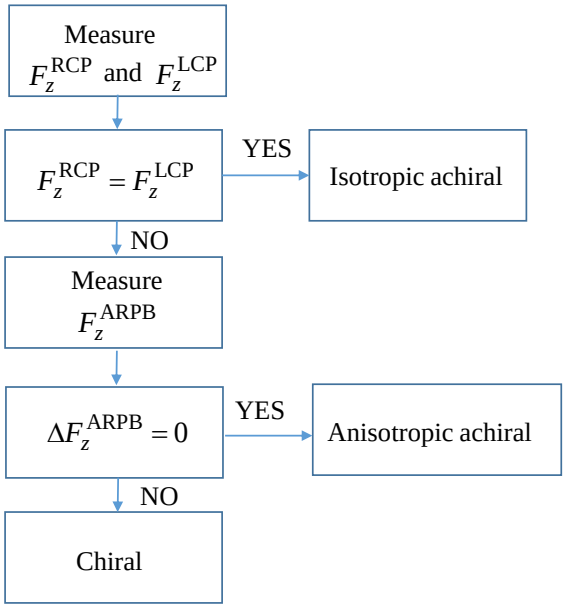

FIG. 4-4. Summary of the proposed method to differentiate between anisotropic and chiral sample. If the differential force under CP illumination is not zero, ARPB should be used to distinguish chirality from anisotropy.

Sec. 4.4 Conclusion

In conclusion in this chapter, based on the concept of photoinduced optical force, we have presented a method to discriminate a chiral particle from an anisotropic one. We have proposed to use an ARPB which is a combination of an APB and a RPB with a controlled proper phase shift ψ. Although the individual APB and RPB are not chiral beams (and thus cannot reveal the chirality of a sample) their combination is chiral and their chirality depends on their phase difference ψ. We have demonstrated that as the phase parameter ψ of ARPB varies, the exerted force on the tip varies as well. However, for an anisotropic achiral sample varying that phase does not change the exerted force on the tip, hence the ARPB can distinguish between chirality and anisotropy whereas circular polarization cannot.

CHAPTER 5 : MANIPULATION AND SORTING OF CHIRAL PARTICLES USING STRUTURED NANOSCALE LIGHT

Sec. 5.1 Motivation

Tremendous progress in understanding light-matter interaction has brought up techniques involving optical force as promising tools for a wide variety of applications including trapping and manipulating of nanoparticles [20], [116]. Recently there has been a great deal of interest in employing optical forces rather than chemical methods for detection and separation of chiral particles since light is less invasive [30], [32], [89], [99], [111], [117]–[120]. The main idea behind sorting chiral molecules using optical forces is the discriminatory behavior of chiral light for chiral molecules with different handedness which leads to their mechanical separation. For example in Ref. [30] by placing the chiral sample over a substrate and illuminating the system with a plane wave, lateral optical force is used to sort the enantiomers. In similar studies, the lateral optical force associated with recoil mechanical force has been employed to sort enantiomers[27], [121]. Circularly polarized beams or plane waves, which are chiral light, have been employed largely to interact with chiral particles.

The idea of using the superposition of an azimuthally polarized beam (APB) and a radially polarized beam (RPB) to discriminate between chiral and achiral particles has first been demonstrated and studied in detail in Ref. [111]. Such a superposition of two beams with orthogonal field components, which we called ARPB in our previous work [111], is used for detecting and unscrambling the structure of chiral nanoparticles using photo-induced force microscopy. It has been shown that, by sweeping the phase difference between the APB and RPB

and measuring the swing of the longitudinal force exerted on a plasmonic particle in the vicinity of the sample, the chirality of the sample can be identified. Indeed, the APRB was introduced to identify the longitudinal rather than transversal chirality of samples which seemed to be impossible with CP beams. The ARPB has been also used in [122], [123] to generate "optimal" chiral fields and in [102] for exciting a chiral dipole moment in an achiral silicon nanoparticle. In this chapter, we theoretically demonstrate the manipulation and sorting of chiral nanoparticles and enantiomers by using a plasmonic nanoparticle excited by an ARPB. We illustrate how to push and pull chiral particles and sort enantiomers by changing the phase difference of two ARPBs as the excitation beams.

Sec. 5.2 ARPB on the axis

Before delving into the analysis and results, we briefly summarize the properties of the APRB. The superposed APB and RPB, with a phase difference of ψ forms the ARPB as

$$\begin{aligned}\mathbf{E}^{\mathrm{ARPB}} &= \mathbf{E}^{\mathrm{APB}} + \mathbf{E}^{\mathrm{RPB}} e^{i\psi}, \\ \mathbf{H}^{\mathrm{ARPB}} &= \mathbf{H}^{\mathrm{APB}} + \mathbf{H}^{\mathrm{RPB}} e^{i\psi},\end{aligned} \tag{5.1}$$

where $\mathbf{E}^{\mathrm{APB}}$, $\mathbf{H}^{\mathrm{APB}}$, $\mathbf{E}^{\mathrm{RPB}}$, and $\mathbf{H}^{\mathrm{RPB}}$ are the electric and magnetic field vectors of the APB and RPB, respectively. Full expressions for these vector fields are given in Ref. [111]. The field expressions for the ARPB illuminating beam at the beam axis are given as (note that both the plasmonic particle and chiral sample are placed on the beam axis, and the chiral sample is at z = 0 where the minimum waist occurs)

$$\mathbf{H}^{\mathrm{ARPB}}\Big|_{\rho=0} = -\frac{V}{\sqrt{\pi}} \frac{4i}{w^2 \omega \mu_0} \mathrm{e}^{-2i\tan^{-1}\left(z/z_{\mathrm{R}}\right)} \mathrm{e}^{ik_0 z} \hat{\mathbf{z}}, \tag{5.2}$$

$$\mathbf{E}^{\mathrm{ARPB}}\Big|_{\rho=0} = -\frac{I}{\sqrt{\pi}} \frac{4i}{w^2 \omega \varepsilon_0} e^{-2i\tan^{-1}\left(z/z_R\right)} e^{i\psi} e^{ik_0 z} \hat{\mathbf{z}} \tag{5.3}$$

in which V and I are the amplitude coefficients and ε_0 and μ_0 are the vacuum permittivity and permeability respectively. Furthermore $z_R = \pi w_0^2 / \lambda$ is the Rayleigh range and $w = w_0\sqrt{1+(z/z_R)^2}$, where w0 is the beam parameter and controls the spatial extent of the beam in the transverse plane, i.e., the beam half waist (w0 tends to be the same as half of the beam waist for non-sharply collimated beams) [124] . The expression of the power carried by an ARPB is given in [111]. We show in Fig. 5-1 (a) the magnitude of the electric field components of a representative ARPB, i.e., E_x^{ARPB}, E_y^{ARPB}, and E_z^{ARPB} for two different phase parameters, $\psi = 0$ and $\psi = 90°$, where we have also assumed that $V/(\eta_0 I) = 1$, in which $\eta_0 = \sqrt{\mu_0/\varepsilon_0}$ is the free space wave impedance. This condition implies that $E_z^{\text{ARPB}} = e^{i\psi}\eta_0 H_z^{\text{ARPB}}$ and for $\psi = \pm\pi/2$ the field is said to be "optimally chiral" [122], [123]

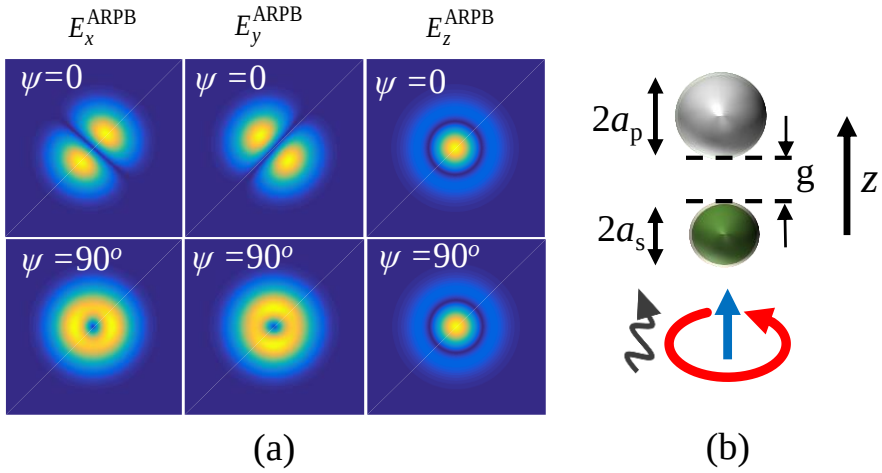

Figure 5-1 Magnitude of the electric field components of the superposition of an APB and an RPB, for two phase parameters $\psi = 0$ and $\psi = 90^o$. On the axis, i. e., at x=y=0 , only the z- components of the fields are non-vanishing,. b) Schematic of a chiral sample (green sphere) in the vicinity of a plasmonic particle under ARPB illumination.

As it is observed in Fig. 5-1 (a), for $\psi = 0$ the magnitude of the transverse electric field components (i.e., the x- and y-components) has a dumbbell-shape whereas for $\psi = 90°$ it has a donut-shape. In both cases, along the beam axis (i.e., along the z-direction), the transverse components of the fields vanish.

Sec. 5.3 Setup for sorting enantiomers

The APB and RPB beams have coincident vortex axes (here the *z*-axis) and beam half-waist parameter $w_0 = 0.7\lambda$, and we assume each beam carrying 1 mW of power at $\lambda = 400\,\text{nm}$. Both the sample and the plasmonic particle are considered to have equal radii $a_\text{s} = a_\text{p} = 50$ nm with a gap of $g = 10$ nm (see Fig. 5-1 (a)). Furthermore, without loss of generality and for the proof of concept, the relative permittivity of the sample is assumed to be $\varepsilon_\text{s} = 2.4$ whereas that of the plasmonic particle is assumed to be $\varepsilon_\text{p} = -3.6 + \text{i}0.19$ (this is the relative permittivity of silver at the operational wavelength [24]). The chirality parameter of the sample (which describes the degree of handedness of a material, (see Eq. (A1) of Ref. [20]) is assumed as $\kappa = 0.75$. First, we assume that the ARPB is propagating in the –*z* direction as is depicted in Fig. 5-2(a). In Fig. 5-2 (b), we have depicted the *z*-component of the exerted force on the chiral particle versus phase parameter ψ of the ARPB. The exerted force depends on the phase parameter ψ of the ARPB. Interestingly the chiral sample can either be pulled toward (positive force) or pushed in the direction of beam propagation depending on the selection of the phase parameter ψ. Indeed, light usually results in a repelling force on objects due to radiation pressure. The possibility of realizing nontrivial optical pulling forces has been recently studied in Refs. [25–28] using several methods such as tractor beams, the superposition of several plane waves, etc. As we alternatively proposed

here by placing the chiral sample in the near-field of a plasmonic particle and tuning the phase parameter of the ARPB, the chiral sample can be pulled or pushed toward the illuminating beam. In Fig. 5-2(c) and (d) we have depicted the geometry of the system with illumination from below and the exerted force on the chiral sample respectively. An analogous behavior is observed.

We want to quantify the physical properties that determine the force on the chiral sample, in terms of electric and magnetoelectric polarizabilities of the plasmonic particle and sample, respectively. We provide a simple formula for the *z*-component of the force by neglecting the probe magnetic polarizability. In free space, the time averaged optical force on the chiral sample under ARPB illumination from below, with phase parameter ψ, reads

$$F_z \approx \frac{1}{2}\mathrm{Re}\left[\left(\frac{\alpha_{\mathrm{s}}^{ee}}{\varepsilon_0}+\frac{\alpha_{\mathrm{s}}^{em}}{\sqrt{\varepsilon_0\mu_0}}e^{i\psi}\right)\frac{-3}{2\pi d^4}|\mathbf{E}_0|^2\left(\alpha_{\mathrm{p}}^{ee}\right)^*\right] \tag{5.4}$$

in which d is the center-to-center distance between the chiral sample and the plasmonic particle where $|\mathbf{E}_0| = 4|I|/\left(\sqrt{\pi}w^2\omega\varepsilon_0\right)$ is the amplitude of the electric field of ARPB at the origin. Equation (5.4) clearly demonstrates that the force depends linearly on the electric polarizability α_{p}^{ee} of the plasmonic particle, hence, the material, size and shape of the plasmonic particle play crucial roles in determining the force. More importantly, Eq. (5.4) illustrates that the force is also related to the magnetoelectric polarizability α_{s}^{em} of the sample. Furthermore, it is also worth noting that F_z is inversely related to the quartic power of the plasmonic particle-sample distance. It is important to note that in deriving the analytic expression in Eq. (5.4) we have assumed that the two lossless particles have a small (subwavelength) distance, i.e., $k_0 d \to 0$, however, both the plasmonic particle and the chiral sample have finite dimensions. This approximation is used here

just to lead to a very simple formula that shows what the main features to characterize the force on the plasmonic particle are.

Sec. 5.4 Counter-propagating waves for comprehensive control of chiral particles

So far, we have demonstrated the ability of ARPB to relatively control the direction and the amplitude of the exerted force on a chiral sample near a plasmonic particle by changing the phase parameter ψ. However, a complete control over the chiral particle is achieved when we control the direction of its motion. In order to do that, we propose using two counter-propagating ARPBs. Under such an illumination, we fix the phase parameter of one ARPB (for example the one illuminating from above) and vary the phase parameter of the other ARPB in order to push or pull the chiral sample toward the plasmonic particle. To make it clearer, in Fig. 5-3 (a), we have demonstrated such an arrangement where two ARPBs are illuminating the system. The phase parameter of the beam propagating in –*z* direction (we call it beam 2) is called ψ_2 whereas the phase parameter of the beam illuminating from below (we call it beam 1) is called ψ_1. We fix the phase parameter $\psi_2 = 42^o$, therefore, based on the results of Fig. 5-2, the force that is applied on the chiral particle due to beam 2 is =0.15 pN (plus sign for force means force in the +*z* direction). In Fig. 5-3 (b) we have illustrated the exerted force on the sample by varying phase parameter of beam 1. As one can observe, by changing the phase parameter of beam 1, the sample is either attracted to or retracted from the plasmonic particle.

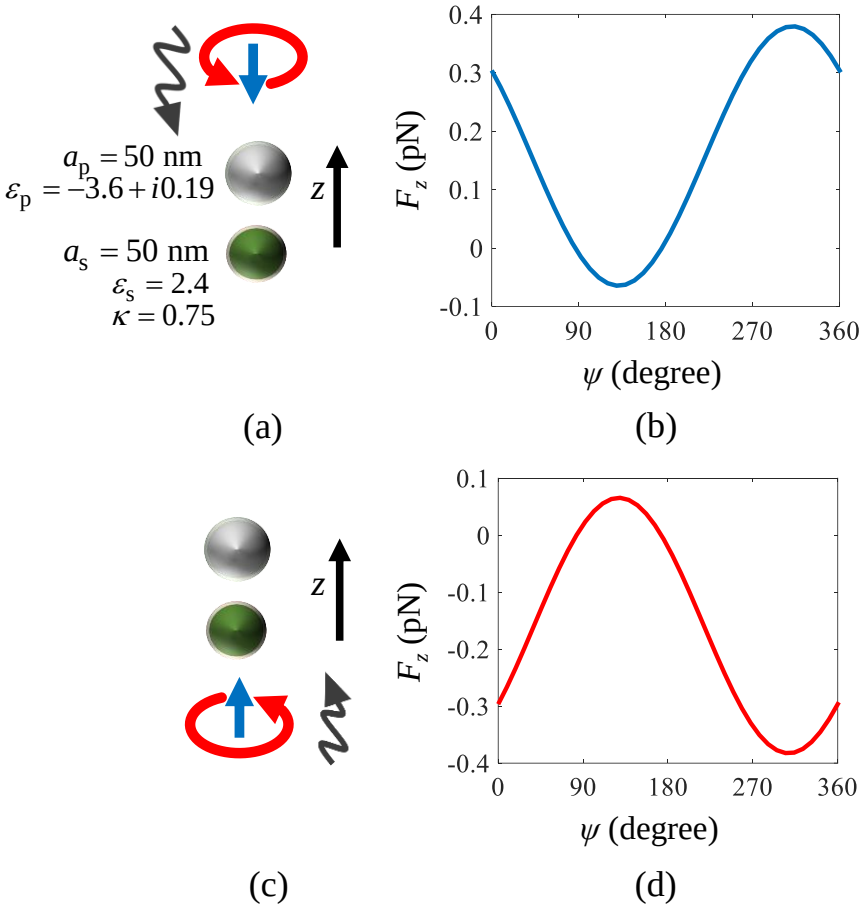

Fig 5-2. (a) and (c) Schematic of ARPB illumination from above and below respectively of the chiral sample (green nanoparticle). (b) and (d) Force exerted on the sample in the z-direction when using ARPB illumination, for two cases of illumination from above and illumination from below, respectively. This figure clearly shows the ability of ARPB illumination to control the force, and its sign, on the chiral particle by varying the phase parameter ψ .

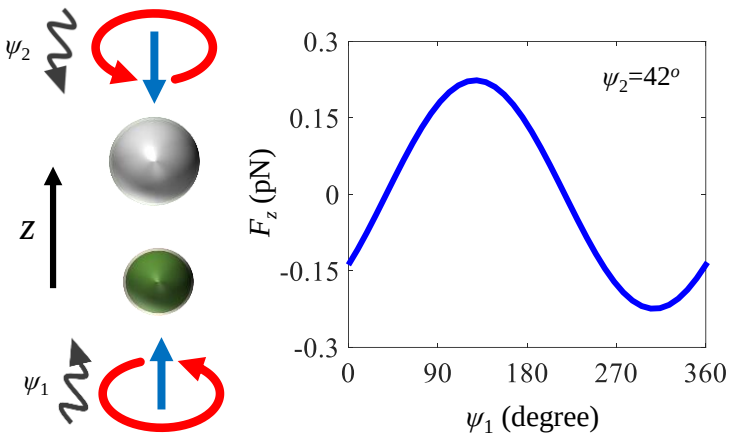

Fig 5-3. (a) Schematic of two counter-propagating ARPB illuminations and the chiral sample (green nanosphere). The field interaction is maximized thanks to the nearfield of plasmonic nanoparticle that acts as a nanoantenna. (b) Exerted force on the chiral sample for $\psi_2 = 42^o$ varying ψ_1. The chiral sample can be attracted to or repelled from the plasmonic nanoparticle by changing the phase parameter of beam ψ_1.

Next, we reveal the important ability of the proposed illumination to manipulate enantiomers. To that end, we assume the system of Fig. 5-3 where the plasmonic particle and sample are illuminated by two counter-propagating ARPB beams with $\psi_2 = 42^o$ while we vary ψ_1 and study in Fig. 5-4 the exerted force on two samples, i.e., enantiomers with opposite chirality parameters $\kappa = 0.75$ and $\kappa = -0.75$. As it is shown in Fig. 5-4, the exerted forces on the enantiomers are equal in amplitude and opposite in sign, therefore, for any arbitrary ψ_1 one enantiomer is attracted to the plasmonic particle while the other enantiomer (chirality of opposite sign) retracts. Hence, the combination of these counter-propagating waves can be used to sort and separate chiral molecules or enantiomers. Note that for this configuration the best separation occurs for $\psi_1 \approx \psi_2 \pm 90^o$.

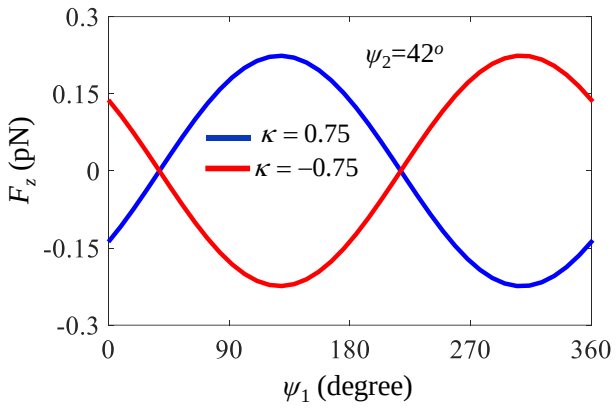

Fig 5-4. Exerted force on the sample under two counter-propagating ARPB beams (As in Fig. 5-3) with $\psi_2 = 42^o$ varying ψ_1 for two different cases of $\kappa = 0.75$ and $\kappa = -0.75$. This figure illustrates that we can separate enantiomers with two-counter-propagating ARPBs.

In conclusion, we have demonstrated the possibility of controlling, pushing and pulling chiral nanoparticles using a structured light beam made of a combination of an azimuthally and a radially polarized beam, which can drag or push a chiral particle toward a plasmonics nanoantenna. Furthermore we have shown that two of these APRB beams with proper phase difference are used to push or repel chiral particles. A possible realization of this scheme could be for chiral particles in solution. By using a plasmonic probe and illuminating with two counter-propagating ARPBs from right and left, one can guide one type of the enantiomers to the left (right) side while the opposite enantiomers are repelled and move to the opposite side.

Compared to previously reported beams to control chiral particles and sort enantiomers which are based on lateral force and on either plane or circularly polarized waves, this chapter demonstrates another possibility using an engineered combination of chiral beams made of a proper combination of azimuthally and radially polarized beams with proper phase difference.

CHAPTER 6 : GIANT FIELD ENHANCEMENT IN LONGITUDINAL EPSILON NEAR ZERO FILMS

Sec. 6.1 Introduction and Background

Recently in [130], the basis of electric levitation of a dipole in vicinity of an epsilon near zero (ENZ) metamaterial was demonstrated. Thus, in this chapter, we present a new class of ENZ materials, called LENZ for potential future applications in manipulation and characterization of chiral particles.

Realization of ENZ behavior has been achieved using multilayer stack of metal and dielectric[131], 3-D periodic array of dielectric-core metallic-shell nanospheres with fluorescent dyes in the core of each nanoparticle for the loss-compensation[132] or employing metal-coated waveguides at their cut-off frequency[133], [134]. Owing to their extremely large velocity of phase propagation[135], such materials enable linear applications such as tailoring radiation emission[136]–[140], energy squeezing and supercoupling[141]. On the other hand ENZ materials can be utilized to achieve huge field enhancement. In[142] the field intensity enhancement (FIE) of a isotropic ENZ semi-infinite medium and a isotropic ENZ slab under TM (transverse magnetic) plane wave incidence are theoretically investigated. Exploiting this ability, optical nonlinearities such as second or third harmonic generation[143]–[148] and Kerr nonlinearities[149] have been enhanced significantly.

In this chapter, we establish that under TM wave incidence a uniaxially anisotropic epsilon near zero film exhibits remarkably stronger FIE than isotropic epsilon near zero. Hereafter, we will use IENZ for isotropic epsilon near zero studied in[142] for comparison. The film whose surfaces are normal to the z axis, shown in Fig. 6-1, is marked by the subscript '2', and modeled via a relative permittivity tensor $\underline{\boldsymbol{\varepsilon}}_2 = \varepsilon_t \left(\hat{\mathbf{x}}\hat{\mathbf{x}} + \hat{\mathbf{y}}\hat{\mathbf{y}} \right) + \varepsilon_z \hat{\mathbf{z}}\hat{\mathbf{z}}$. Particularly we show that the specific type of anisotropy useful for super-field enhancement occurs when the *zz* entry of the permittivity tensor is near zero, which in the following we call it longitudinal epsilon near zero (LENZ) condition. Most interestingly, we show that FIE in LENZ films occurs for a very wide range of angles of incidence and is almost independent of the film thickness unlike IENZ films where such features occur for a fix angle and extremely thin films [142]. To the best of our knowledge, significant field enhancement can't be achieved using realistic ENZ materials due to inherent material losses. Remarkably, in this chapter, we introduce a LENZ structure that provides large field enhancement despite having realistic loss which paves the way for a wide range of applications associated to second harmonic generation and enhanced field emission. Indeed, through reciprocity, we demonstrate that a z-polarized dipole located in the LENZ film has stronger far field radiation compared to the IENZ case.

Sec. 6.2 Analysis and Results

The geometry of the investigated problem is depicted in Fig. 6-1. We first investigate the FIE in a film with thickness d under a TM plane wave as in Fig. 6-1(a), and then we investigate the radiative emission enhancement of a point dipole inside a LENZ film as illustrated in Fig. 6-1(b).

The electric field vector of the incident TM wave is in the $x-z$ plane, i.e., $\mathbf{E}_1^i = E_1^i\left(\cos\theta\hat{\mathbf{x}} + \sin\theta\hat{\mathbf{z}}\right)e^{i\mathbf{k}_1\cdot\mathbf{r}}$ in which $\mathbf{k}_1$ is the wavevector of the impinging TM wave where $k_1 = |\mathbf{k}_1| = \omega\sqrt{\mu_0\varepsilon_0\varepsilon_1}$ is the wavenumber in medium 1. A monochromatic, time harmonic convention $e^{-i\omega t}$ is implicitly assumed. The transverse (to the z axis) wavenumber is k_t whereas the longitudinal wavenumber outside the film is $k_{z1} = \sqrt{k_1^2 - k_t^2}$. In the LENZ film the entries of the relative permittivity tensor are $\varepsilon_t = \varepsilon_t' + i\varepsilon_t''$ and $\varepsilon_z = \varepsilon_z' + i\varepsilon_z''$. We will use $k_{z2} = \sqrt{\varepsilon_t k_0^2 - \left(\varepsilon_t / \varepsilon_z\right)k_t^2}$ to denote the longitudinal wavenumber in the film [150], [151]. Owing to the continuity of the normal displacement field component at $z = d/2$,

$$\varepsilon_1 E_{z1}\big|_{z=(d/2)^+} = \varepsilon_z\, E_{z2}\big|_{z=(d/2)^-} \ , \tag{6.1}$$

in which E_{z1} and E_{z2} are the longitudinal components of the total electric field in media 1 and 2 respectively. By replacing the value of E_{z1} in the abovementioned equation one obtains [142]

$$\varepsilon_1 E_1^i(1-\Gamma)\sin\theta = \varepsilon_z E_{z2} \ , \tag{6.2}$$

in which Γ is the plane wave reflection coefficient at $z = d/2$, seen from the upper interface and is given by

$$\Gamma\left(d,\theta\right) = \frac{-i\left(k_{z2}^2 - k_{z1}^2\hat{\varepsilon}_t^2\right)s_h}{2k_{z1}k_{z2}\hat{\varepsilon}_t\, c_h - i\left(k_{z2}^2 + k_{z1}^2\hat{\varepsilon}_t^2\right)s_h} \ , \tag{6.3}$$

with $s_h = \sin(k_{z2}d)$, $c_h = \cos(k_{z2}d)$ and $\hat{\varepsilon}_t = \varepsilon_t / \varepsilon_1$. Assuming $\hat{\varepsilon}_z = \varepsilon_z / \varepsilon_1$, it is convenient to define the local z-polarized field intensity enhancement at $z = (d/2)^-$ as

$$\text{FIE} = \left| \frac{E_{z2}}{E_1} \right|^2 = \left| \frac{(1-\Gamma)\sin\theta}{\hat{\varepsilon}_z} \right|^2 , \tag{6.4}$$

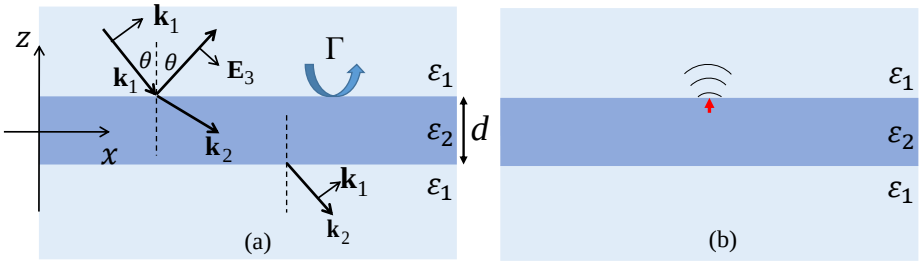

Figure 6-1 Schematic of longitudinal epsilon near zero film (a) under TM-plane wave incidence and (b) with dipole located below the interface.

which is the ratio of the electric field in the longitudinal direction in the film to the incident electric field amplitude at the same place in the absence of the film. In the following, unless stated otherwise, FIE is always calculated just below the top surface of the film at $z = (d/2)^-$. The field intensity enhancement depends strongly on the choice of ε_z, i.e., by choosing ε_z close to zero FIE gets large. FIE is also strongly dependent upon the reflection coefficient Γ, which in general is complex, and if it gets close to unity then FIE vanishes. We will compare the LENZ and IENZ cases for their field enhancement and radiation enhancement capabilities using examples and analytical calculations.

As an example, in Fig. 6-2, we consider a film with thickness $d = \lambda/3$, with $\lambda = 2\pi/k_1$, made of LENZ material surrounded by vacuum i.e. $\varepsilon_1 = 1$. In Fig. 6-2(a) we assume that the film

has longitudinal permittivity of $\varepsilon_z = 0.001 + i0.001$ and transverse permittivity of $\varepsilon_t = \varepsilon_t' + i0.001$ at wavelength λ. We report the FIE at $z = (d/2)^-$, i.e. just below the top surface of the film, versus the real part of the transverse permittivity of the film ε_t' and the angle of incidence of the impinging TM-polarized wave. The IENZ case, as a subset of LENZ cases reported in Fig. 6-2 (a), is marked with white dashed line where $\varepsilon_t' = \varepsilon_z'$. Notably, we observe that FIE is the lowest for the IENZ case compared to LENZ cases with larger ε_t'. As the anisotropy of the film becomes starker, the FIE increases significantly, in other words, it is better not to have vanishing ε_t'. Importantly, the plot shows that LENZ leads to not only larger FIE, but also to a wider angular span of large FIE, contrarily to the IENZ case that provides large FIE only on a very limited angular range[142]. We now exactly show the reason of the physical behavior that differentiates the LENZ from the IENZ: assuming $\varepsilon_1 = 1$ we substitute Γ from (3) in (4):

$$\mathrm{FIE} = \left| \frac{2k_{z1}\varepsilon_t \left(k_{z2}c_h - ik_{z1}\varepsilon_t s_h \right)}{\varepsilon_z \left[2k_{z1}k_{z2}\varepsilon_t c_h - i\left(k_{z2}^2 + k_{z1}^2\varepsilon_t^2 \right) s_h \right]} \sin\theta \right|^2 . \tag{6.5}$$

From this equation one may observe that for isotropic film with permittivity $\varepsilon_2 \to 0$ and $\theta \neq 0$ equation (6.5) is rewritten as

$$\mathrm{FIE}_{\mathrm{IENZ}} = \left| \frac{-2\cos\theta\cos\left(-ik_1 d\sin\theta\right)}{\sin\left(-ik_1 d\sin\theta\right)} \right|^2 , \tag{6.6}$$

which is a finite (i.e., not large) value unless θ or d tends to zero. Note that for an assigned arbitrary θ, $\mathrm{FIE}_{\mathrm{IENZ}}$ does not tend to infinity even if we assume that $\varepsilon_2 \to 0$. It is worth

mentioning that $\mathrm{FIE}_{\mathrm{IENZ}}$ in thin ENZ films (i.e., when $d \to 0$) is inversely proportional to the thickness *d*. This can be seen by simplifying equation (6.6) for $d \to 0$ and using $\cos\left(-ik_1 d \sin\theta\right) \approx 1$ and $\sin\left(-ik_1 d \sin\theta\right) \approx -ik_1 d \sin\theta$, leading to

$$\mathrm{FIE}_{\mathrm{IENZ}} \approx \left| \frac{2\cos\theta}{ik_1 d \sin\theta} \right|^2 . \tag{6.7}$$

Instead, for the LENZ case, assuming near zero values for ε_z and angles such that $\varepsilon_z << \sin^2\theta$ (because the proper limit should be taken for $\left(\varepsilon_z / \sin^2\theta\right) \to 0$), by simplifying the numerator and denominator of (5), considering finite values of ε_t and d, we obtain

$$\mathrm{FIE}_{\mathrm{LENZ}} \approx \left| \frac{2\sqrt{\varepsilon_t}}{\sqrt{\varepsilon_z}} \cos\theta \right|^2 \approx 4\left|\frac{\varepsilon_t}{\varepsilon_z}\right| \cos^2\theta . \tag{6.8}$$

Here the denominator goes to zero as $\varepsilon_z \to 0$ which causes the FIE to tend towards infinity for the LENZ case. Note that to obtain giant FIE is not necessary to illuminate with small incidence angle θ, whereas in the IENZ case only for small θ, one can get giant FIE. The results of FIE are shown in Fig. 6-2 (b) where FIE is reported in logarithmic scale versus real part of the transverse and longitudinal permittivities for slab with $d = \lambda/3$ and $\varepsilon_t'' = \varepsilon_z'' = 0.001$ under $\theta = 40^o$ incidence angle. Note that as ε_z tends to zero the FIE value increases. Most importantly, as the film becomes more anisotropic (larger $\left|\varepsilon_t'\right|$) FIE increases as well, as was explained with (8). To trace the physical origin of this point, we observe that for a constant near zero value of ε_z and constant incident angle ($\theta = 40^o$ in this example) FIE only depends on $\left|1-\Gamma\right|$. Therefore, the behavior of FIE is a signature of the behavior of the reflection coefficient Γ which tends to one

for IENZ unless when d tends to zero. However, for LENZ case, Γ does not tend to one, paving the way for obtaining large FIE over a wide range of angles.

One of the most important factors in determining the FIE in LENZ and IENZ films is the loss represented by the imaginary part of the permittivity. Note that to evaluate (6) we have assumed that $\varepsilon_2 \to 0$, however in practical cases one can only choose $\varepsilon_2' \to 0$ and hence $\varepsilon_2 = i\varepsilon_2''$ is the minimum value, that can't be arbitrarily small because of losses, further limiting the FIE growth. For LENZ, ideally FIE tends to infinity when $\varepsilon_z \to 0$, and having large ε_t is even more favorable for obtaining large FIE, an important aspect not shown in the literature. The presence of losses implies that one can only choose $\varepsilon_z' \to 0$, hence $\varepsilon_z = i\varepsilon_z''$ can't be arbitrarily small, but from (8) a large FIE in LENZ is still obtained when choosing $\left|\varepsilon_t / \varepsilon_z''\right|$ to be large, indicating that loss effects are overcome in LENZ. This is a striking result showing that limitations are imposed only by having composite materials with large ε_t.

To investigate the effect of the loss, in Fig. 6-3(a) we reproduce the same set of cases as in Fig. 6-2(a) but with higher film loss modeled by $\varepsilon_t'' = \varepsilon_z'' = 0.01$ reporting that FIE decreases drastically due to the loss. However, LENZ still yields higher FIE compared to IENZ (marked with dashed white line). To better appreciate FIE superiority of LENZ over IENZ in a wide angular range both in low and high loss cases, in Fig. 6-3(b) FIE is plotted versus incident angle for IENZ with $\varepsilon_2' = 0.001$ and LENZ with $\varepsilon_t' = 2.5$ and $\varepsilon_z' = 0.001$. For the high loss cases we assume $\varepsilon_2'' = 0.05$ for IENZ and $\varepsilon_t'' = \varepsilon_z'' = 0.05$ for LENZ; for the low loss cases we have $\varepsilon_2'' = 0.01$ for IENZ and $\varepsilon_t'' = \varepsilon_z'' = 0.01$ for LENZ. The outstanding performance of LENZ is demonstrated in this figure by noting that high loss LENZ provides much higher FIE than even low loss IENZ for

angles of incidence $\theta > 10^{o}$. With similar imaginary part of permittivity, the FIE of LENZ is two orders of magnitude higher than that for IENZ for a very wide range of angles of incidence. Moreover, the angular range at which FIE occurs is much wider in the LENZ case than in the IENZ case. Using angular full width at half maximum (FWHM) of FIE defined as the range of angles in which FIE is higher than the half of its maximum value, the angular FWHM of FIE in the low-loss LENZ case is at least 45˚ whereas for the low-loss isotropic case is less than 12˚.

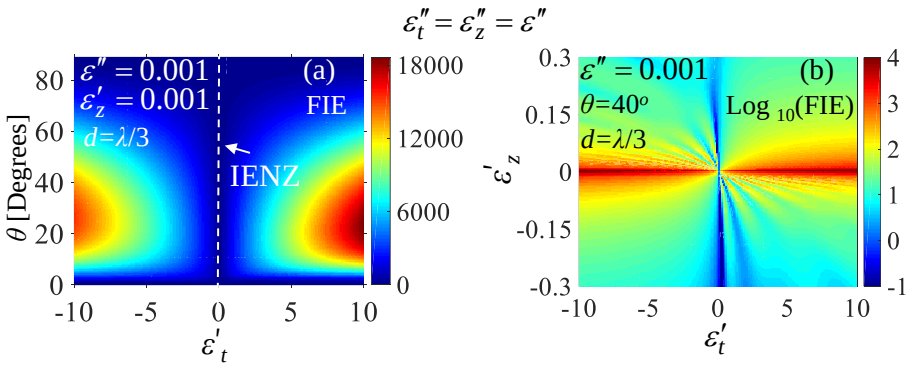

FIG. 6-2. (a) FIE in LENZ film at $z = (d/2)^{-}$ in the geometry of Fig. 6-1 with $d = \lambda/3$ and $\varepsilon_z = 0.001 + i0.001$ and $\varepsilon_t = \varepsilon_t' + i0.001$ as a function of ε_t' and θ. (b) FIE in logarithmic scale versus ε_t' and ε_z'.

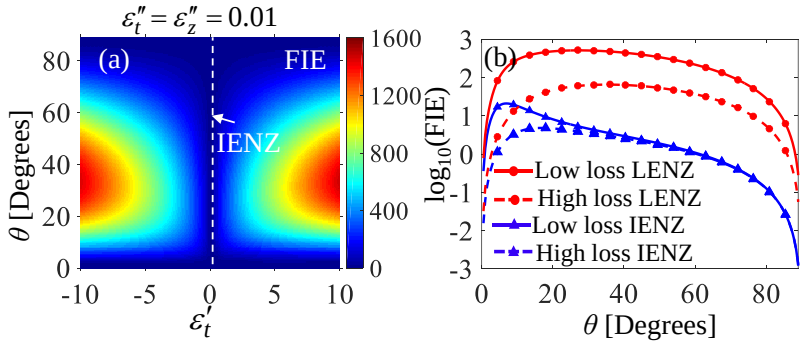

FIG. 6-3. (a) FIE in LENZ film at $z = (d/2)^{-}$ as in Fig. 6-2(a) with higher loss $\varepsilon_t'' = \varepsilon_z'' = 0.01$. (b) Comparison between IENZ and LENZ for different losses.

Another important quality of FIE in LENZ is its high value over a range of *z*-locations within the film. This is reported in Fig. 6-4(a) as a function of z and d, both normalized to wavelength, for a specific case of $\theta = 40^{o}$, $\varepsilon_z = 0.001 + i0.035$ and $\varepsilon_t = 2.5 + i0.035$. The FIE is maximum at the interface between the film and air and decreases by getting deeper into the film. For small thicknesses, when $d < 0.1\lambda$, the FIE has a more uniform distribution inside the film and the FIE at the interface is at similar levels as in thicker films, so thickness is not important to have large FIE near the interface, contrarily to the IENZ case[142]. In Fig. 6-4(b) the dependence of FIE on the film thickness ($d/\lambda = 1$, $d/\lambda = 0.1$ and $d/\lambda = 0.01$) is shown as a function of ε_t' assuming incidence at $\theta = 40^{o}$, $\varepsilon_z = 0.001 + i0.035$ and $\varepsilon_t'' = 0.035$. The exceptional property of a LENZ film with large $|\varepsilon_t|$ to significantly enhance the field independent of its thickness is clearly shown, in contrast to IENZ films where FIE is large only for extremely thin films. This property is simply understood from equation (6.8) in which numerator is proportional to ε_t. Importantly, from Fig. 6-4 (b) we also observe that very thin films (e.g., $d/\lambda = 0.01$) can provide high FIE almost independently of $|\varepsilon_t|$.

We now discuss the results of a realistic LENZ case obtained with a multilayer structure and compare it to IENZ. The multilayer structure providing LENZ performance when homogenized is made of 10 alternate layers, of equal thickness $\lambda/60$, of Dysprosium-doped cadmium oxide (CdO:Dy) [152] with carrier density $n = 3.7 \times 10^{20}$ cm-3, and silicon with permittivity taken from[153]. Using effective medium approximation (EMA)[151], LENZ condition for the homogenized structure occurs at λ_0= 1867.9 nm for which $\varepsilon_z = i0.26$ and $\varepsilon_t = 5.98 + i0.065$. In Fig. 6-5 we calculate the FIE of this structure just below the top surface of

the top layer (CdO:Dy) via transfer-matrix method (TMM) and compare it with FIE of bulk CdO:Dy at its ENZ wavelength of λ_0= 1866.7 nm with $\varepsilon_2 = i0.13$ (note that $\varepsilon_z'' = 2\varepsilon_2''$). Also, to better appreciate the remarkable effect of LENZ, we have provided the FIE of indium tin oxide (ITO) at its ENZ frequency[146]. Films have thicknesses $d = \lambda / 3$, where the wavelength is the one at the respective LENZ and ENZ conditions . As it can be seen, not only FIE for the multilayer (LENZ) is higher for all angles of incidence than bulk CdO:Dy but also the maximum of the former is 12 folds the maximum of the latter. The FIE of ITO is even less than the FIE of CdO:Dy due to its higher loss indicating how FIE in ENZ is in general not practical unless you can use ε_t' as in LENZ to overcome the loss.

Giant *z*-polarized E-field enhancement inside the film for a wide range of angles of incidence in LENZ also implies, via the reciprocity theorem that a *z*-polarized dipole located at the E-field hotspot in a LENZ film radiates very strong far-fields over a wide angular region. Hence, we show next the capability of LENZ films to enhance a dipole radiation emission. This is described by resorting to the key parameter [154]

$$\mathrm{REE} = P_{\mathrm{rad}} / P_{\mathrm{fs}} \ , \tag{6.9}$$

where REE is the radiative emission enhancement, P_{rad} is the power radiated in both top and bottom vacuum half-spaces by an impressed dipole located inside the film and P_{fs} is the total power emitted by the same dipole in free space. P_{rad} does not account for all the power emitted by that dipole

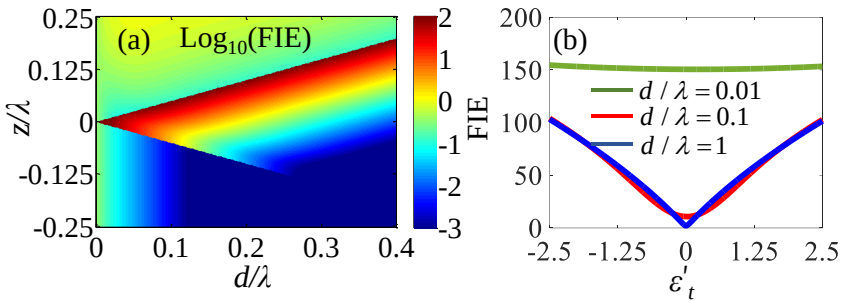

FIG. 6-4. FIE in LENZ for $\theta = 40^{o}$, $\varepsilon_t'' = \varepsilon_z'' = 0.035$ and $\varepsilon_z' = 0.001$ (a) in the film profile for $\varepsilon_t' = 2.5$ (b) as a function of ε_t' for various thicknesses.

which is also dissipated as loss in the LENZ film. In Fig. 6-6, REE of a z-polarized dipole inside the LENZ film with thickness $d = \lambda / 3$ at an infinitesimal distance from the top surface is plotted versus ε_t' and ε_z' for (a) lossless case and (b) when $\varepsilon_t'' = \varepsilon_z'' = 0.01$. We observe that regardless of the sign of ε_z', as long as it is small, REE is large. Moreover, REE increases as $|\varepsilon_t'|$ increases. In the lossless case, the REE is maximized when $\varepsilon_t' < 0$ and $\varepsilon_z' > 0$ or when $\varepsilon_t' > 0$ and $\varepsilon_z' < 0$, however when losses are introduced, this behavior is less pronounced.

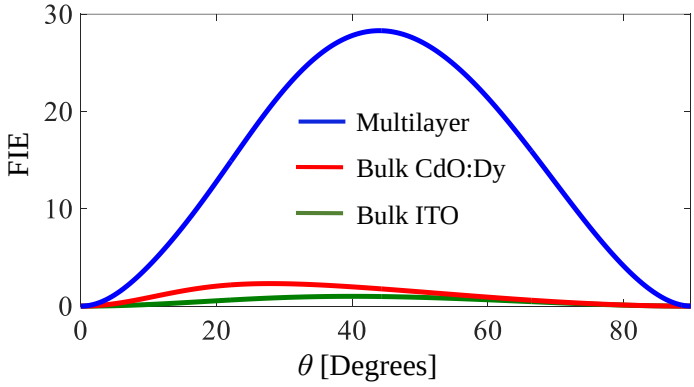

FIG. 6-5. FIE versus angle of incidence for the realistic LENZ (multilayer) and two IENZ cases: bulk CdO:Dy and bulk ITO.

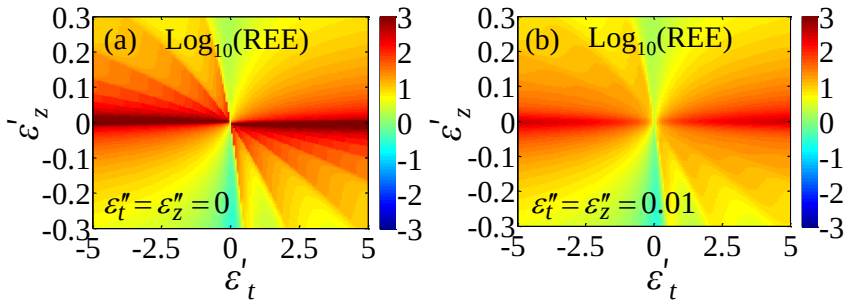

FIG. 6-6. Radiative emission enhancement, versus ε_t' and ε_z' (a) for the lossless case (the color legend is saturated for values more than 1000) and (b) for a lossy case.

Sec. 6.3 Conclusion

In conclusion, we demonstrated the unique ability of LENZ films to generate electric field enhancement and why it is superior to what can be obtained with IENZ. We showed that for the same level of loss, LENZ gives much higher FIE than IENZ and also occurs for a wider range of angles of incidence compared to the IENZ. Furthermore, FIE is almost independent of the thickness of the film unlike the IENZ case where the film has to be extremely thin. Remarkably, losses play a major role in practical IENZ cases for generating FIE but loss effect is instead overcome in LENZ by increasing $|\varepsilon_t|$. Finally, radiative emission in LENZ is higher than in IENZ films and it occurs over a wide angular region with possible applications also in light generation [155].

REFERENCES

[1] D. B. Ambilino, *Chirality at the Nanoscale: Nanoparticles, Surfaces, Materials and More*. Germany: Wiley-VCH, 2009.

[2] J. Behr, *The Lock-and-Key Principle*. U.K.: John Wiley & Sons, 1994.

[3] L. D. Barron and A. D. Buckingham, "Rayleigh and Raman scattering from optically active molecules," *Mol. Phys.*, vol. 20, no. 6, pp. 1111–1119, Jan. 1971.

[4] W. Hug and H. Surbeck, "Vibrational raman optical activity spectra recorded in perpendicular polarization," *Chem. Phys. Lett.*, vol. 60, no. 2, pp. 186–192, Jan. 1979.

[5] L. D. Barron, "Raman Optical Activity," in *Optical Activity and Chiral Discrimination*, S. F. Mason, Ed. Springer Netherlands, 1979, pp. 219–262.

[6] L. D. Barron, E. W. Blanch, and L. Hecht, "Unfolded proteins studied by raman optical activity," *Adv. Protein Chem.*, vol. 62, pp. 51–90, Jan. 2002.

[7] W. C. Johnson, "Protein secondary structure and circular dichroism: A practical guide," *Proteins Struct. Funct. Bioinforma.*, vol. 7, no. 3, pp. 205–214, Jan. 1990.

[8] S. M. Kelly, T. J. Jess, and N. C. Price, "How to study proteins by circular dichroism," *Biochim. Biophys. Acta BBA - Proteins Proteomics*, vol. 1751, no. 2, pp. 119–139, Aug. 2005.

[9] N. J. Greenfield, "Using circular dichroism spectra to estimate protein secondary structure," *Nat. Protoc.*, vol. 1, no. 6, pp. 2876–2890, Jan. 2007.

[10] R. Tullius et al., "'Superchiral' Spectroscopy: Detection of Protein Higher Order Hierarchical Structure with Chiral Plasmonic Nanostructures," *J. Am. Chem. Soc.*, vol. 137, no. 26, pp. 8380–8383, Jul. 2015.

[11] Y. Zhao, A. N. Askarpour, L. Sun, J. Shi, X. Li, and A. Alù, "Chirality detection of enantiomers using twisted optical metamaterials," *Nat. Commun.*, vol. 8, p. 14180, Jan. 2017.

[12] T. B. Freedman, X. Cao, R. K. Dukor, and L. A. Nafie, "Absolute configuration determination of chiral molecules in the solution state using vibrational circular dichroism," *Chirality*, vol. 15, no. 9, pp. 743–758, Jan. 2003.

[13] L. D. Barron, "An Introduction to Chirality at the Nanoscale," in *Chirality at the Nanoscale*, D. B. Amabilino, Ed. Wiley-VCH Verlag GmbH & Co. KGaA, 2009, pp. 1–27.

[14] A. m. Stalcup, “Chiral Separations,” *Annu. Rev. Anal. Chem.*, vol. 3, no. 1, pp. 341–363, Jun. 2010.

[15] A. Ashkin, J. M. Dziedzic, J. E. Bjorkholm, and S. Chu, “Observation of a single-beam gradient force optical trap for dielectric particles,” *Opt. Lett.*, vol. 11, no. 5, p. 288, May 1986.

[16] A. Ashkin, “Optical trapping and manipulation of neutral particles using lasers,” *Proc. Natl. Acad. Sci.*, vol. 94, no. 10, pp. 4853–4860, May 1997.

[17] A. Ashkin, “History of optical trapping and manipulation of small-neutral particle, atoms, and molecules,” *IEEE J. Sel. Top. Quantum Electron.*, vol. 6, no. 6, pp. 841–856, Nov. 2000.

[18] A. Jannasch, A. F. Demirörs, P. D. J. van Oostrum, A. van Blaaderen, and E. Schäffer, “Nanonewton optical force trap employing anti-reflection coated, high-refractive-index titania microspheres,” *Nat. Photonics*, vol. 6, no. 7, pp. 469–473, Jul. 2012.

[19] A. Ashkin and J. M. Dziedzic, “Optical trapping and manipulation of viruses and bacteria,” *Science*, vol. 235, no. 4795, pp. 1517–1520, Mar. 1987.

[20] M. Dienerowitz, M. Mazilu, and K. Dholakia, “Optical manipulation of nanoparticles: a review,” *J. Nanophotonics*, vol. 2, no. 1, pp. 021875-021875–32, 2008.

[21] M. Padgett and R. Bowman, “Tweezers with a twist,” *Nat. Photonics*, vol. 5, no. 6, pp. 343–348, Jun. 2011.

[22] T. W. Hänsch and A. L. Schawlow, “Cooling of gases by laser radiation,” *Opt. Commun.*, vol. 13, no. 1, pp. 68–69, Jan. 1975.

[23] D. Kleckner and D. Bouwmeester, “Sub-kelvin optical cooling of a micromechanical resonator,” *Nature*, vol. 444, no. 7115, pp. 75–78, Nov. 2006.

[24] R. W. Peterson *et al.*, “Laser Cooling of a Micromechanical Membrane to the Quantum Backaction Limit,” *Phys. Rev. Lett.*, vol. 116, no. 6, p. 063601, Feb. 2016.

[25] F. Huang, V. Ananth Tamma, Z. Mardy, J. Burdett, and H. Kumar Wickramasinghe, “Imaging Nanoscale Electromagnetic Near-Field Distributions Using Optical Forces,” *Sci. Rep.*, vol. 5, p. 10610, Jun. 2015.

[26] M. G. Donato *et al.*, “Polarization-dependent optomechanics mediated by chiral microresonators,” *Nat. Commun.*, vol. 5, p. 3656, Apr. 2014.

[27] A. Canaguier-Durand, J. A. Hutchison, C. Genet, and T. W. Ebbesen, “Mechanical separation of chiral dipoles by chiral light,” *New J. Phys.*, vol. 15, no. 12, p. 123037, 2013.

[28] K. Ding, J. Ng, L. Zhou, and C. T. Chan, “Realization of optical pulling forces using chirality,” *Phys. Rev. A*, vol. 89, no. 6, p. 063825, Jun. 2014.

[29] R. P. Cameron, S. M. Barnett, and A. M. Yao, “Discriminatory optical force for chiral molecules,” *New J. Phys.*, vol. 16, no. 1, p. 013020, 2014.

[30] S. B. Wang and C. T. Chan, “Lateral optical force on chiral particles near a surface,” *Nat. Commun.*, vol. 5, p. 3307, Mar. 2014.

[31] G. Tkachenko and E. Brasselet, “Optofluidic sorting of material chirality by chiral light,” *Nat. Commun.*, vol. 5, p. 3577, Apr. 2014.

[32] Y. Zhao, A. A. E. Saleh, and J. A. Dionne, “Enantioselective Optical Trapping of Chiral Nanoparticles with Plasmonic Tweezers,” *ACS Photonics*, vol. 3, no. 3, pp. 304–309, Mar. 2016.

[33] G. Binnig, C. F. Quate, and Ch. Gerber, “Atomic Force Microscope,” *Phys. Rev. Lett.*, vol. 56, no. 9, pp. 930–933, Mar. 1986.

[34] I. Rajapaksa, K. Uenal, and H. K. Wickramasinghe, “Image force microscopy of molecular resonance: A microscope principle,” *Appl. Phys. Lett.*, vol. 97, no. 7, p. 073121, Aug. 2010.

[35] I. Rajapaksa and H. K. Wickramasinghe, “Raman spectroscopy and microscopy based on mechanical force detection,” *Appl. Phys. Lett.*, vol. 99, no. 16, p. 161103, Oct. 2011.

[36] D. Nowak *et al.*, “Nanoscale chemical imaging by photoinduced force microscopy,” *Sci. Adv.*, vol. 2, no. 3, p. e1501571, Mar. 2016.

[37] J. Jahng *et al.*, “Gradient and scattering forces in photoinduced force microscopy,” *Phys. Rev. B*, vol. 90, no. 15, p. 155417, Oct. 2014.

[38] J. Jahng *et al.*, “Linear and Nonlinear Optical Spectroscopy at the Nanoscale with Photoinduced Force Microscopy,” *Acc. Chem. Res.*, vol. 48, no. 10, pp. 2671–2679, Oct. 2015.

[39] E. U. Condon, “Theories of Optical Rotatory Power,” *Rev. Mod. Phys.*, vol. 9, no. 4, pp. 432–457, Oct. 1937.

[40] A. Ishimaru, S.-W. Lee, Y. Kuga, and V. Jandhyala, “Generalized constitutive relations for metamaterials based on the quasi-static Lorentz theory,” *IEEE Trans. Antennas Propag.*, vol. 51, no. 10, pp. 2550–2557, Oct. 2003.

[41] A. Serdyukov, I. Semchenko, S. Tretyakov, and A. Sihvola, *Electromagnetics of bi-anisotropic materials : theory and applications*. Australia: Gordon and Breach Science, 2001.

[42] S. Campione and F. Capolino, "Ewald method for 3D periodic dyadic Green's functions and complex modes in composite materials made of spherical particles under the dual dipole approximation," *Radio Sci.*, vol. 47, no. 6, p. RS0N06, Dec. 2012.

[43] A. H. Sihvola and I. V. Lindell, "Chiral Maxwell-Garnett mixing formula," *Electron. Lett.*, vol. 26, no. 2, pp. 118–119, Jan. 1990.

[44] K. L. Kelly et al., "The Optical Properties of Metal Nanoparticles: The Influence of Size, Shape, and Dielectric Environment," *J. Phys. Chem. B*, vol. 107, no. 3, pp. 668–677, Jan. 2003.

[45] P. K. Jain, K. S. Lee, I. H. El-Sayed, and M. A. El-Sayed, "Calculated Absorption and Scattering Properties of Gold Nanoparticles of Different Size, Shape, and Composition: Applications in Biological Imaging and Biomedicine," *J. Phys. Chem. B*, vol. 110, no. 14, pp. 7238–7248, Apr. 2006.

[46] K. A. Willets and R. P. V. Duyne, "Localized Surface Plasmon Resonance Spectroscopy and Sensing," *Annu. Rev. Phys. Chem.*, vol. 58, no. 1, pp. 267–297, 2007.

[47] L.-W. Nien, S.-C. Lin, B.-K. Chao, M.-J. Chen, J.-H. Li, and C.-H. Hsueh, "Giant Electric Field Enhancement and Localized Surface Plasmon Resonance by Optimizing Contour Bowtie Nanoantennas," *J. Phys. Chem. C*, vol. 117, no. 47, pp. 25004–25011, Nov. 2013.

[48] X. Wu *et al.*, "Nanoparticles: Gold Core-DNA-Silver Shell Nanoparticles with Intense Plasmonic Chiroptical Activities (Adv. Funct. Mater. 6/2015)," *Adv. Funct. Mater.*, vol. 25, no. 6, pp. 987–987, Feb. 2015.

[49] M. V. Gorkunov, A. N. Darinskii, and A. V. Kondratov, "Enhanced sensing of molecular optical activity with plasmonic nanohole arrays," *JOSA B*, vol. 34, no. 2, pp. 315–320, Feb. 2017.

[50] A. O. Govorov, Z. Fan, P. Hernandez, J. M. Slocik, and R. R. Naik, "Theory of Circular Dichroism of Nanomaterials Comprising Chiral Molecules and Nanocrystals: Plasmon Enhancement, Dipole Interactions, and Dielectric Effects," *Nano Lett.*, vol. 10, no. 4, pp. 1374–1382, Apr. 2010.

[51] A. O. Govorov, “Plasmon-Induced Circular Dichroism of a Chiral Molecule in the Vicinity of Metal Nanocrystals. Application to Various Geometries,” *J. Phys. Chem. C*, vol. 115, no. 16, pp. 7914–7923, Apr. 2011.

[52] J. M. Slocik, A. O. Govorov, and R. R. Naik, “Plasmonic Circular Dichroism of Peptide-Functionalized Gold Nanoparticles,” *Nano Lett.*, vol. 11, no. 2, pp. 701–705, Feb. 2011.

[53] F. Lu *et al.*, “Discrete Nanocubes as Plasmonic Reporters of Molecular Chirality,” *Nano Lett.*, vol. 13, no. 7, pp. 3145–3151, Jul. 2013.

[54] M. Darvishzadeh-Varcheie, C. Guclu, R. Ragan, O. Boyraz, and F. Capolino, “Electric field enhancement with plasmonic colloidal nanoantennas excited by a silicon nitride waveguide,” *Opt. Express*, vol. 24, no. 25, pp. 28337–28352, Dec. 2016.

[55] D. V. Guzatov and V. V. Klimov, “The influence of chiral spherical particles on the radiation of optically active molecules,” *New J. Phys.*, vol. 14, no. 12, p. 123009, 2012.

[56] V. V. Klimov, I. V. Zabkov, A. A. Pavlov, and D. V. Guzatov, “Eigen oscillations of a chiral sphere and their influence on radiation of chiral molecules,” *Opt. Express*, vol. 22, no. 15, pp. 18564–18578, Jul. 2014.

[57] Y. Martin, C. C. Williams, and H. K. Wickramasinghe, “Atomic force microscope–force mapping and profiling on a sub 100-Å scale,” *J. Appl. Phys.*, vol. 61, no. 10, pp. 4723–4729, May 1987.

[58] R. Mohammadi-Baghaee and J. Rashed-Mohassel, “The Chirality Parameter for Chiral Chemical Solutions,” *J. Solut. Chem.*, vol. 45, no. 8, pp. 1171–1181, Aug. 2016.

[59] A. Penzkofer, “Optical Rotatory Dispersion Measurement of D-Glucose with Fixed Polarizer Analyzer Accessory in Conventional Spectrophotometer,” *J. Anal. Sci. Instrum.*, vol. Vol. 3, pp. 234–239, Dec. 2013.

[60] J. Lambert, R. N. Compton, and T. D. Crawford, “The optical activity of carvone: A theoretical and experimental investigation,” *J. Chem. Phys.*, vol. 136, no. 11, p. 114512, Mar. 2012.

[61] P. Y. Bruice, *Organic Chemistry*, 6th ed. United States: Pearson, 2011.

[62] T. J. Katz and C. P. Nuckolls, “Aggregrates of substituted (6)helicene compounds that show enhanced optical rotatory power and nonlinear optical response and uses thereof,” US5993700 A, 30-Nov-1999.

[63] M. Caricato, P. H. Vaccaro, T. D. Crawford, Kenneth. B. Wiberg, and P. Lahiri, “Insights on the Origin of the Unusually Large Specific Rotation of (1S,4S)-Norbornenone,” *J. Phys. Chem. A*, vol. 118, no. 26, pp. 4863–4871, Jul. 2014.

[64] J. Yang, A. P. Somlyo, Z. Siao, and J. Mou, “Cryogenic atomic force microscope,” US5410910 A, 02-May-1995.

[65] P. M. Hansen, V. K. Bhatia, N. Harrit, and L. Oddershede, “Expanding the Optical Trapping Range of Gold Nanoparticles,” *Nano Lett.*, vol. 5, no. 10, pp. 1937–1942, Oct. 2005.

[66] C. Selhuber-Unkel, I. Zins, O. Schubert, C. Sönnichsen, and L. B. Oddershede, “Quantitative Optical Trapping of Single Gold Nanorods,” *Nano Lett.*, vol. 8, no. 9, pp. 2998–3003, Sep. 2008.

[67] F. Hajizadeh and S. N. S.Reihani, “Optimized optical trapping of gold nanoparticles,” *Opt. Express*, vol. 18, no. 2, pp. 551–559, Jan. 2010.

[68] C. F. Bohren, “PhD Thesis,” University of Arizona, 1975.

[69] D. Jackson, *Classical Electrodynamics*. New York: Wiley, 1998.

[70] S. Zouhdi, A. Sihvola, and M. Arsalane, *Advances in Electromagnetics of Complex Media and Metamaterials*. Netherlands: Springer, 2002.

[71] I. Sersic, C. Tuambilangana, T. Kampfrath, and A. F. Koenderink, “Magnetoelectric point scattering theory for metamaterial scatterers,” *Phys. Rev. B*, vol. 83, no. 24, p. 245102, Jun. 2011.

[72] I. Sersic, M. A. van de Haar, F. B. Arango, and A. F. Koenderink, “Ubiquity of Optical Activity in Planar Metamaterial Scatterers,” *Phys. Rev. Lett.*, vol. 108, no. 22, p. 223903, May 2012.

[73] H. Lodish, A. Berk, S. L. Zipursky, P. Matsudaira, D. Baltimore, and J. Darnell, *Molecular Cell Biology*, 4th ed. W. H. Freeman, 2000.

[74] M. A. Heim, M. Jakoby, M. Werber, C. Martin, B. Weisshaar, and P. C. Bailey, “The Basic Helix–Loop–Helix Transcription Factor Family in Plants: A Genome-Wide Study of Protein Structure and Functional Diversity,” *Mol. Biol. Evol.*, vol. 20, no. 5, pp. 735–747, May 2003.

[75] I. J. Joye, B. Lagrain, and J. A. Delcour, “Use of chemical redox agents and exogenous enzymes to modify the protein network during breadmaking – A review,” *J. Cereal Sci.*, vol. 50, no. 1, pp. 11–21, Jul. 2009.

[76] S. A. Mortimer, M. A. Kidwell, and J. A. Doudna, “Insights into RNA structure and function from genome-wide studies,” *Nat. Rev. Genet.*, vol. 15, no. 7, pp. 469–479, Jul. 2014.

[77] J. Moult, K. Fidelis, A. Kryshtafovych, T. Schwede, and A. Tramontano, “Critical assessment of methods of protein structure prediction: Progress and new directions in round XI,” *Proteins Struct. Funct. Bioinforma.*, vol. 84, pp. 4–14, Sep. 2016.

[78] Y. Huang and L. Liu, “Protein modification: Standing out from the crowd,” *Nat. Chem.*, vol. 8, no. 2, pp. 101–102, Feb. 2016.

[79] L. D. Barron, E. W. Blanch, and L. Hecht, “Unfolded proteins studied by raman optical activity,” vol. 62, B.-A. in P. Chemistry, Ed. Academic Press, 2002, pp. 51–90.

[80] P. Coullet, L. Gil, and F. Rocca, “Optical vortices,” *Opt. Commun.*, vol. 73, no. 5, pp. 403–408, Nov. 1989.

[81] M. Veysi, C. Guclu, and F. Capolino, “Vortex beams with strong longitudinally polarized magnetic field and their generation by using metasurfaces,” *JOSA B*, vol. 32, no. 2, pp. 345–354, Feb. 2015.

[82] M. Veysi, C. Guclu, and F. Capolino, “Focused azimuthally polarized vector beam and spatial magnetic resolution below the diffraction limit,” *JOSA B*, vol. 33, no. 11, pp. 2265–2277, Nov. 2016.

[83] C. Guclu, M. Veysi, and F. Capolino, “Photoinduced Magnetic Nanoprobe Excited by an Azimuthally Polarized Vector Beam,” *ACS Photonics*, vol. 3, no. 11, pp. 2049–2058, Nov. 2016.

[84] P. Woźniak, P. Banzer, and G. Leuchs, “Selective switching of individual multipole resonances in single dielectric nanoparticles,” *Laser Photonics Rev.*, vol. 9, no. 2, pp. 231–240, 2015.

[85] P. Woźniak, I. De León, K. Höflich, G. Leuchs, and P. Banzer, “Interaction of light carrying orbital angular momentum with a chiral dipolar scatterer,” *ArXiv190201731 Phys.*, Feb. 2019.

[86] K. C. Neuman and A. Nagy, “Single-molecule force spectroscopy: optical tweezers, magnetic tweezers and atomic force microscopy,” *Nat. Methods*, vol. 5, no. 6, pp. 491–505, Jun. 2008.

[87] J. A. Dionne, “Towards all-optical chiral resolution with achiral plasmonic and dielectric nanostructures (Conference Presentation),” in *Complex Light and Optical Forces XII*, 2018, vol. 10549, p. 1054913.

[88] J. Zeng *et al.*, “Sharply Focused Azimuthally Polarized Beams with Magnetic Dominance: Near-Field Characterization at Nanoscale by Photoinduced Force Microscopy,” *ACS Photonics*, vol. 5, no. 2, pp. 390–397, Feb. 2018.

[89] M. Kamandi *et al.*, “Enantiospecific Detection of Chiral Nanosamples Using Photoinduced Force,” *Phys. Rev. Appl.*, vol. 8, no. 6, p. 064010, Dec. 2017.

[90] I. V. Lindell, A. H. Sihvola, S. A. Tretyakov, and A. J. vitanen, *Electromagnetic Waves in Chiral and Bi-Isotropic Media*. Boston: Artech House, 1994.

[91] T. Mackay and A. Lakhtakia, *Electromagnetic Anisotropy and Bianisotropy - A Field Guide*. London: World Scientific Publishing, 2010.

[92] M. Kamandi, S.-M.-H. Emadi, and R. Faraji-Dana, “Integral Equation Analysis of Multilayered Waveguide Bends Using Complex Images Green’s Function Technique,” *J. Light. Technol.*, vol. 33, no. 9, pp. 1774–1779, May 2015.

[93] T. Tumkur *et al.*, “Wavelength-Dependent Optical Force Imaging of Bimetallic Al–Au Heterodimers,” *Nano Lett.*, vol. 18, no. 3, pp. 2040–2046, Mar. 2018.

[94] R. Alaee, C. Rockstuhl, and I. Fernandez-Corbaton, “An electromagnetic multipole expansion beyond the long-wavelength approximation,” *Opt. Commun.*, vol. 407, pp. 17–21, Jan. 2018.

[95] V. S. Asadchy, I. A. Faniayeu, Y. Ra’di, and S. A. Tretyakov, “Determining polarizability tensors for an arbitrary small electromagnetic scatterer,” *Photonics Nanostructures - Fundam. Appl.*, vol. 12, no. 4, pp. 298–304, Aug. 2014.

[96] J. P. Gordon, “Radiation Forces and Momenta in Dielectric Media,” *Phys. Rev. A*, vol. 8, no. 1, pp. 14–21, Jul. 1973.

[97] D. Gao *et al.*, “Optical manipulation from the microscale to the nanoscale: fundamentals, advances and prospects,” *Light Sci. Appl.*, vol. 6, no. 9, p. e17039, Sep. 2017.

[98] M. Albooyeh *et al.*, “Photo-induced force vs power in chiral scatterrers,” in *2017 IEEE International Symposium on Antennas and Propagation USNC/URSI National Radio Science Meeting*, 2017, pp. 35–36.

[99] J. Zeng *et al.*, "In pursuit of photo-induced magnetic and chiral microscopy," *EPJ Appl. Metamaterials*, vol. 5, p. 7, 2018.

[100] M. Darvishzadeh-Varcheie, C. Guclu, and F. Capolino, "Magnetic Nanoantennas Made of Plasmonic Nanoclusters for Photoinduced Magnetic Field Enhancement," *Phys. Rev. Appl.*, vol. 8, no. 2, p. 024033, Aug. 2017.

[101] A. Holleczek, A. Aiello, C. Gabriel, C. Marquardt, and G. Leuchs, "Classical and quantum properties of cylindrically polarized states of light," *Opt. Express*, vol. 19, no. 10, pp. 9714–9736, May 2011.

[102] J. S. Eismann, M. Neugebauer, and P. Banzer, "Exciting a chiral dipole moment in an achiral nanostructure," *Optica*, vol. 5, no. 8, pp. 954–959, Aug. 2018.

[103] S. Nechayev and P. Banzer, "Mimicking Chiral Light-Matter Interaction," *ArXiv190401910 Phys.*, Apr. 2019.

[104] S. Campione and F. Capolino, "Ewald method for 3D periodic dyadic Green's functions and complex modes in composite materials made of spherical particles under the dual dipole approximation," *Radio Sci.*, vol. 47, no. 6, p. RS0N06, Dec. 2012.

[105] N. Tischler *et al.*, "Experimental control of optical helicity in nanophotonics," *Light Sci. Appl.*, vol. 3, no. 6, p. e183, Jun. 2014.

[106] I. Fernandez-Corbaton, "Helicity and duality symmetry in light matter interactions: Theory and applications," *ArXiv14074432 Phys.*, Jul. 2014.

[107] C. Guclu, V. A. Tamma, H. K. Wickramasinghe, and F. Capolino, "Photo-induced Magnetic Force Between Nanostructures," *Phys. Rev. B*, vol. 92, no. 23, Dec. 2015.

[108] R. W. Woody, "Theory of Circular Dichroism of Proteins," in *Circular Dichroism and the Conformational Analysis of Biomolecules*, G. D. Fasman, Ed. Boston, MA: Springer US, 1996, pp. 25–67.

[109] A. F. Drake, "Circular Dichroism," in *Microscopy, Optical Spectroscopy, and Macroscopic Techniques*, C. Jones, B. Mulloy, and A. H. Thomas, Eds. Totowa, NJ: Humana Press, 1994, pp. 219–244.

[110] G. Snatzke, "Circular Dichroism and Optical Rotatory Dispersion — Principles and Application to the Investigation of the Stereochemistry of Natural Products," *Angew. Chem. Int. Ed. Engl.*, vol. 7, no. 1, pp. 14–25, 1968.

[111] M. Kamandi *et al.*, "Unscrambling Structured Chirality with Structured Light at the Nanoscale Using Photoinduced Force," *ACS Photonics*, vol. 5, no. 11, pp. 4360–4370, Nov. 2018.

[112] I. Rajapaksa, K. Uenal, and H. K. Wickramasinghe, "Image force microscopy of molecular resonance: A microscope principle," *Appl. Phys. Lett.*, vol. 97, no. 7, p. 073121, Aug. 2010.

[113] M. Kamandi *et al.*, "Enantiospecific Detection of Chiral Nanosamples Using Photoinduced Force," *Phys. Rev. Appl.*, vol. 8, no. 6, p. 064010, Dec. 2017.

[114] M. Hanifeh, M. Albooyeh, and F. Capolino, "Optimally Chiral Electromagnetic Fields: Helicity Density and Interaction of Structured Light with Nanoscale Matter," *ArXiv180904117 Phys.*, Sep. 2018.

[115] M. Hanifeh, M. Albooyeh, and F. Capolino, "Helicity Maximization of Structured Light to Empower Nanoscale Chiral Matter Interaction," *ArXiv180904119 Phys.*, Sep. 2018.

[116] A. E. Cohen, "Control of Nanoparticles with Arbitrary Two-Dimensional Force Fields," *Phys. Rev. Lett.*, vol. 94, no. 11, p. 118102, Mar. 2005.

[117] H. Chen, C. Liang, S. Liu, and Z. Lin, "Chirality sorting using two-wave-interference\char21{}induced lateral optical force," *Phys. Rev. A*, vol. 93, no. 5, p. 053833, May 2016.

[118] M. H. Alizadeh and B. M. Reinhard, "Transverse Chiral Optical Forces by Chiral Surface Plasmon Polaritons," *ACS Photonics*, vol. 2, no. 12, pp. 1780–1788, Dec. 2015.

[119] T. Zhang *et al.*, "All-Optical Chirality-Sensitive Sorting via Reversible Lateral Forces in Interference Fields," *ACS Nano*, vol. 11, no. 4, pp. 4292–4300, Apr. 2017.

[120] F. Patti *et al.*, "Chiral optical tweezers for optically active particles in the T-matrix formalism," *Sci. Rep.*, vol. 9, no. 1, p. 29, Jan. 2019.

[121] F. J. Rodríguez-Fortuño, N. Engheta, A. Martínez, and A. V. Zayats, "Lateral forces on circularly polarizable particles near a surface," *Nat. Commun.*, vol. 6, p. 8799, Nov. 2015.

[122] M. Hanifeh, M. Albooyeh, and F. Capolino, "Helicity Maximization of Structured Light to Empower Nanoscale Chiral Matter Interaction," *ArXiv180904119 Phys.*, Sep. 2018.

[123] M. Hanifeh, M. Albooyeh, and F. Capolino, "Optimally Chiral Electromagnetic Fields: Helicity Density and Interaction of Structured Light with Nanoscale Matter," *ArXiv180904117 Phys.*, Sep. 2018.

[124] M. Veysi, C. Guclu, and F. Capolino, "Focused azimuthally polarized vector beam and spatial magnetic resolution below the diffraction limit," *JOSA B*, vol. 33, no. 11, pp. 2265–2277, Nov. 2016.

[125] J. Zeng *et al.*, "Exclusive Magnetic Excitation Enabled by Structured Light Illumination in a Nanoscale Mie Resonator," *ACS Nano*, vol. 12, no. 12, pp. 12159–12168, Dec. 2018.

[126] P. B. Johnson and R. W. Christy, "Optical Constants of the Noble Metals," *Phys. Rev. B*, vol. 6, no. 12, pp. 4370–4379, Dec. 1972.

[127] A. Novitsky, C.-W. Qiu, and H. Wang, "Single Gradientless Light Beam Drags Particles as Tractor Beams," *Phys. Rev. Lett.*, vol. 107, no. 20, p. 203601, Nov. 2011.

[128] J. J. Sáenz, "Optical forces: Laser tractor beams," *Nat. Photonics*, vol. 5, no. 9, pp. 514–515, Sep. 2011.

[129] V. Shvedov, A. R. Davoyan, C. Hnatovsky, N. Engheta, and W. Krolikowski, "A long-range polarization-controlled optical tractor beam," *Nat. Photonics*, vol. 8, no. 11, pp. 846–850, Nov. 2014.

[130] F. J. Rodríguez-Fortuño, A. Vakil, and N. Engheta, "Electric Levitation Using ϵ-Near-Zero Metamaterials," *Phys. Rev. Lett.*, vol. 112, no. 3, p. 033902, Jan. 2014.

[131] G. Subramania, A. J. Fischer, and T. S. Luk, "Optical properties of metal-dielectric based epsilon near zero metamaterials," *Appl. Phys. Lett.*, vol. 101, no. 24, p. 241107, Dec. 2012.

[132] S. Campione, M. Albani, and F. Capolino, "Complex modes and near-zero permittivity in 3D arrays of plasmonic nanoshells: loss compensation using gain [Invited]," *Opt. Mater. Express*, vol. 1, no. 6, p. 1077, Oct. 2011.

[133] A. Alù and N. Engheta, "Boosting Molecular Fluorescence with a Plasmonic Nanolauncher," *Phys. Rev. Lett.*, vol. 103, no. 4, p. 043902, Jul. 2009.

[134] G. D'Aguanno, N. Mattiucci, M. J. Bloemer, R. Trimm, N. Aközbek, and A. Alù, "Frozen light in a near-zero index metasurface," *Phys. Rev. B*, vol. 90, no. 5, p. 054202, Aug. 2014.

[135] I. Liberal, A. M. Mahmoud, and N. Engheta, "Geometry-invariant resonant cavities," *Nat. Commun.*, vol. 7, p. 10989, Mar. 2016.

[136] G. Lovat, P. Burghignoli, F. Capolino, D. R. Jackson, and D. R. Wilton, "Analysis of directive radiation from a line source in a metamaterial slab with low permittivity," *IEEE Trans. Antennas Propag.*, vol. 54, no. 3, pp. 1017–1030, Mar. 2006.

[137] G. Lovat, P. Burghignoli, F. Capolino, and D. R. Jackson, “High directivity in low-permittivity metamaterial slabs: Ray-optic vs. leaky-wave models,” *Microw. Opt. Technol. Lett.*, vol. 48, no. 12, pp. 2542–2548, Dec. 2006.

[138] G. Lovat, P. Burghignoli, F. Capolino, and D. R. Jackson, “Combinations of low/high permittivity and/or permeability substrates for highly directive planar metamaterial antennas,” *Antennas Propag. IET Microw.*, vol. 1, no. 1, pp. 177–183, Feb. 2007.

[139] A. Alù, M. G. Silveirinha, A. Salandrino, and N. Engheta, “Epsilon-near-zero metamaterials and electromagnetic sources: Tailoring the radiation phase pattern,” *Phys. Rev. B*, vol. 75, no. 15, p. 155410, Apr. 2007.

[140] F. Monticone and A. Alù, “Embedded Photonic Eigenvalues in 3D Nanostructures,” *Phys. Rev. Lett.*, vol. 112, no. 21, p. 213903, May 2014.

[141] B. Edwards, A. Alù, M. E. Young, M. Silveirinha, and N. Engheta, “Experimental Verification of Epsilon-Near-Zero Metamaterial Coupling and Energy Squeezing Using a Microwave Waveguide,” *Phys. Rev. Lett.*, vol. 100, no. 3, p. 033903, Jan. 2008.

[142] S. Campione, D. de Ceglia, M. A. Vincenti, M. Scalora, and F. Capolino, “Electric field enhancement in $\ensuremath{\varepsilon}$-near-zero slabs under TM-polarized oblique incidence,” *Phys. Rev. B*, vol. 87, no. 3, p. 035120, Jan. 2013.

[143] M. A. Vincenti, S. Campione, D. de Ceglia, F. Capolino, and M. Scalora, “Gain-assisted harmonic generation in near-zero permittivity metamaterials made of plasmonic nanoshells,” *New J. Phys.*, vol. 14, no. 10, p. 103016, 2012.

[144] D. de Ceglia, S. Campione, M. A. Vincenti, F. Capolino, and M. Scalora, “Low-damping epsilon-near-zero slabs: Nonlinear and nonlocal optical properties,” *Phys. Rev. B*, vol. 87, no. 15, p. 155140, Apr. 2013.

[145] C. Argyropoulos, G. D’Aguanno, and A. Alù, “Giant second-harmonic generation efficiency and ideal phase matching with a double \ensuremath{\epsilon}-near-zero cross-slit metamaterial,” *Phys. Rev. B*, vol. 89, no. 23, p. 235401, Jun. 2014.

[146] T. S. Luk *et al.*, “Enhanced third harmonic generation from the epsilon-near-zero modes of ultrathin films,” *Appl. Phys. Lett.*, vol. 106, no. 15, p. 151103, Apr. 2015.

[147] A. Capretti, Y. Wang, N. Engheta, and L. D. Negro, “Enhanced third-harmonic generation in Si-compatible epsilon-near-zero indium tin oxide nanolayers,” *Opt. Lett.*, vol. 40, no. 7, pp. 1500–1503, Apr. 2015.

[148] A. Capretti, Y. Wang, N. Engheta, and L. Dal Negro, “Comparative Study of Second-Harmonic Generation from Epsilon-Near-Zero Indium Tin Oxide and Titanium Nitride Nanolayers Excited in the Near-Infrared Spectral Range,” *ACS Photonics*, vol. 2, no. 11, pp. 1584–1591, Nov. 2015.

[149] C. Argyropoulos, P.-Y. Chen, G. D’Aguanno, N. Engheta, and A. Alù, “Boosting optical nonlinearities in $\ensuremath{\epsilon}$-near-zero plasmonic channels,” *Phys. Rev. B*, vol. 85, no. 4, p. 045129, Jan. 2012.

[150] L. D. Landau, L. P. Pitaevskii, and E. M. Lifshitz, *Electrodynamics of Continuous Media - 2nd Edition*. Oxford, UK: Butterworth-Heinemann, 1984.

[151] C. Guclu, S. Campione, and F. Capolino, “Hyperbolic metamaterial as super absorber for scattered fields generated at its surface,” *Phys. Rev. B*, vol. 86, no. 20, p. 205130, Nov. 2012.

[152] E. Sachet *et al.*, “Dysprosium-doped cadmium oxide as a gateway material for mid-infrared plasmonics,” *Nat. Mater.*, vol. 14, no. 4, pp. 414–420, Apr. 2015.

[153] H. H. Li, “Refractive index of silicon and germanium and its wavelength and temperature derivatives,” *J. Phys. Chem. Ref. Data*, vol. 9, no. 3, pp. 561–658, Jul. 1980.

[154] C. Guclu, T. S. Luk, G. T. Wang, and F. Capolino, “Radiative Emission Enhancement Using Nano-antennas Made of Hyperbolic Metamaterial Resonators,” *Appl. Phys. Lett.*, vol. 105, no. 12, p. 123101, Sep. 2014.

[155] M. Sivis, M. Duwe, B. Abel, and C. Ropers, “Extreme-ultraviolet light generation in plasmonic nanostructures,” *Nat. Phys.*, vol. 9, no. 5, pp. 304–309, May 2013.